SED COMP DESIGN TDB

C00-2823-2

FINAL REPORT FOR A 10 KWT SOLAR ENERGY RECEIVER

DECEMBER 1978

CONTRACT NO. EY-76-C-03-1533

(Formerly Contract No. EY-76-C-02-2823)

Prepared by:

SANDERS ASSOCIATES, INC.

ENERGY SYSTEMS CENTER

95 Canal Street
Nashua, New Hampshire 03061

C000-2823-2

FINAL REPORT
FOR A
10 KWt SOLAR ENERGY RECEIVER

December 1978

Prepared for

Department of Energy
Chicago Operations Office
9800 South Cass Avenue
Argonne, IL 60439

Contract No. EY-76-C-03-1533
(Formerly Contract No. EY-76-C-02-2823)

Prepared by

SANDERS ASSOCIATES, INC.
ENERGY SYSTEMS CENTER

95 Canal Street
Nashua, N.H. 03061

ABSTRACT

The primary objective of this contract was to design and build a 10 kilowatt thermal (kWt) solar-to-air receiver, and to test its performance at the White Sands Solar Test Facility. Following the successful test program, a systems analysis of a 100 megawatt electric (MWe) power tower conceptual design based on an open cycle air Brayton system was performed.

Experimental results indicated that thermal conversion efficiencies (heat added to the air divided by the solar energy in) varied from 0.75 to 0.85. These results were obtained in spite of a highly inhomogeneous solar flux distribution at the ceramic matrix. Flux variations as high as 10:1 were measured. Test goals and achievements were:

PARAMETER	GOAL	ACHIEVED
INPUT POWER (kW)	14.3	24.6
ΔT (^{o}C)	305	455
T_{IN} (^{o}C)	620	510
T_{OUT} (^{o}C)	925	965
ΔP (INCH H_2O)	2	0.1-0.3
Efficiency (η)	0.70	0.85

The 100 MWe power plant conceptual design uses an offset mirror field having 9700 heliostats which focus the solar energy onto a 15.1 meter diameter receiver aperture. The receiver is located on a 233 meter high tower, along with the thermal storage vessels and the power generation equipment.

The open cycle Brayton concept was selected as the power plant because it has high conversion efficiency, relatively low cost, and does not require cooling water. The key feature of Sanders' concept

is the ability to separate the solar collection cycle from the power generation cycle by using highly efficient sensible heat storage. Operationally, this allows the scheduling of power output to meet demand without direct dependence on instantaneous insolation. Sensible heat storage units, in the form of modified checker stoves developed under an independent research and development program, designed to operate in the thermocline mode, are closely coupled to the receiver and gas turbine components for minimum loss.

TABLE OF CONTENTS

SECTION 1
INTRODUCTION

SECTION 2
ANALYSIS

SECTION 3
EXPERIMENT

TABLE OF CONTENTS (Continued)

SECTION 4
CONCEPTUAL DESIGN FOR A 100 MWe SOLAR POWER PLANT

TABLE OF CONTENTS (Continued)

LIST OF ILLUSTRATIONS

LIST OF ILLUSTRATIONS (Continued)

LIST OF TABLES

SECTION 1
INTRODUCTION

As part of the increasing concern regarding the nation's future energy need, increased consideration has been given to large-scale, solar-powered electric generating plants. Design studies have been completed for 100 MWe "power tower" steam turbine plants, and construction of the 10 MWe solar electric demonstration plant is underway. In addition, recent advances in high temperature gas turbine technology allow substantial advantages to be derived by implementing gas turbine (open air Brayton cycle) prime movers instead of the steam turbine (Rankine cycle).

The Brayton cycle is ~~favored~~ considered a good candidate because it:

- Reduces initial cost - derived through a reduction in mirror field costs resulting from potentially higher thermal cycle efficiency

- Reduces dependence on water availability and/or elimination of dry cooling towers required for steam plants

- Reduces startup times - of particular value in "peaking" applications

The Department of Energy (then ERDA) initial solar energy contract with Sanders was to develop and demonstrate a ~~10 KWt~~ small scale (10 KWt) receiver for use in an open cycle Brayton system. Part of this effort was designed to obtain basic data on the properties of receiver configurations as used in an air cycle system. The program emphasized obtaining heat transfer data and provided the baseline experimental data required to ultimately build and operate full-scale solar receivers for the electric utility industry. Most of this work was performed during the period of November, 1975 through March, 1977.

The 10 kWt receiver was selected as a basic experiment which could be tested at the largest existing solar facility in the U.S.; the solar furnace at the White Sands Nuclear Effects Facility. Extrapolation of the test results allows for the design and construction of a scaled experiment to considerably higher power levels.

Concurrent with this DOE-funded solar receiver program, Sanders has been involved in an internal research and development program to overcome two problems associated with the high operating temperatures required for maximum efficiency of the Brayton cycle installation. These problems involve the central tower solar receiver/heat exchanger, and the thermal storage system. Problems with the receiver derive from the requirement that the air, at the point in the cycle where heat is added (Figure 1-1), be compressed to several atmospheres (the actual value depending on specific cycle parameters). The receiver must therefore be of ceramic tube construction which is capable of withstanding high temperature and pressure; or, in Sanders' approach, must have a pressure sealing window. At the power levels of interest in commercial power systems, the severe thermal and structural problems make such a large window impractical. In the case of the ceramic tube receiver, there are severe thermal stress problems due to nonuniform radiant inputs. In addition, these tube receivers present a large pressure drop which adversely affects the overall turbine efficiency.

The second problem area is related to the thermal storage requirement. Thermal storage is required to: (a) act as a buffer against short-term variations in solar insolation, and (b) provide for plant operation during the early evening hours when demand exceeds the solar input. Previous efforts to provide efficient, inexpensive storage at high temperatures (~930^{o}C) have focused on latent heat systems (e.g., metallic salts), because of the high energy released per unit mass of these compounds. These storage systems have severe

economic and operational disadvantages (e.g., corrosion) and require a high temperature heat exchanger to transfer the heat to the turbine loop.

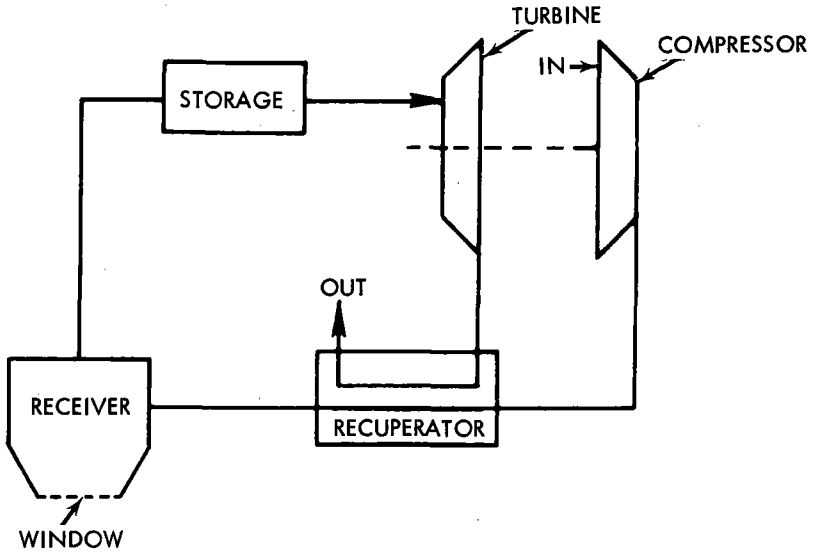

Figure 1-1. Conventional Solar Brayton System

Sanders' Internal Research and Development (IR&D) program initiated the investigation of energy storage systems and the tradeoffs in a Brayton cycle system with storage. This research and development effort, coupled with the work under this contract, has been directed toward development of a practical solution to the problems described above. Results of the work to data indicate that a storage system can be coupled with the recuperated Brayton cycle engine by replacing the recuperators with thermocline stoves, which are improved versions of "checker stove" units in the steel and glass industries during the past 50 years.

These thermocline stoves have demonstrated high reliability and low maintenance. They are currently constructed in sizes compatible with the requirements of a 50 to 100 MWe solar power plant. When used in

this configuration, improved checker stoves can eliminate the need for costly and relatively short-lived metal recuperators. (Currently, most gas turbines are not recuperated because of short recuperator life.)

This storage concept allows the use of a new receiver concept which can result in a viable commercial solar electric power system. In this concept, the solar receiver can operate at atmospheric pressure and, with suitable design, can be run efficiently with no windows. This will considerably reduce engineering complexity in commercial-size systems where the entrance aperture is 15 meters.

Figure 1-2 is a schematic representation of a solar Brayton cycle power system which uses Sanders' design approach. The receiver loop is completely independent of the engine loop and can be operated at atmospheric pressure. The storage unit connected between the compressor and the turbine operates at the optimum pressure for the engine (approximately 60 psi) and supplies all the turbine energy requirements. The storage unit in the exhaust operates as a recuperator. When such recuperators provide a sufficiently low back-pressure to the turbine, high cycle efficiencies are obtained.

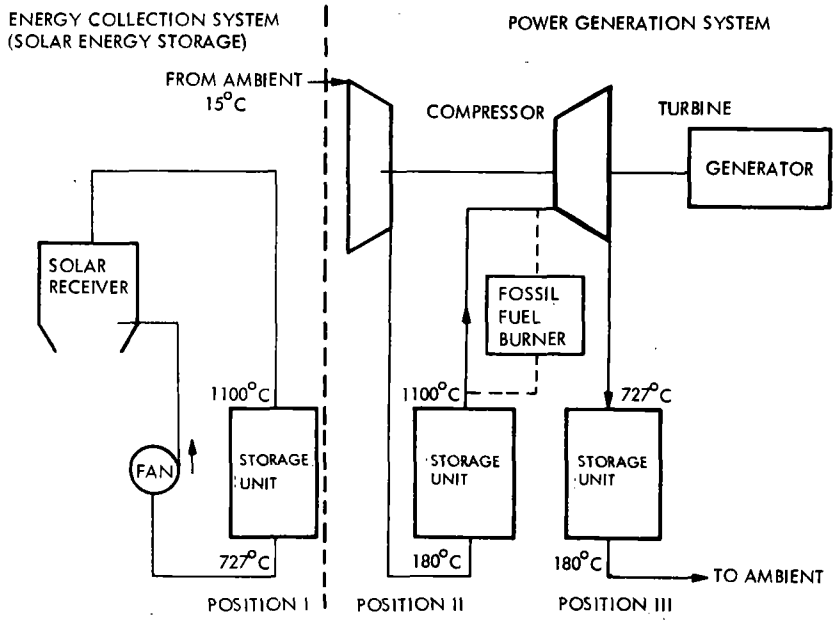

Figure 1-2. Power Plant Cycle

This concept was used as the basis of a conceptual design of a 100 MWe solar power plant. The plant is closely coupled to minimize thermal losses and is able to reject waste heat directly to the ambient environment, eliminating the need for dry cooling towers or large quantities of cooling water. This property is expected to enhance the economic viability of the system in arid and semi-arid areas such as the southwestern United States.

Section 2 of this report summarizes the analysis which was performed to attain the final solar receiver design. Section 3 describes the experiments conducted on the solar receiver at the U.S. Army White Sands Solar Test Facility. Section 4 describes the conceptual design for a 100 MWe solar power plant. Section 5 presents the conclusions to the report.

SECTION 2
ANALYSIS

The analysis required to support a solar receiver design can be separated into structural and energy capture aspects. In the study to date, the thermal analysis has been emphasized because temperature distributions in the honeycomb are basic to many of the structural problems. For the 10 KWt receiver, the energy capture analysis was subdivided into two phases: (a) solar radiation-to-surface heat conversion, and (b) surface heat-to-airstream heat conversion.

2.1 RADIATION TO HEAT CONVERSION ON THE SURFACE OF A SOLID

2.1.1 Introduction

The solar energy system design considers the effects of optical and infrared radiation impinging on the system. The potential for heat energy and the heating effect in a system depends both on the intrinsic properties of the materials irradiated and on the reflection and scattering properties of the system. One goal of solar receiver design is to minimize this reflection. The distribution of energy within the receiver structure, its transfer to an airstream, and the radiation emitted by the receiver are all simulated in the analysis.

Given a bundle of rays incident on a receiver surface, the radiation absorbed by any small area of surface (dA) is proportional to the probability of a ray striking dA(v,w); where (v,w) constitutes a coordinate system specifying a location on the surface. Any incident ray may be described by a maximum of four independent coordinates. These coordinates may include v and w, specifying the point of incidence on a plane related by projection to the surface; and θ and ϕ, specifying the azimuth and elevation of a given ray; i.e., the angle of incidence. Given the probability distributions for each of these variables: p(v),

$p(w)$, $p(\theta)$, $p(\phi)$, as well as their interdependencies as expressed through any joint probabilities [e.g., $p(\phi,\theta)$, $p(\phi,v)$, $p(\phi,\theta,w)$], it is possible to calculate $p(v,w,\theta,\phi)$ and average over θ, ϕ to obtain

$$p(v,w) = \int_{\phi}\int_{\theta} p(v,w,\theta,\phi)\, d\theta d\phi$$

It is recognized that if the surface emissivity is ε, the energy absorbed in area element $dA(v,w)$ is given by

$$I(v,w)dA = \varepsilon \mathring{Q} p(v,w) dv\, dw$$

where:

$\mathring{Q}$ = Total energy per unit time per unit area incident on the receiver surface

$I(v,w)$ = Energy per unit time per unit area absorbed by the receiver surface at the point specified by (v,w)

$p(v,w)$ = Probability of a ray striking the area enclosed by the ranges v to $v+dv$ and w to $w+dw$

$dA(v,w)$ = Element of area on the surface as specified by the above range of u and v

These calculations are potentially difficult to perform because there is no assurance of a closed form explicit solution for several of the steps involved. However, for some relatively simple cases where there is some symmetry, the surface may be described in typical analytical geometry terms (e.g., conic sections), and one or more of

the foregoing variables vanishes from the analysis. In such cases, the distributions of variables may be reasonably and explicitly expressed, and a simplified form of Monte Carlo analysis may be applied. Where the overall simulation results are not excessively sensitive to the details of the radiation distribution, the Monte Carlo analysis can be performed for a relatively small number of points (e.g., 1000). This makes the statistical analysis quite tractable, though of limited precision.

Typical of Monte Carlo methods, the formulation is simplified in that the relation between the variables (y,z,θ,ϕ) is determined explicitly, either in closed form for v and w (or directly related variables y, z), or in terms of a computer program. However, the probability distribution of the dependent variable is determined empirically from a histogram of values calculated from random selections for values of the independent variables. For example, if

$$v = f_1(y,z,\theta,\phi)$$

$$w = f_2(y,z,\theta,\phi)$$

and a pseudo-random number generator of appropriate characteristics produces each independent variable (y,z,θ,ϕ) with its appropriate probability distribution [(y), p(z), etc.], then the dependent variables (v,w) will have a distribution of values. With a sufficient number of values of (v,w), either a distribution can be inferred or a fit can be made to prescribed functional form to an accuracy commensurate with the number of values (v,w) calculated and with the required tolerance. If a probability distribution can be renormalized to a form [f(x)], for example using p(x)

$$\frac{p(x)}{\max\ [p(x)]} = f(x),$$

and an algorithm for producing pseudo-random numbers (U_1) produces a uniform distribution from 0.000 to 1.000 with the same properties but with independent uncorrelated values, then $x = f^{-1}\ (U_1)$

will be a randomly distributed variable that follows the desired probability distribution [p(x)] and may be regarded as a simulation of x. Similarly, other physical variables can be simulated with independent choices of U, such as U_2. Thus, if y has a probability distribution p(y) with a functional form

$$\frac{p(y)}{\max\ [p(y)]} = g(y)$$

then $y = g^{-1}\ (U_2)$ is a simulation for y. In turn, a combination of x and y, such as $r = x^2 + y^2$ can be simulated as

$$r = f^{-1}\ (U_1)^2 + g^{-1}\ (U_2)^2$$

An important elaboration of the above rule results when f(x) is not monotonic. In this case, $f^{-1}\ (U)$ would have multiple values and would be ambiguous. For a finite multiplicity, however, the ambiguity is readily resolved, and the results are useful. Multiple branches of $f^{-1}\ (U)$ may be defined such that each segment is monotonic. Thus, for an $f(x) \propto \exp\ (-x^2/2\sigma^2)$ Gaussian distribution, one possible simulation is given by

$$x = \sigma - 2\ \ln|2U_1-1|\ \text{sgn}\ (2U_1-1)$$

where, if $\xi = 2U_1-1$, then sgn (ξ) =

$$+1 \text{ if } \xi > 0$$

$$-1 \text{ if } \xi < 0$$

Another simulation could be

$$x = \sigma - 2\ \ln U_1\ \text{sng}\ (2U_2-1)$$

Several alternatives may be readily found, based on various methods of randomly choosing the branch of x values corresponding to the argument of f^{-1}, in addition to the argument itself.

A major point of this Monte Carlo procedure is that the deterministic part of the calculations is straight analytic geometry. The probabilistic part uses random number generators that are easily constructed, given the unit random number generator which generates a uniform distribution between 0 and 1 and which is provided on most computers.

2.1.2 Distribution of Radiation along the Axis of a Cylindrical Tube

Figure 2-1 illustrates the geometry of a typical ray from an optical system symmetric about the z-axis. With the given symmetry, the azimuth angle (ϕ) may be neglected. Since it is desired to find the intensity [I(z)] along the z-axis, the symmetry about the z-axis is fully utilized by replacing x and y with ξ and η such that the η-axis is always in a plane parallel to the z-axis and containing any incident ray, while the ξ-axis is normal to both η and z. If f is the fraction of rays entering the tubes, 1-f is the fraction striking the face. If $\dot{Q}$ is the total incident energy flux rate, then I(z) (the distribution of energy incident over the surfaces involved) is expressed by

$$\dot{Q} = (1-f)\ \dot{Q} + f\ [I(z)dz]$$

The consequent energy absorbed on the front face is $(1-f)\ \dot{Q}\varepsilon$, while the energy absorbed by the tube walls, with no bounces, is $\varepsilon f I(z)dz$ for an incremental length dz along the axis. If the basic Monte Carlo method is extended to calculate the distance (z') along the tube axis where a ray strikes the walls after one bounce, the distance (z") along the tube after two bounces, etc., then the calculation

proceeds in a similar way, with additional parameters to account for the scattering details at each bounce (essentially a polar plot of scattering off a surface by an arbitrary incident ray).

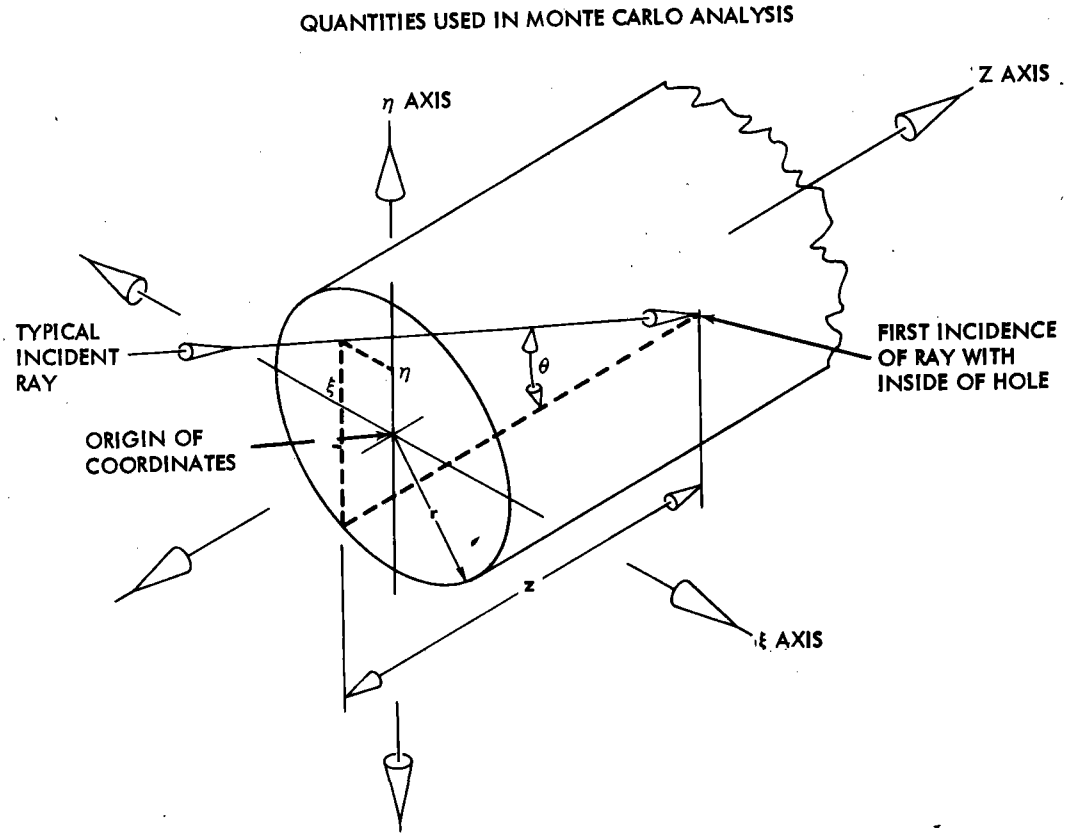

Figure 2-1. Solar Input Radiation Distribution

With the calculation of p(z), p(z'), p(z"), etc., it is possible to calculate the net energy flux absorbed in terms of a weighted sum of these probabilities (each of which can be found with a Monte Carlo calculation). Specifically,

$$I(z)_{overall} = \frac{\dot{Q}}{A}\left[I_{FACE} + f\varepsilon p(z) + f(1-\varepsilon)\varepsilon p(z') + f(1-\varepsilon)^2\,\varepsilon p(z") + f(1-\varepsilon)^3\,\varepsilon p(z''')+\ldots\right]$$

The sum of this series of distributions is frequently dealt with in a more simple form in terms of the effective emissivity of a cavity of given shape. This effective emissivity is generally closer to 1 than the surface emissivity, and depends on the cavity shape, (particularly on the cavity surface area versus the aperture area). An effective emissivity value applied to the first term [p(z) of the above series] is the counterpart of the surface emissivity applied to each individual term. The former is simpler to calculate; the latter is appropriate where more detail is needed.

The specifics of the Monte Carlo calculation for p(z) follow. From Figure 2-1 by inspection ,

$$\frac{z}{r} = \frac{\eta + \sqrt{1-\xi^2}}{\tan\,\theta}$$

where

r = radius of cylinder

η = distance from the tube axis to the ray intersection with the plane of the tube face (z=0). The η-axis is chosen to be parallel to the projection of the ray on the tube face plane as allowed by full cylindrical symmetry.

ξ = distance to the intersection of the ray with the z=0 plane in the direction normal to the tube axis.

The independent variables are θ, ξ, η, which can be simulated by random number generators as shown in the following paragraphs.

For a probability distribution for θ, based on equal contributions from each area element in the mirror field, $p(\theta) = (2N_F \tan\theta)^2$. This distribution can be simulated, using the inverse of $p(\theta)$, as

$$\theta = \tan^{-1}\left[\frac{\sqrt{U_1}}{2N_F}\right] = \tan^{-1}\left[\sqrt{U_1}\left(\tan\theta_{max}\right)\right]$$

where

U_1 is a random number uniformly distributed between 0 and 1

N_F is the effective f/number of the incident rays

Two alternate approaches can be used to simulate ξ and η:

a. $\xi = \sqrt{U_2}\left[\cos\left(2\pi U_3\right)\right]$

$\eta = \sqrt{U_2}\left[\sin\left(2\pi U_3\right)\right]$

b. $\xi = 2U_2 - 1$

$$\eta = (2U_3 - 1)\sqrt{1-\xi^2}$$

$$= (2U_3 - 1)\sqrt{1-(2U_2-1)^2}$$

where, in either case, U_2 and U_3 are independent selections from the same pseudo-random number generator as U_1. Figure 2-2 is a diagram illustrating these calculations in flow chart form.

If several values of z are calculated by this formula, the resulting tabulation of z values could be converted to a probability distribution by the following method:

a. Sort all z values in numerical order.

b. Tabulate the sequence number divided by the total number of values (which amounts to the percentile rank of the associated z value).

c. Plotting b. versus a. yields a plot of $p(z) = \int_0^z p(z)\, dz$ as a function of z.

d. If a convenient function can be fitted to p(z), analytically or graphically, its derivative is p(z).

e. In the above example, p(z) fits the error function very well; thus p(z) has a Gaussian form.

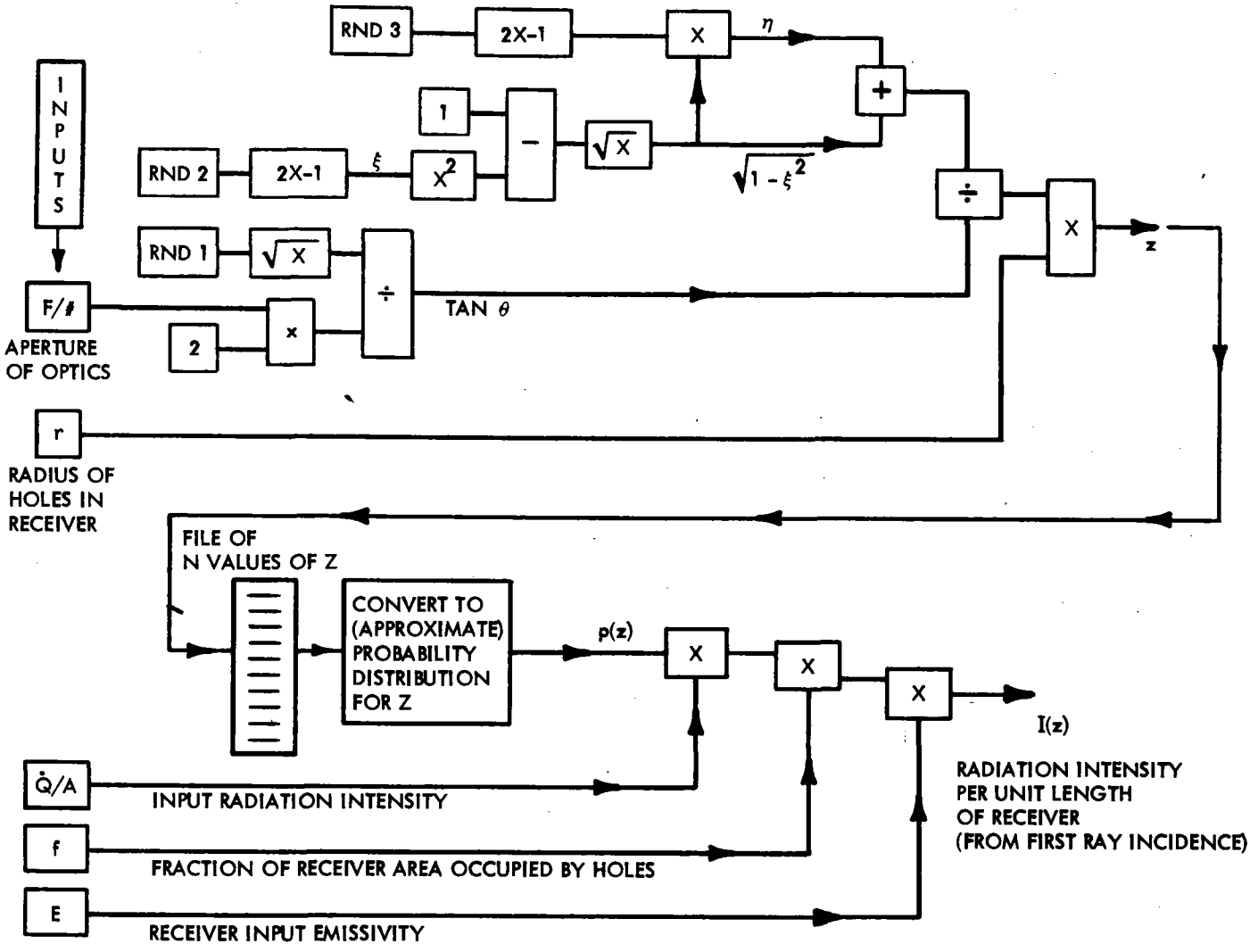

Figure 2-2. Solar Input Radiation Distribution Flow Chart

In Table 2-1, columns 3 and 4 are trial curve fits. The values $\sigma = 5$ and $\sigma = 4.2$ are found to bracket the Monte Carlo percentiles of column 2 fairly well. Giving the heaviest weight to the region near 50% (or 0.5 in column 2), where the greatest sensitivity occurs, leads to a value $\sigma \sim 5 \pm \delta$. From the variation of σ required to bracket the calculated percentiles, $\delta \sim 0.4$ and $\sigma \sim 4.8$ would be a better fit.

TABLE 2-1

DISTRIBUTION OF $\frac{Z}{r}$ VALUES FOR RAYS INCIDENT ON THE INSIDE OF A CYLINDER

	Percentile ÷ 100	Trial Curve Fits: $P(\frac{Z}{r}) = \text{erf}\left[\frac{1}{\sigma}\frac{z}{r}\right]$	
	$P(\frac{Z}{r})$	$\sigma = 5$	$\sigma = 4.2$
0.20	0.052	0.045	0.054
0.43	0.118	0.10	0.12
0.93	0.247	0.21	0.25
2.33	0.529	0.49	0.57
5.02	0.860	0.84	0.91
9.28	0.96	0.99	1.00

Calculation of more than the 1000 points used here would yield a more precise curve fit, a smaller δ, and a better check on whether $p(z) \sim \text{erf}\left[\frac{1}{\sigma}\frac{z}{r}\right]$, or whether another curve form would yield a closer fit over a greater range. In this case, however, the bracketing at high and low z values with two values of σ is a strong indication that $p(z/r) \sim \text{erf}\left[\frac{1}{\sigma}\frac{z}{r}\right]$ in form, and that

$$p(z) = \frac{d}{dz} P(z) = \frac{1}{\sigma\sqrt{2\pi}} \exp -\left[\frac{1}{2\sigma^2} \frac{z^2}{r^2}\right]$$

Thus, a distribution of heat flows has been found that corresponds to radiation absorbed in a cylinder at first ray incidence. In energy absorption terms:

$$I(z) = 2\pi r \frac{\dot{Q} f \epsilon}{A} \frac{1}{5r\sqrt{2\pi}} \exp\left[- \frac{z^2}{50^2 r^2} \right]$$

This represents the radiation distribution to sufficient accuracy for present computations (to represent an F/1, or N_F=1, bundle of rays) (see Figure 2-3).

Further bounces will effectively increase σ, and possibly change the form of the distribution. No such calculations have been performed to date, but the formulation is as follows.

Using all the variables in the formulation of p(z) above, the following variables are added to describe p(z'). θ is the angle of an incident ray with respect to the tube axis, ϕ is the angle of an emerging ray with respect to the tube axis (measured from the opposite direction), $\phi_{\parallel}$ is the component of angle in the plane defined by the ray and the tube axis, and $\phi_{\perp}$ is the component of angle in the plane perpendicular to the plane defined by the ray and tube axis. The following simulations apply:

$$\phi_{\parallel} = \theta + \sin^{-1}\left[\sigma' \, \mathrm{sgn}\,(2U_4 - 1) \sqrt{(-2 \ln|2U_4 - 1|)} \right]$$

$$\phi_{\perp} = \sin^{-1}\left[\sigma' \, \mathrm{sgn}\,(2U_5 - 1) \sqrt{(-2 \ln|2U_5 - 1|)} \right]$$

Here σ' is a parameter describing the distribution of scattered rays about the specular reflection direction.

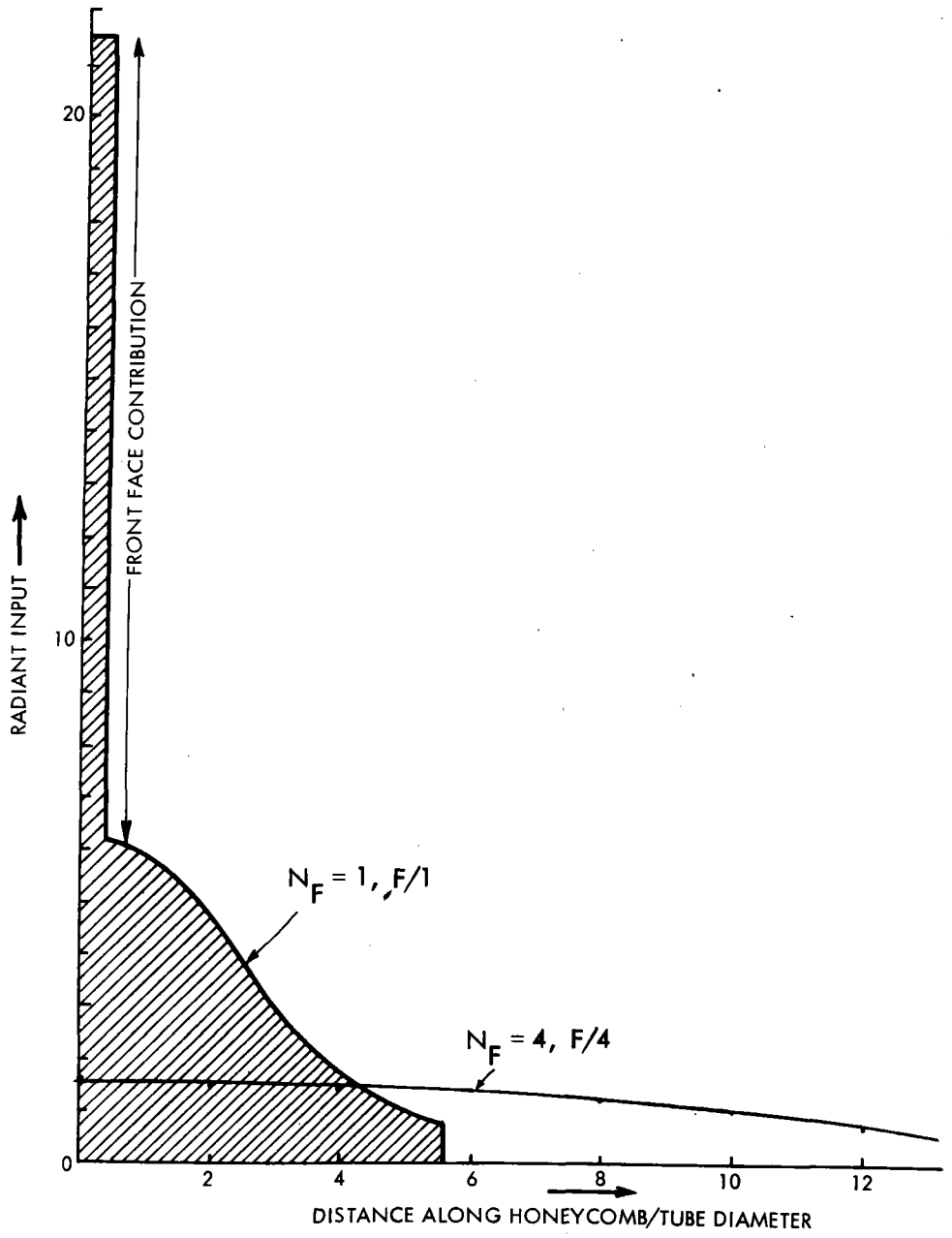

Figure 2-3. Radiant Energy Distribution

2.1.3 Examples of Scattering Special Cases

For a true Lambertian case (experimental data on SiC match this fairly well),

$$\theta = Q, \quad \sigma' = \pi/2$$

i.e., scattered rays are centered along the surface normal, and the σ' of the angular distribution is $\pi/2$ radians.

For strong backscatter

$$\theta \longleftarrow \pi - \theta$$

$$\sigma' < \pi/2$$

i.e., rays are scattered centering on their direction of origin, with an angular dispersion, σ', less than $\pi/2$ radians

$$\sigma' \longrightarrow 0$$

i.e., the reflected rays have no angular dispersion.

It is necessary to calculate the next point of incidence (at least z'), given z and $\phi_{||}$, $\phi_{\perp}$. If $\ell_{||}$ is the distance the ray travels as projected on the ξ, η plane, and $\ell_{\perp}$, the distance along z, then

$$\ell_{\perp} = 2\, r \sin \left[\phi_1 + \sin^{-1} \sqrt{1 - (z/r)^2} \right]$$

$$\ell_{||} = \ell_{\perp} / \tan \phi_{||} \left[\phi_1 + \sin^{-1} \sqrt{1 - (z/r)^2} \right]$$

$$x' = x + \ell_\perp \sin\phi_\perp$$
$$y' = y + \ell_\perp \cos\phi_\perp$$
$$z' = z + \ell_\perp$$

x', y' are in direction of new ξ', η' axes, rotated from ξ, η so as to keep the ray projection normal to x along the η axis.

With these formulas, z' can be calculated in terms of z, all the parameters specified, and the indicated random number generators. Similarly, stages of the same form can be added to account for additional bounces. While the parameters would be numerically the same, each set of random number generators would have to be independent of all previous ones in the overall ray simulation. With such calculations for z, z' and z", etc., of a typical ray, p(z), p(z'), p(z"), etc., could all be determined from histograms in the same way as the first ray incidence illustration. The weighted sum of these distributions would lead to the distribution of energy absorption along the axis as follows:

$$I(z)_{overall} = \frac{\dot{Q}}{A}\left[I_{FACE} + f\,\varepsilon\,p(z) + f\,(1-\varepsilon)\,\varepsilon\,p(z') + f\,(1-\varepsilon)^2\,\varepsilon\,p(z") + f\,(1-\varepsilon)^3\,\varepsilon\,p(z") + \ldots\right]$$

Clearly, for large ε, the terms representing additional bounces are less important in shaping the overall absorption distribution than they are for lower ε. For the $\varepsilon = 0.9$ value assumed (exceeded by the materials treated to date), the higher terms have been neglected; but a value of $\sigma = 5r$, on the high side of the Monte Carlo curve fitting tolerance, has been used. If materials with lower ϵ values are seriously considered, the above calculations should be reviewed and carried out to the degree warranted. For ray distributions with high N_F ($\equiv 1/2 \tan\theta_{max}$), it is reasonable to use $\sigma\ 5N_F$ to represent the radiation incident within the tube.

2.2 SURFACE HEAT - AIRSTREAM HEAT CONVERSION

2.2.1 General

Given the surface distribution of input heat fluxes on the receiver structure, the determination of the resulting temperature distributions and heat outputs for an airstream in intimate contact with this structure requires an analysis of many simultaneous local convection, conduction and radiation processes. Adequate computational systems currently exist for the solution of the large numbers of simultaneous nonlinear partial differential equations which result from an adequately fine-grained heat balance formulation.

The particular Finite Element software system selected for this solar receiver analysis was ANSYS, developed by Swanson Analysis Systems of Elizabeth, PA. ANSYS is suitable for both the thermal analyses and the subsequent mechanical stress analysis.

A description of the analysis (Figure 2-4) and of the results is provided in Section 2.2.2. The division of the honeycomb tube into 50 segments was more than adequate to account for the resulting temperature profiles. The implication of accounting for all re-radiation in the first segment is not physically correct, but with the rapid decrease in shape factor for later segments, it is not expected to lead to temperature profiles differing greatly from experiment.

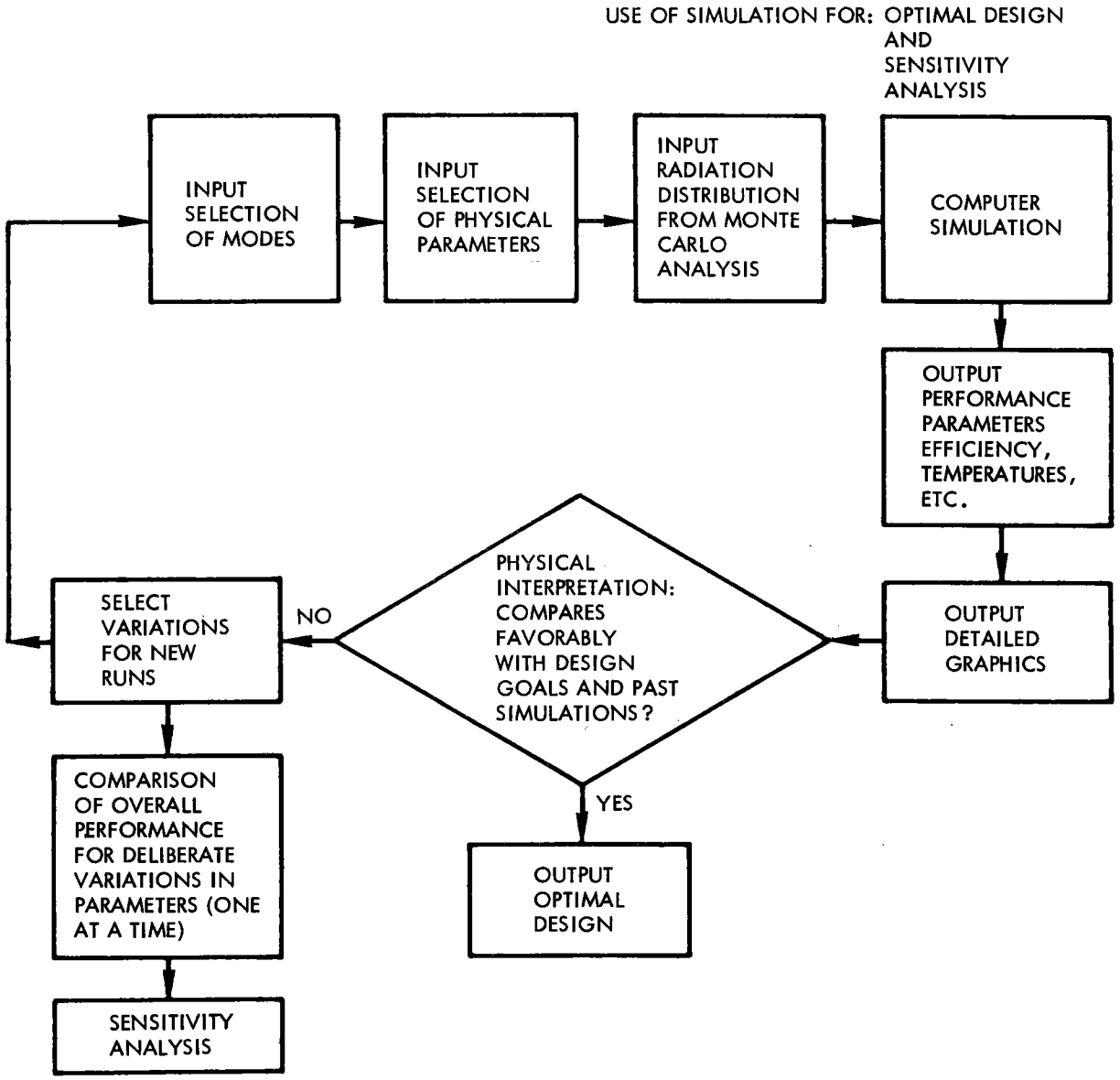

Figure 2-4. Solar Receiver Simulation

2.2.2 Conversion of Radiative Heat to Airstream

2.2.2.1 Single Node Model of Heat Transfer

A heat transfer analysis is arbitrary to the degree that zones which are assumed to be at a single temperature are selected. On one level, one can assume that the entire receiver structure is represented by a single temperature value. Such an analysis of the radiation, convection and conduction inputs and outputs to the receiver can be performed on a fully consistent basis for purposes of representing the overall heat transfer and relating it to parameters such as convection film coefficient (h) and mass flow density ($\dot{m}$). However, such an analysis would not properly deal with maximum temperatures or with location of hot spots on the receiver because a single temperature was chosen to represent the receiver.

Without conflicting in any way with the single node analysis, one can arbitrarily choose a set of temperature zones, set up appropriate heat balance equations for each zone (or temperature node), and have proportionate numbers of simultaneous equations involving the various temperatures as well as the heat flows between nodes. This set of equations is analogous to an electrical network except that the thermal radiation effects are nonlinear in their relation between temperature difference and heat flow. Therefore, mathematically, both matrix inversion and iterative calculations are necessary.

Any single case might be solvable with normal computer programming. However, a developed software system (ANSYS in this case) is general enough in capability to allow for evolutionary studies; i.e., a problem may be formulated and solved initially with a coarse mesh of temperature nodes. Then, as optimization proceeds, more details may be incorporated in the analysis through successively finer meshes of nodes. At a stage where further refinement yields no significant changes, the analysis may be regarded as "converged" and may be discontinued.

2.2.2.2 Simulation

The following conditions were applied to an initial set of simulation runs made on a hypothesized silicon carbide honeycomb tube 3/8" in diameter by 5" long that was used for a preliminary sensitivity analysis. The tube length in the model was deliberately chosen to be oversized so that the analysis could show how heat transfer to the airstream decreases with distance. Subsequent simulation models and experimental designs have been based on the lengths that Figure 2-5 and its counterparts have shown necessary. The tube diameter of 3/8" was chosen based on estimates of the heat transfer coefficient (h). Subsequent analysis has shown an optimal diameter of 0.1".

Using the axial symmetry, the array of nodes and elements was considered to be in a single plane, with appropriate inputs and outputs reduced to a per radian basis; i.e., divided by 2π. This included cross sectional areas, heat flow inputs and outputs, but not material parameters such as conductivities and heat capacities. The result of each run is a printout listing of all node temperatures and the heat flows in each link. These are plotted in Figure 2-5. Figure 2-6 shows the actual input in annotated form for one simulation run.

Temperature variations, along the honeycomb tube and airstream, and the specified radiative heat input, adjusted to fit the Monte Carlo radiation absorption calculation, are also shown in Figure 2-3. An important consequence of the Monte Carlo calculation is that 25% of the total radiation is absorbed at the front face within a depth of 20 radii (for f/1 radiation), which is 3.75" for the hypothetical case illustrated here. The temperature curves illustrate that substantially no further heat is transferred beyond the 2" distance at which the radiative input becomes substantially negligible. The heat flow of Figure 2-7 illustrates some further details of the

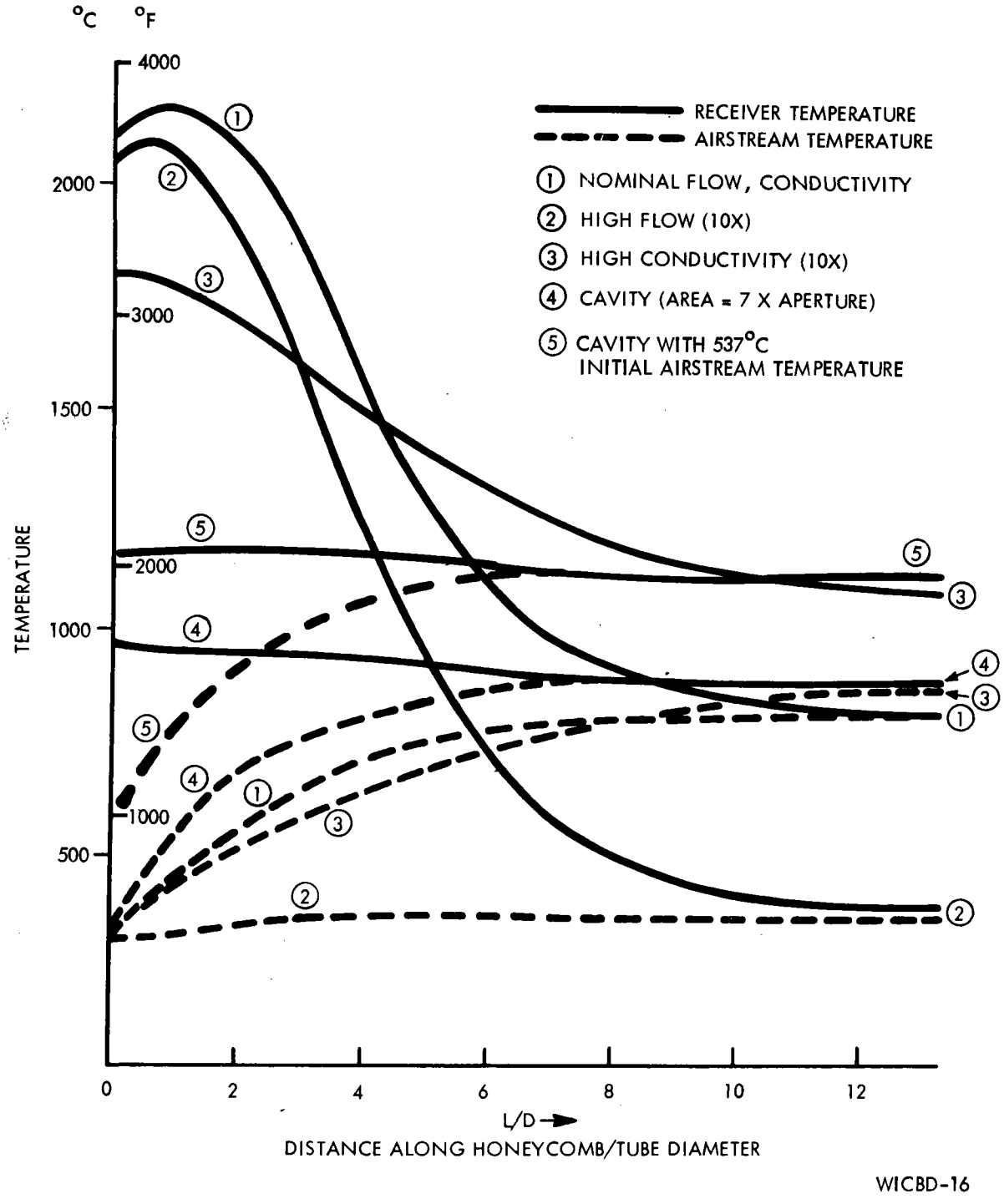

Figure 2-5. Temperatures in Receiver and Airstream

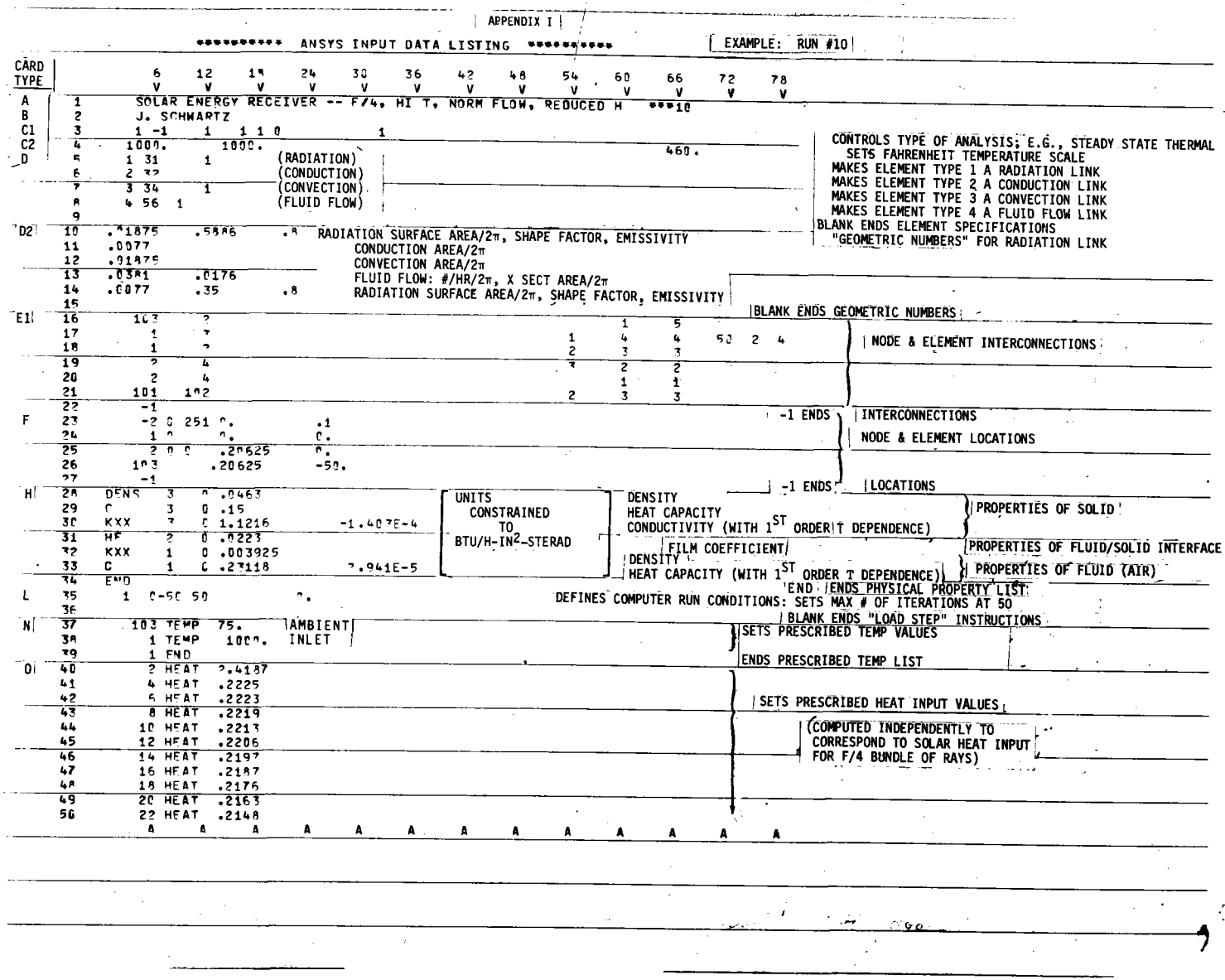

Figure 2-6. Annotated ANSYS Input for One Simulation Run (Sheet 1 Of 2)

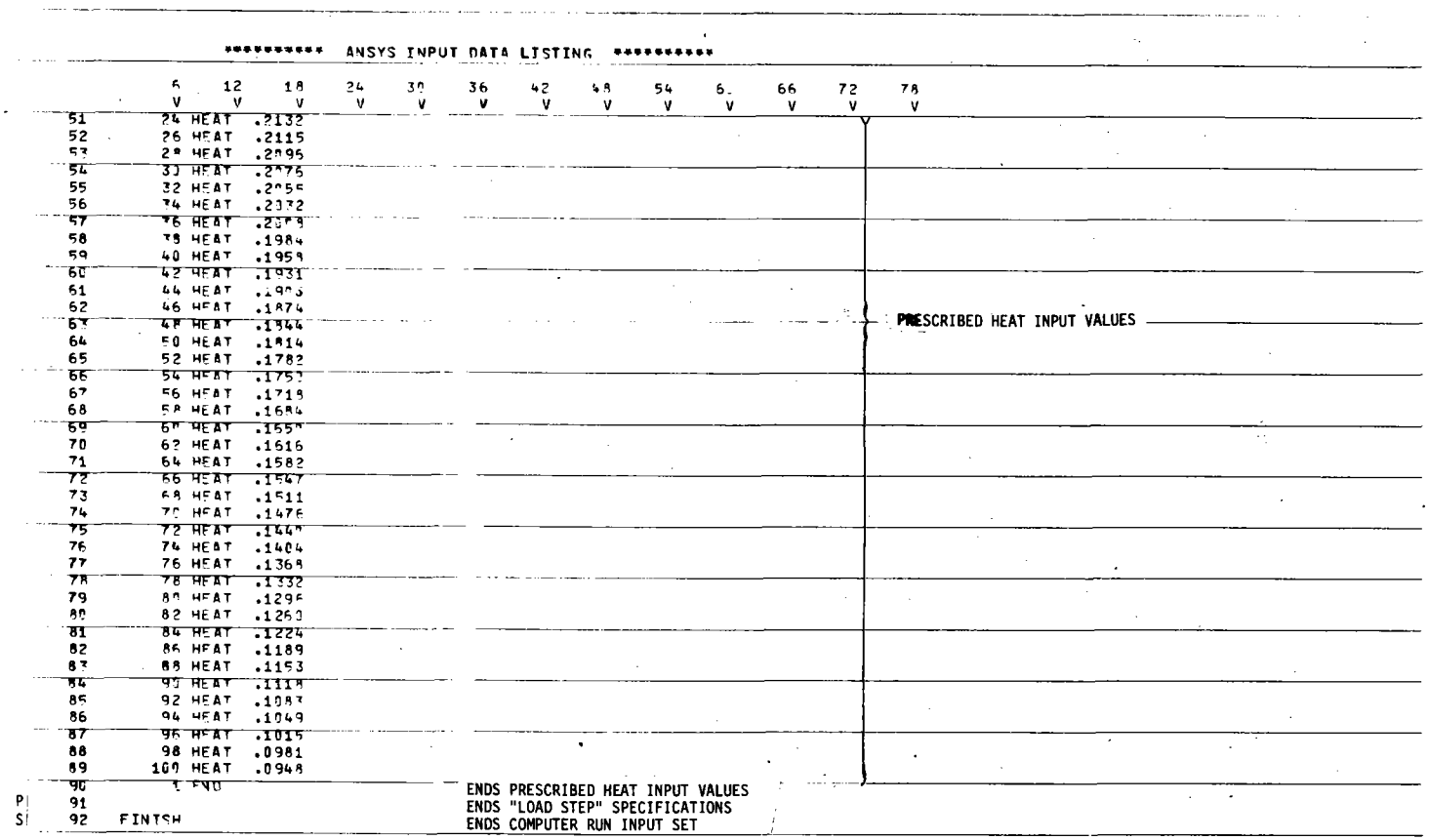

Figure 2-6. Annotated ANSYS Input for One Simulation Run (Sheet 2 of 2)

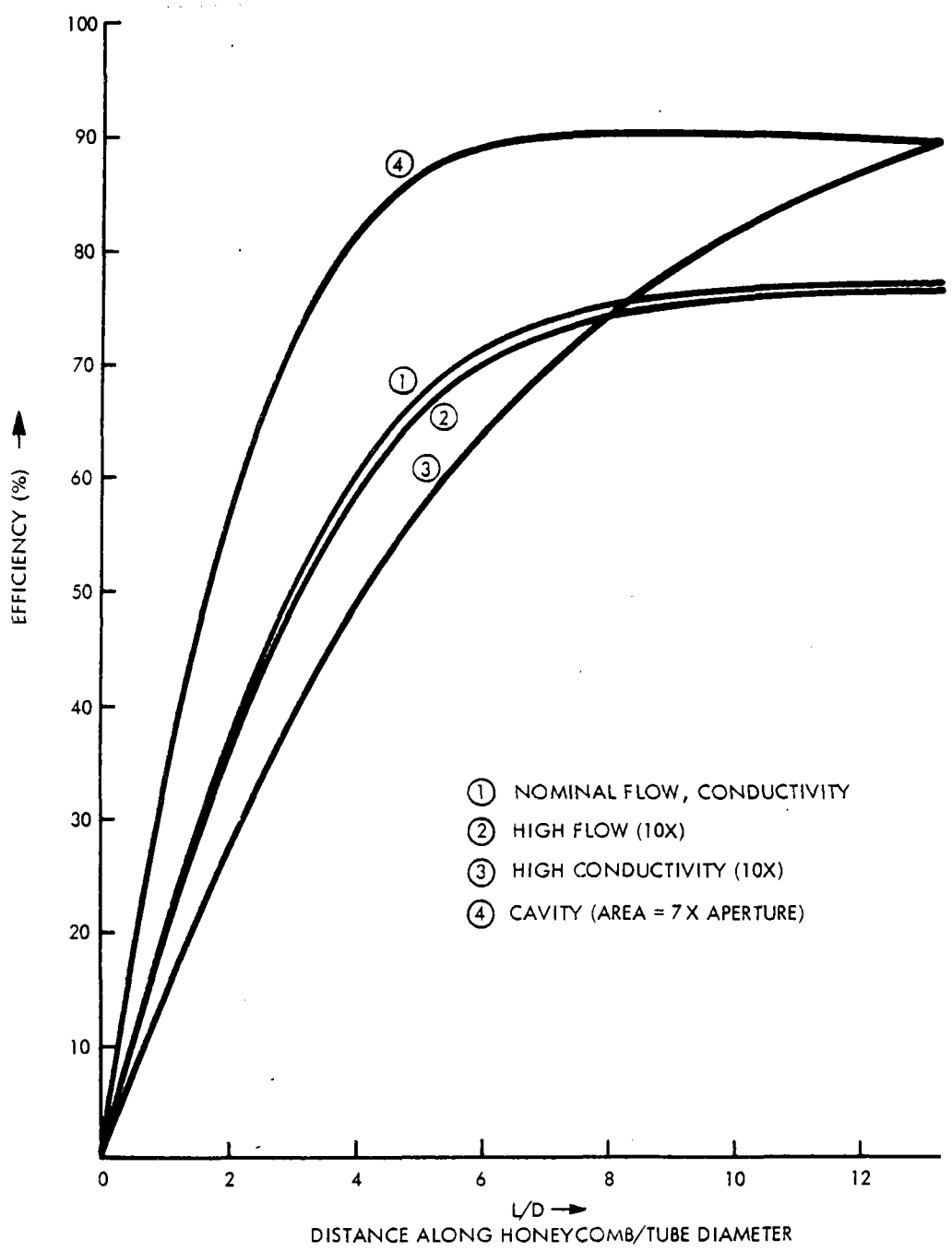

Figure 2-7. Cumulative Heat Collection Efficiency

mechanisms by which heat is transferred and shows the accumulated heat flow (q) in the airstream at each point along the honeycomb. Its final value, related to the solar input, is a measure of the efficiency of the honeycomb in converting radiant energy to heat in the airstream at specified flow conditions.

A more detailed examination of the computer printout illustrates the balance between conductive heat transport, as governed by the conductivity of the honeycomb, versus the absorption and re-emission of radiative energy from one cylindrical segment inside the tube to the next. The run, assuming elevated conductivity (high K), shows how much more heat flow takes place when this channel is more "available". In effect, if the conductivity is sufficiently large, the thermal input is spread effectively over a longer tube length, and higher efficiencies result from the increased convective area that participates in heat transfer.

A set of additional runs was made to indicate sensitivities to the heat transfer coefficient (h), mass flow rate ($\dot{m}$), inlet temperature and f/number. The resulting temperature profiles are shown in Figures 2-8 and 2-9, with numerical summaries in Table 2-2.

The principal conclusions drawn from these simulation runs are that:

- At the assumed solar concentration ratio of 2000, the maximum temperatures at the front of the honeycomb would exceed the 1650^{o}C limit on silicon carbide (above which the material has been found to degrade rapidly); and

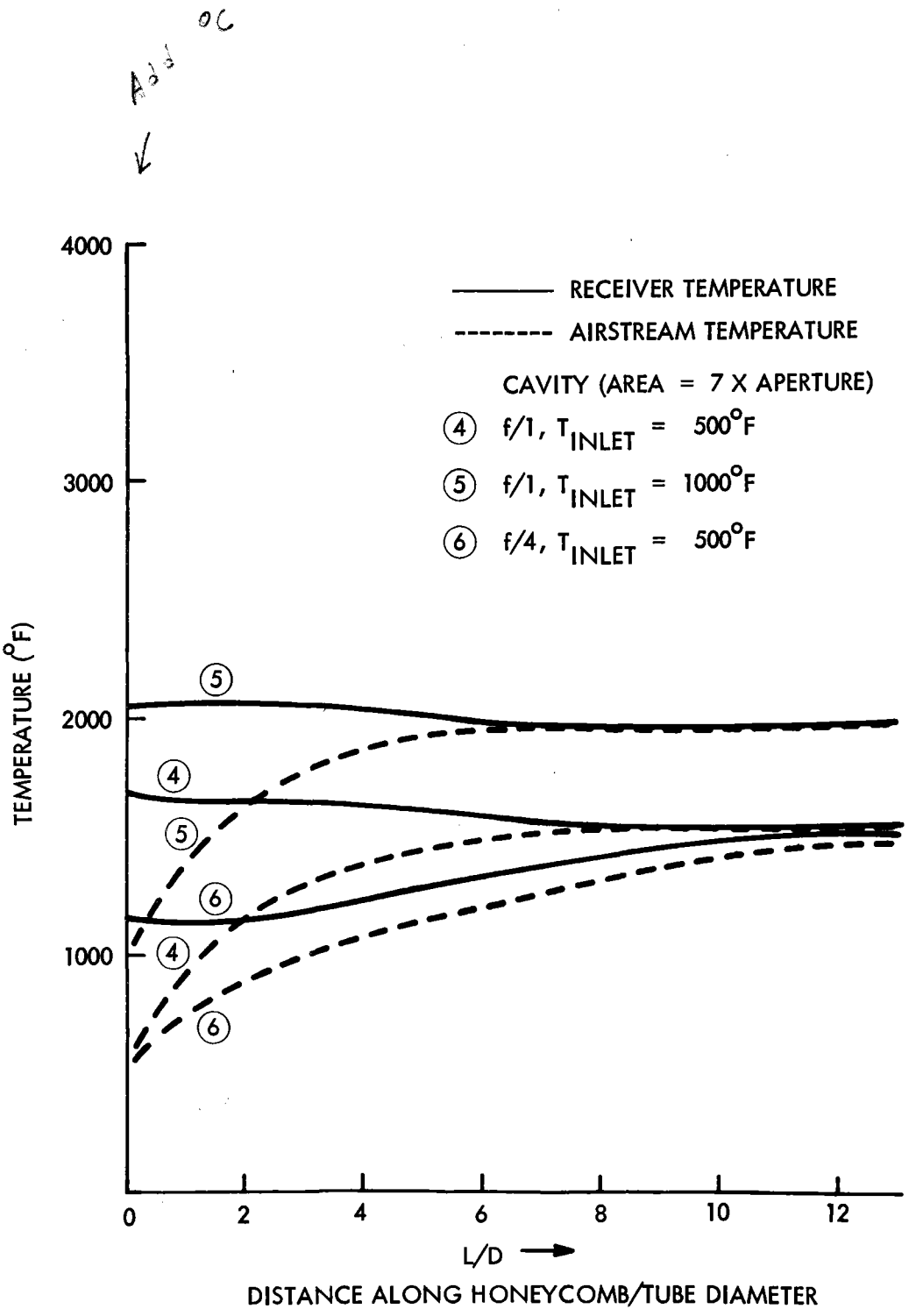

Figure 2-8. Temperature in Honeycomb and Airstream

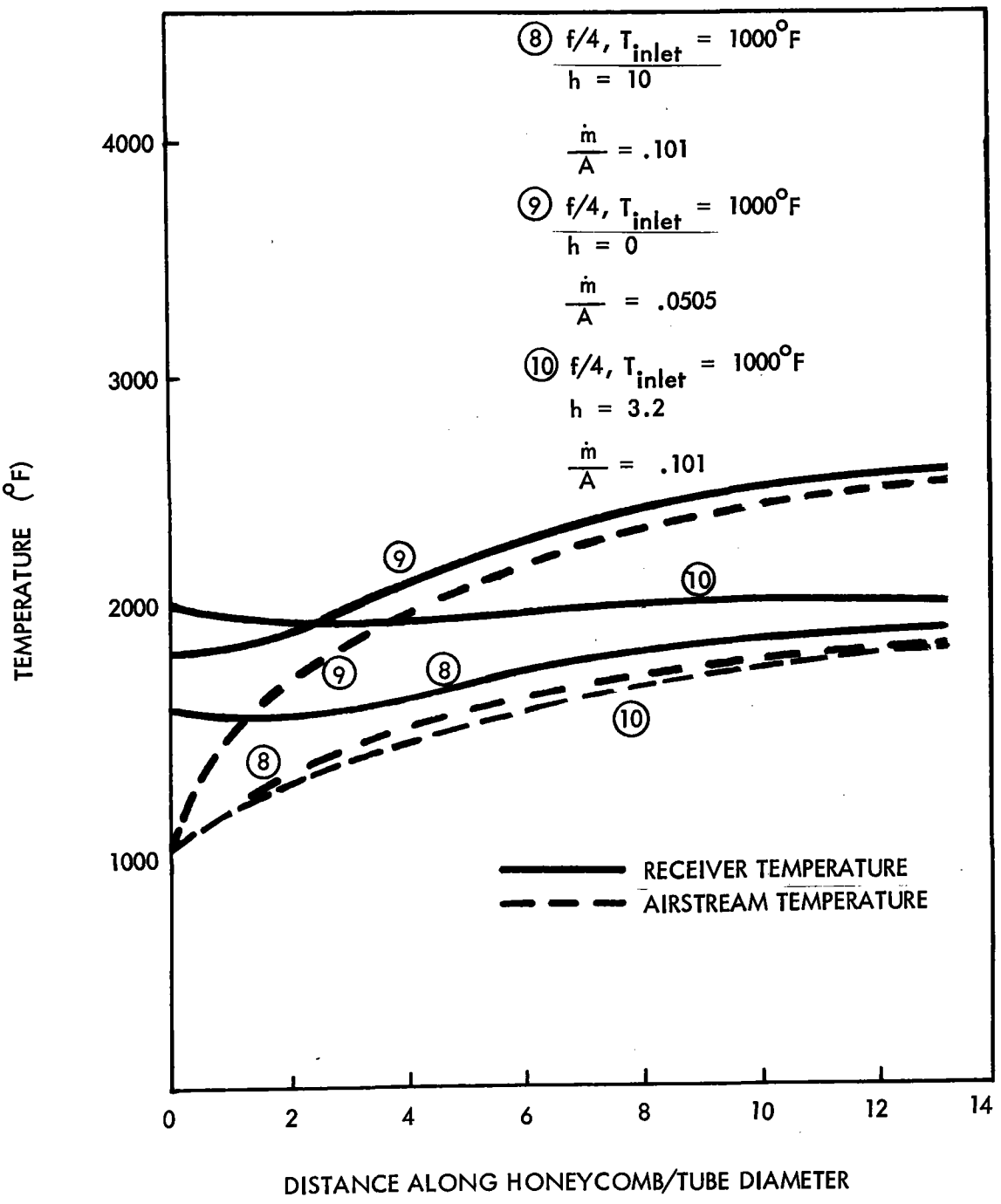

Figure 2-9. Temperature in Receiver and Airstream, Sensitivity to h and ṁ

TABLE 2-2
SUMMARY OF RESULTS

PARAMETERS	COMPUTER RUNS				
INPUTS	5	7	8	9	10
Heat Input Radiation Distribution	F/1	F/1	F/4	F/4	F/4
T_{INLET} (^oC)	538	538	538	538	538
h (Btu/hr-ft^2-^oC)	10	3.2	10.	10.	3.2
FLOW $\frac{\dot{M}}{A}$ (lb/sec-ft^2)	.101	.101	.101	.0505	.101
Outputs					
T_{OUTLET} (^oC)	1078	1072	1062	1448	1136
T_{MAX} (^oC)	1134	1443	1062	1448	1138
$\frac{RADIANT}{AIR}$ efficiency (%)	92.3	87.5	99.9+	95.8	99.2

- Increasing the airflow has little effect in lowering the maximum honeycomb temperature value. This appears to be due to: (a) the very limited capacity of the available convective area to transfer heat to the airstream and, (b) limited conduction. Clearly, the simulated high conductivity case shows that a substantial improvement would occur if this obstacle could be eliminated.

After review of the above data, it was decided to alter the design somewhat to yield a cavity lined with honeycomb and with the holes conducting air outward from the center. Though ultimately this structure would require a change in the simulation model (its mesh topology as well as its geometry in general), initial indications were taken from an adaptation of the foregoing model with the following assumptions:

- A cavity surface area seven times the aperture area. The same total radiation is divided over the increased area, leading to a reduction of the radiative input for a single tube in the model by a factor of seven.

- The same total airflow resulting in a per unit air flow at 1/7 the previous value.

- The shape factor for outgoing reradiation was taken at 1/3 the previous value, largely because the original estimate was judged too high.

Clearly, there are several approximations inherent in this adaptation of the simulation of a single tube model to a cavity model which must ultimately be resolved by simulating some more appropriate meshes. The results provide a clear indication that:

- Distribution of the solar input over a larger area, while keeping the effective area for reradiation constant, substantially lessens the peak temperature.

- The increased available area for convection allows more heat transfer with a reduced difference in temperature between the honeycomb and the airstream.

- With higher values of effective f/number (N_F), the maximum honeycomb temperature may occur at the outlet and be only several degrees above the outlet temperature. In practice, a design that utilizes a relatively high N_F, by keeping the honeycomb at minimal temperature levels, can broaden the variety of materials available for solar applications as well as prolong the useful service life of the honeycomb.

Therefore, while the maximum receiver temperature is lowered, the output airstream temperature and the heat flow efficiency are increased.

A study of Tables 2-2 and 2-3 shows the improved performance with reduced cavity temperature. More detailed analysis will yield local temperature distributions, especially the location of hot spots, control of which will be necessary for a detailed design.

2.3 RECEIVER DESIGN CRITERIA

With A_{AP} as the receiver aperture area, A_H as the effective honeycomb area, and A_{SFCE} as the total active surface area exposed to the flowing airstream and to solar heating (or conduction therefrom), the following guidelines were used:

TABLE 2-3

SUMMARY OF COMPUTER SIMULATIONS (ALL AT SOLAR CONCENTRATION RATIO OF 2000 AT APERTURE)

$\varepsilon = 0.80$

Description	Mass Flow/ Unit Area of Honey-comb	Conductivity	T_R Max (^oC)	T Air Inlet (^oC)	T_R Min (^oC)	T Air Outlet (^oC)	LMTD*	η/e Efficiency of Radiation to Airstream Conversion
Normal	M	K	2110	260	777	766	359	0.780
High Flow	10M	K	2027	260	332	313	385	0.748
High K	M	10K	1738	260	1043	788	696	0.949
Low Flow	0.1M	K	3221	260	3093	2471	1499	0.625
Cavity	M/7	K	910	260	849.66	849.55	74.8	0.926

$$*\text{LMTD} \equiv \frac{(T_{R_{Max}} - T_{Air\ Inlet}) - (T_{R_{Min}} - T_{Air\ Outlet})}{\ln (T_{R_{Max}} - T_{Air\ Inlet}) - \ln (T_{R_{Min}} - T_{Air\ Outlet})}$$

*Log Mean Temperature Difference - this figure is commonly applied in analysis of heat exchangers, though it has no special validity here, except that a high value would be expected to yield higher efficiency at a given air outlet temperature for given surface area.

$$I_{OPTICAL} \equiv \frac{L}{DN_F} \geq \frac{5}{2} \text{ erf}^{-1} \left[\frac{(1+f)\delta_o}{200} \right]$$

where

L = tube length

D = tube diameter

N_F = f/number of incident light rays

This condition assures that less than δ_o% of incident rays do not impinge on the honeycomb. With δ_o = 1% as a reasonable design requirement

$$I_{OPTICAL} = \frac{L}{DN_F} \geq 6$$

assures adequate capture of incident radiation.

Flow index (I_{FLOW}) defined as

$$I_{FLOW} \equiv \frac{\dot{m}c_p}{A_{AP}}$$

is chosen as large as is practical for maximum heat transfer consistent with the constraint that the Graetz number (N_{GR}) is less than 6. Higher flows result in higher circulator pump energy losses.

For honeycomb tubes of length (L) and diameter (D), this requires that:

$$N_{GR} = N_{REYNOLDS} \times N_{PRANDTL} \times \frac{D}{L} \leq 6$$

$$= \left(\frac{M}{A_H} \quad \frac{D}{\mu}\right) \frac{c_p \mu}{k} \quad \frac{D}{L} \leq 6$$

$$= \frac{\dot{m} c_p}{A_H} \frac{D^2}{kL} \leq 6$$

Thus

$$I_{FLOW} \leq \frac{6kL}{c_p D^2} r_c = \frac{6kL}{D^2} \quad \frac{A_H}{A_{AP}}$$

or

$$\dot{m} \leq \frac{6kL}{c_p D^2} A_H$$

For the convective index (I_{CONV})

$$I_{CONV} \equiv \frac{U_{eff} A_{SFCE}}{A_{AP}} = \frac{\zeta h A_{SFCE}}{A_{AP}}$$

where

$$\zeta = \frac{U_{eff}}{h}$$

is chosen as 2 x I_{FLOW} for optimal conversion efficiency:

$$I_{CONV} = 2\ I_{FLOW}$$

A preliminary analysis of this condition, illustrated in Figure 2-10, shows that the heat transfer efficiency tends to level off at the recommended maximum. Raising I_{CONV} generally requires a larger cavity, incurring proportionately larger costs. Beyond the recommended level, performance increases will be relatively small and reduced values of I_{CONV} will cause marked degradations in performance. In general, the finer the honeycomb, the easier it is to meet or exceed the convective index guideline, primarily because of the larger values for h and U_{eff}. These larger values result from the Graetz mechanism of heat transport. For laminar flow ($N_{GR} < 6$), this mechanism is based on the conductivity of the fluid and is more effective for smaller diameters, even if the total surface area is kept fixed.

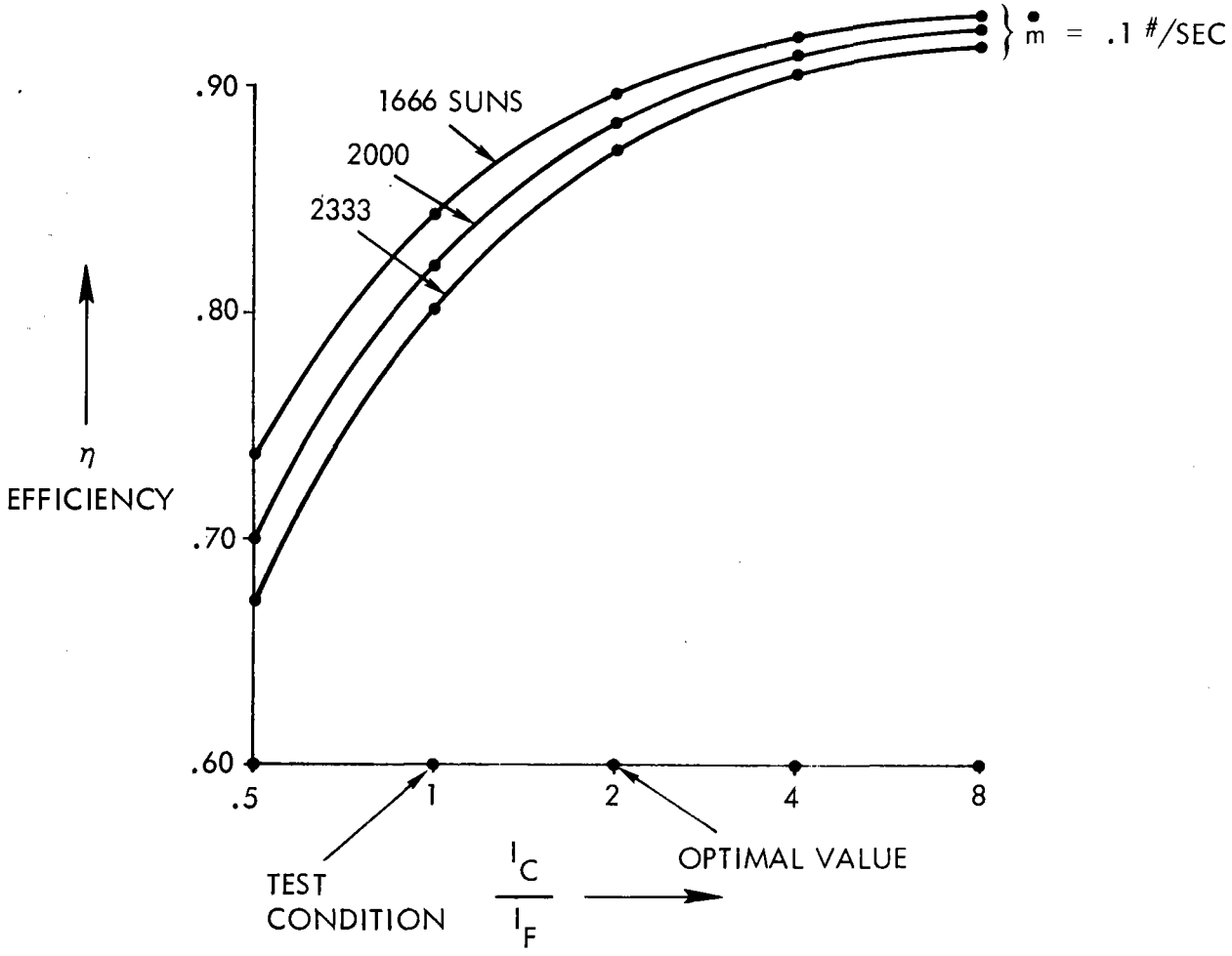

SENSITIVITY OF RECEIVER CONVERSION EFFICIENCY TO CONVECTIVE INDEX/FLOW INDEX NEAR WHITE SANDS TEST CONDITIONS (BASED ON SIMPLIFIED MODEL CALCULATIONS)

Figure 2-10. Heat Transfer Efficiency

SECTION 3
EXPERIMENT

3.1 RECEIVER DESIGN

3.1.1 Description

The receiver unit is constructed of temperature-resistant steel alloys and high-temperature insulation. Solar radiation entering a quartz window on one end impinges on an internal ceramic honeycomb absorber. A series of external radiation shields prevents solar energy spill from striking the metal housing. Heated compressed air, simulating the conditions appropriate to the Brayton cycle turbine, is supplied to the receiver where it is further heated while flowing through the honeycomb absorber. This air is exhausted from the unit through a small opening which maintains the internal pressure of the unit at the required level.

3.1.2 Operation Parameters

Design operating parameters of the receiver are as follows:

- Input Power: 15 kW (thermal input)
- Airflow Rate: 0.32 kg/sec
- Input Air Temperature $621^{o}C$
- Output Air Temperature $927^{o}C$
- Internal Pressure 3.1×10^{4} dyne/cm^{2} (45 psig)

3.2 WHITE SANDS FACILITY

The solar furnace used for this experiment is the U.S. Army White Sands solar furnace shown in Figure 3-1. This facility was designed to provide a high radiant flux to simulate the thermal output of nuclear weapons for testing military equipment. Originally designed for 35 kW, the system is currently capable of delivering approximately 27 kW of radiant energy.

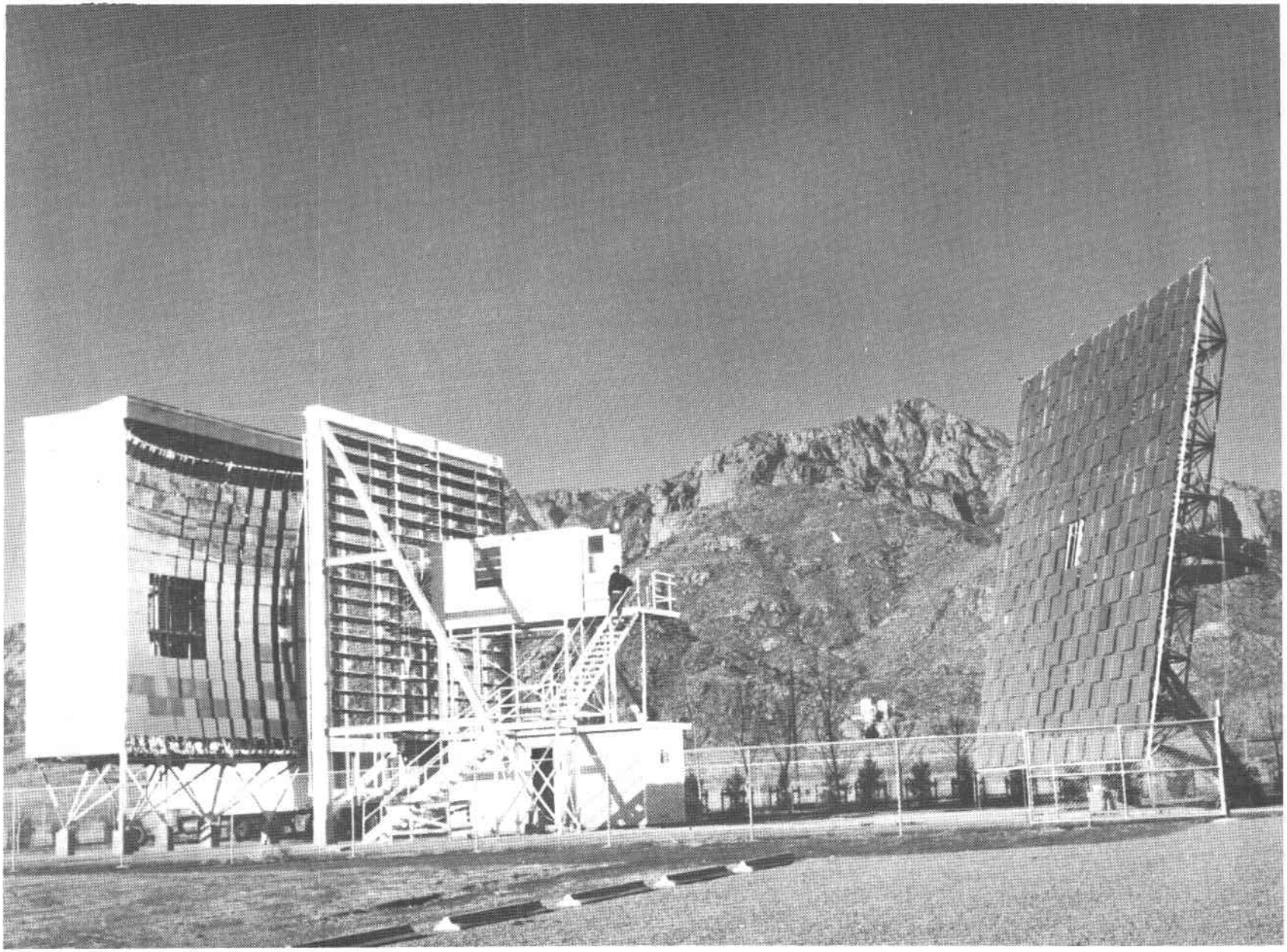

Figure 3-1. White Sands Solar Furnace

3.3 TEST APPARATUS AND INSTRUMENTATION

The system under test consists of the receiver unit, the air heater unit, control and instrument panel, and a power distribution box. The functional interrelationship of the items is indicated in Figure 3-2. Figure 3-3 presents a photograph of the equipment installed at the White Sands solar furnace.

3.3.1 Airflow Rate (lb/sec)

The airflow rate through the system was measured by the flow meter (F). The weight flow of air (W) (lb/sec) is related to the indicated SCFM reading (F), the input pressure (P_1) psia, and temperature (T_{20})^{o}R, by the equation:

$$W = 0.00772F\sqrt{\frac{P_1}{T_{20}}}$$

The factor 0.00772 accounts for the calibration of the meter.

3.3.2 Temperature

Temperatures were measured using chrome-alumel exposed junction thermocouples. The individual junctions were read out on a 20-position digital pyranometer matched to the thermocouple characteristics. Exposed junctions were shielded from the effects of direct radiant heating.

3.3.3 Air Outlet Temperature

Two methods were provided to obtain the temperature of the air after it had been heated by the solar radiation. The first consisted of a thermocouple (T4) located on the centerline of the receiver outlet where it would be exposed to a well mixed flow. Possible

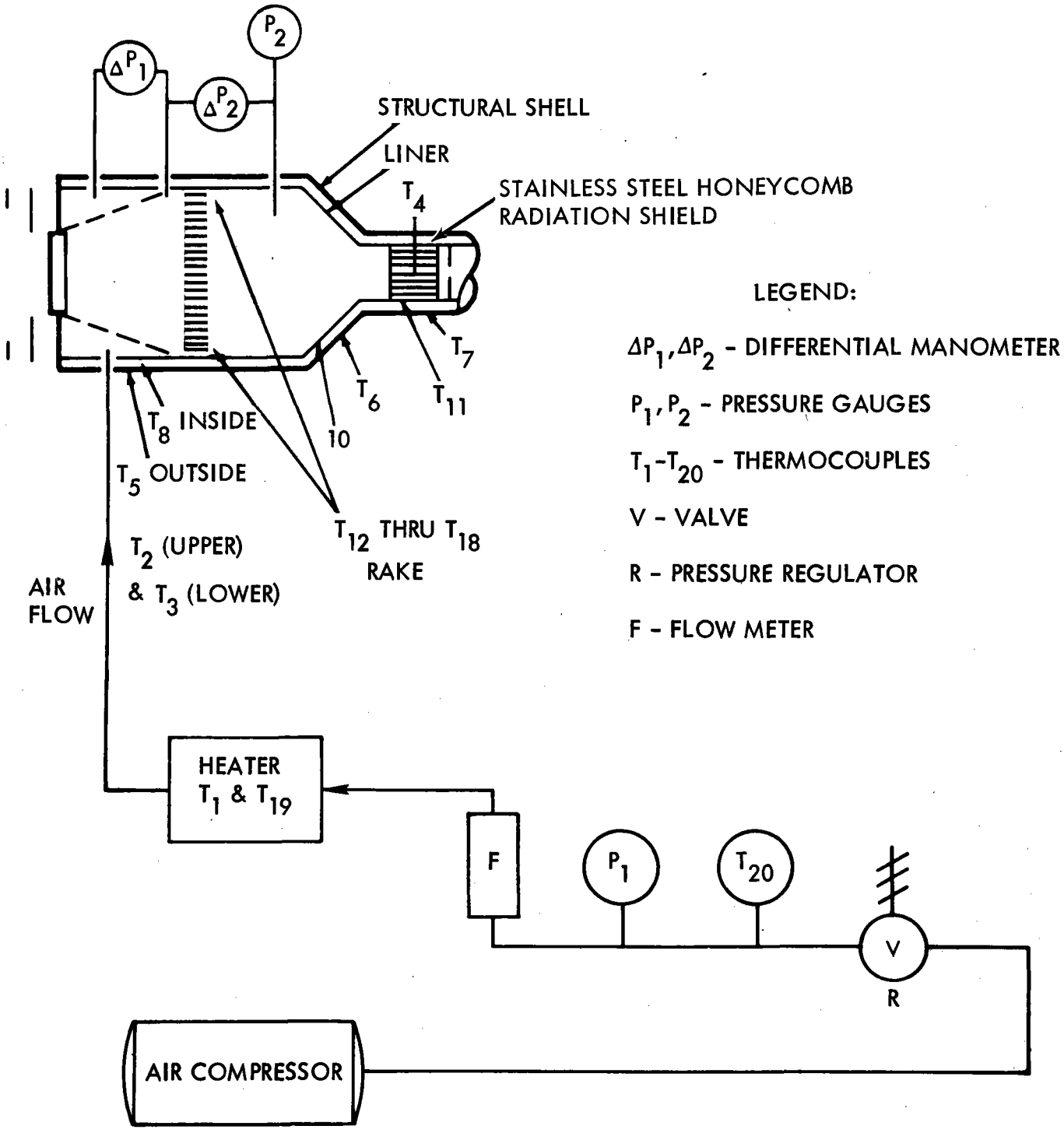

Figure 3-2. Instrumentation Layout

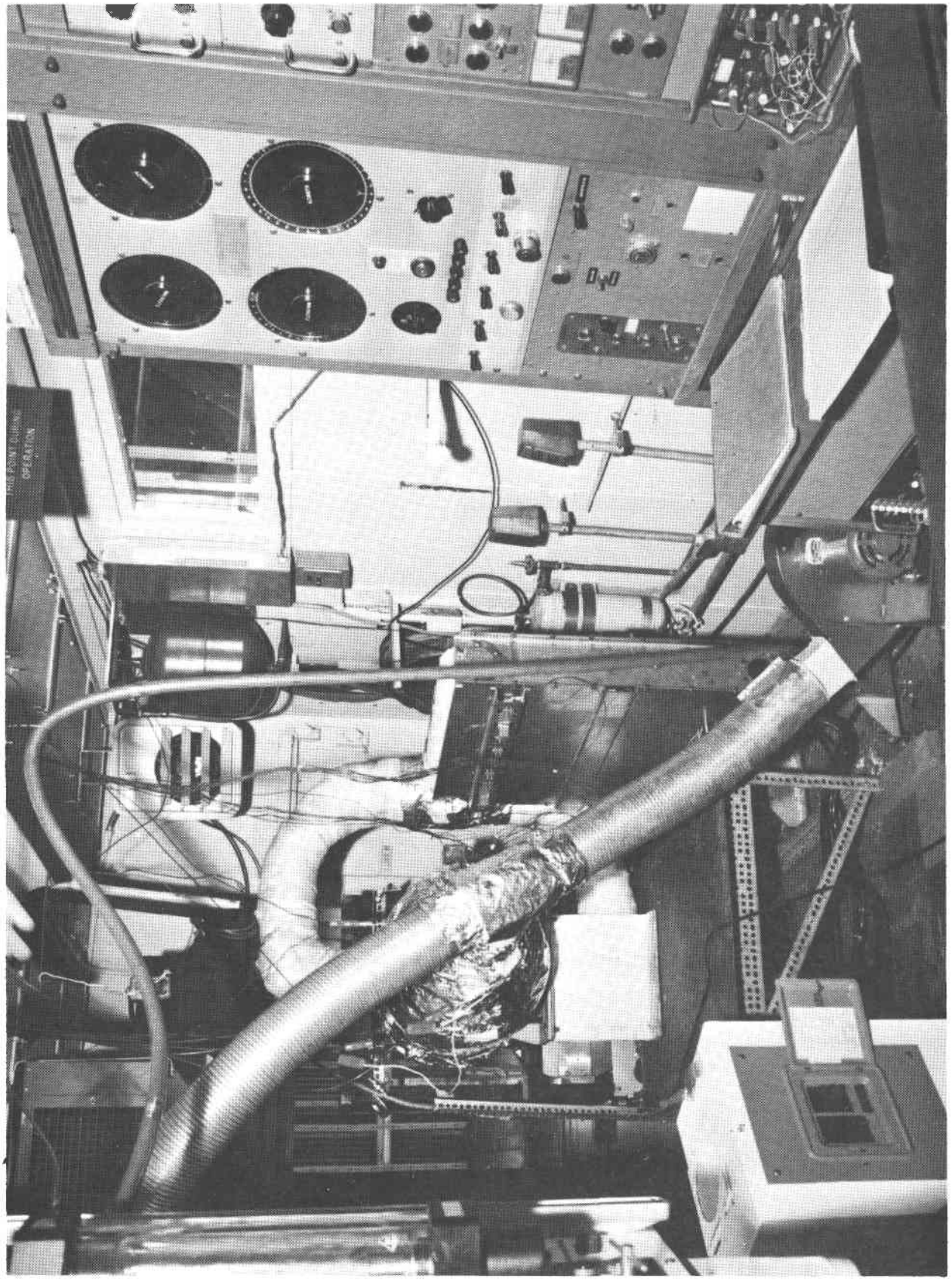

Figure 3-3. Equipment Installed at White Sands Solar Furnace

errors due to radiation losses were minimized by interposing a thin-walled, stainless-steel honeycomb between the thermocouple junction and the receiver wall. A second measure was obtained from a 7-thermocouple rake (T12 through T18) located on the horizontal centerline 7.62 cm downstream of the matrix.

3.4 TEST PROCEDURE

3.4.1 Calibration

The first series of tests, conducted on 5 and 6 August 1976, were calibration tests to determine the amount of radiant flux impinging on the window and the matrix in subsequent receiver runs. This was accomplished by scanning the flux distribution in the appropriate vertical plane using a Hycal scanning calorimeter. This data was then used to construct maps of flux contours such as those shown in Figures 3-4 and 3-5. Based on these maps, the relation showing total solar power as a function of direct solar flux and attenuator settings is shown in Figure 3-6, which gives the incident power in Btu/sec for the matrix at two different receiver positions. Calibration constants were:

$$1 \text{ mw} = 3.5 \text{ cal/cm}^2\text{-sec} \quad \text{(Hycal Calorimeter)}$$

$$\left.\begin{aligned} 72 \text{ mw-cm}^2 &= 1 \text{ Btu/sec} \\ 68 \text{ mw-cm}^2 &= 1 \text{ kW} \end{aligned}\right\} \quad \text{Integrated Flux Values}$$

In addition to the radiant input calibrations discussed above, it was also necessary to develop a calibration method to account for energy losses from the receiver due to conduction through the walls to the ambient environment. This correction is required to isolate the effect of the honeycomb and permit correlation of scaling parameters with theoretical estimates. Furthermore, the small size of the test unit precluded the use of the same insulation techniques which would be used in full scale units, and resulted in a much

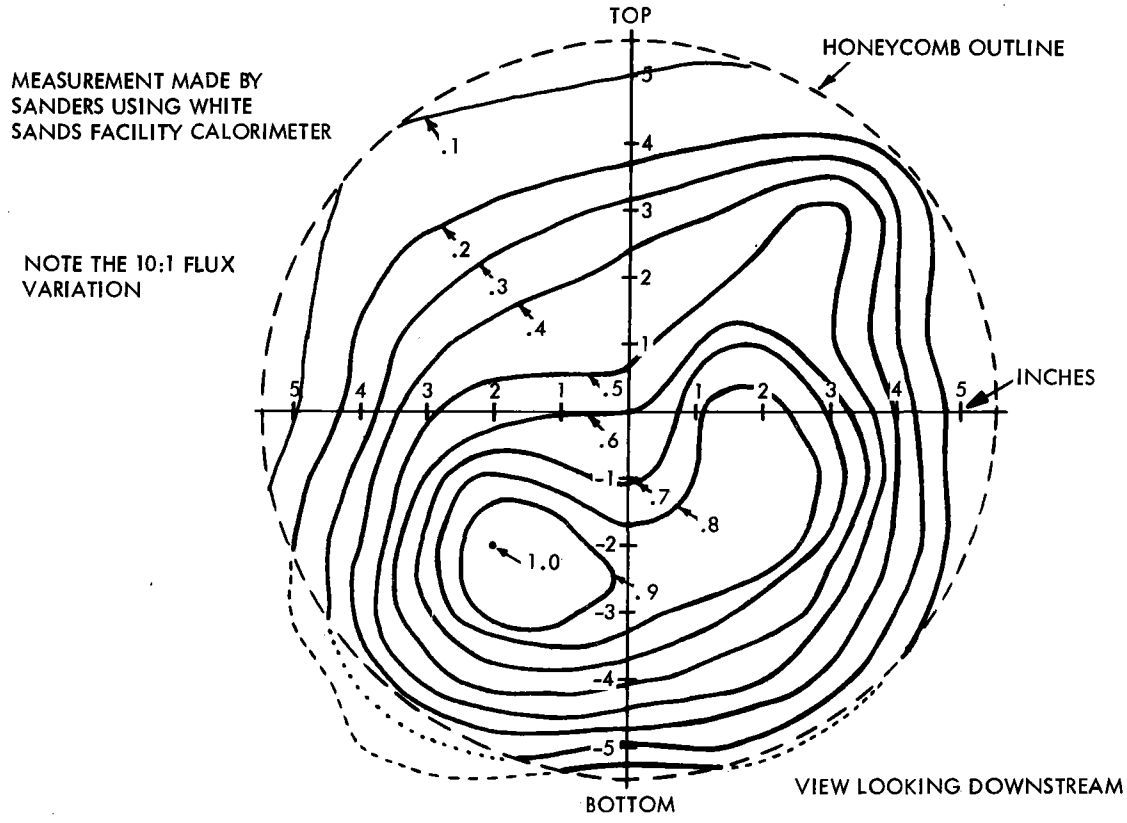

Figure 3-4. Isoflux Map at Honeycomb Surface (Window at Focal Point)

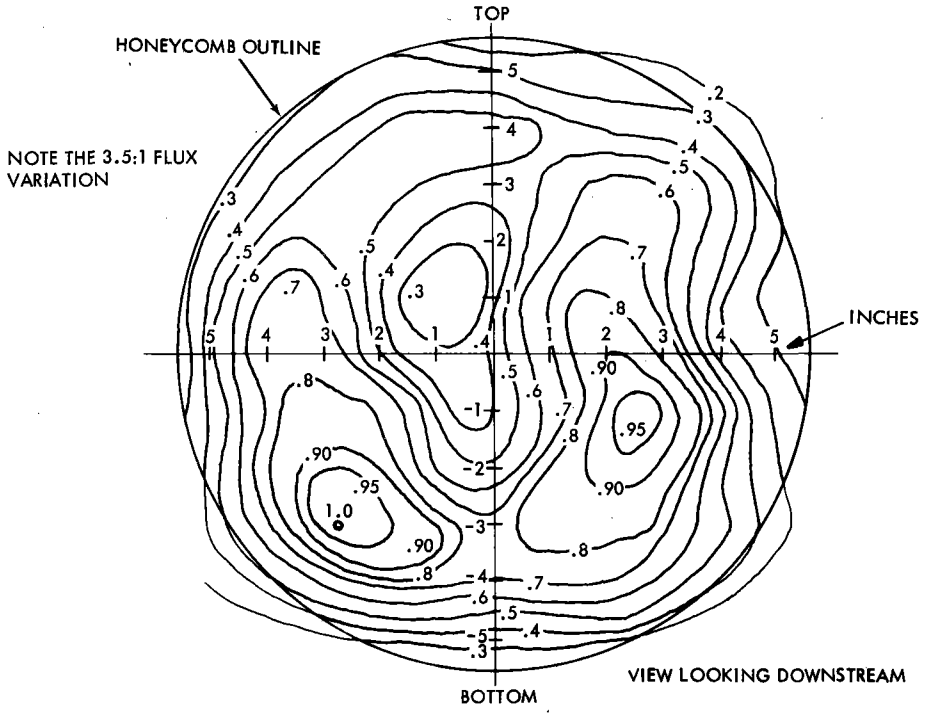

Figure 3-5. Isoflux Map at Honeycomb Surface with Window 4-1/4 inches aft of Focal Plane

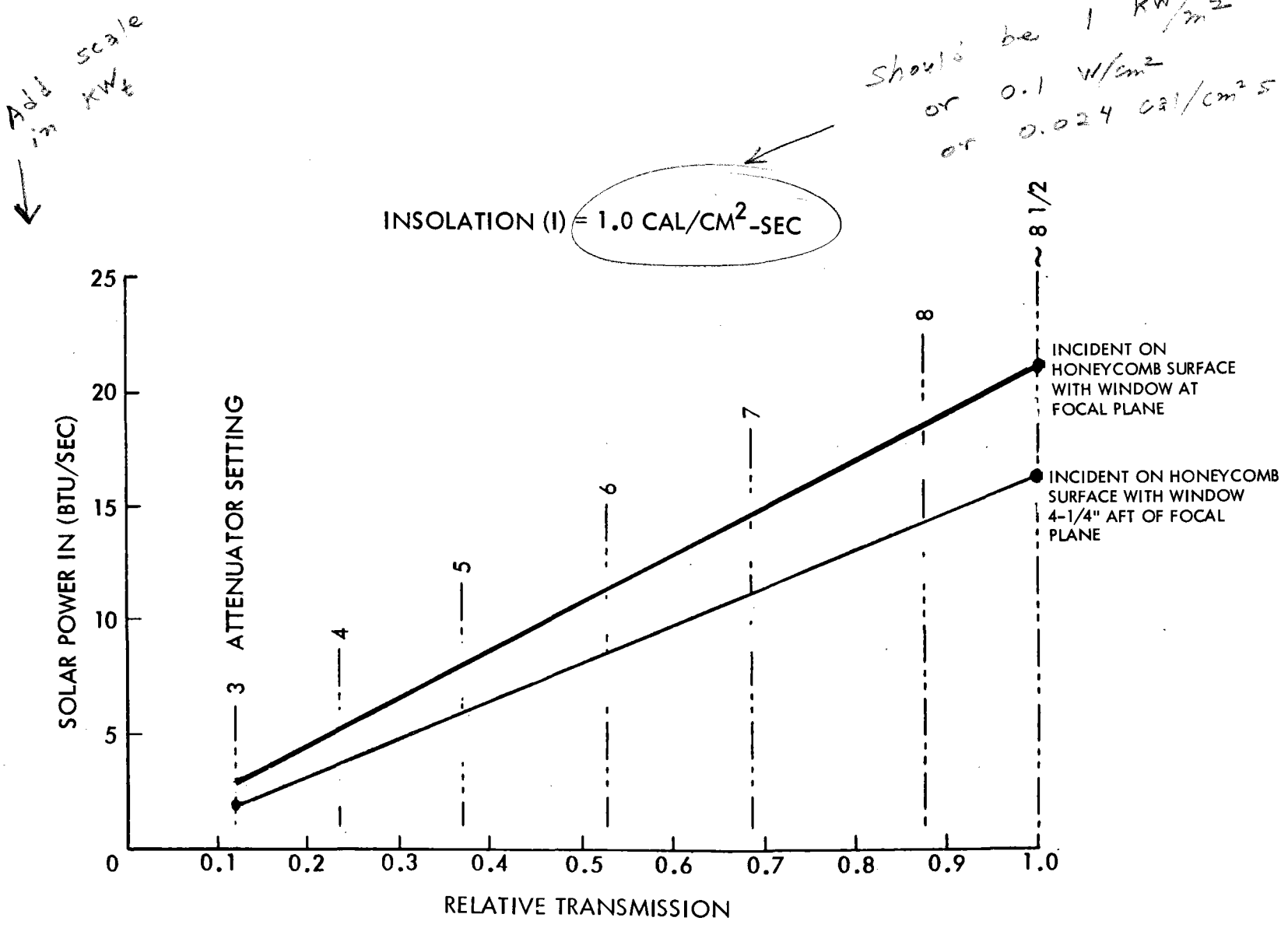

Figure 3-6. Input Solar Power versus Attenuator Transmission

greater percentage of heat losses. The heat loss calibrations consisted of a number of sun-off runs during which the input air temperature, flow rate and pressure were varied. Outlet air temperatures, which were lower than the input temperature due to heat loss, were recorded. From these records, graphs of temperature drop as a function of input conditions were developed. This temperature correction ranged from 22.2°C to 55.6°C, and was typically 38.9°C at design conditions.

3.4.2 Testing

The most effective test procedure, which evolved after a few days of operating experience, began by stabilizing the internal temperature of the receiver at the test operating temperature. This required at least 1 hour, with input air at approximately 480°C and 0.0432 kg/sec (0.095 lb/sec). Periodic temperature readings were made; stability was assumed when the output temperature did not vary by more than 2 to 3 degrees over a 5 minute period.

When stability was reached, the heliostat was brought into automatic tracking with the attenuators closed and the water-cooled shutter raised in front of the receiver. Correct alignment was visually verified by slightly opening the attenuators and observing the position of the concentrated flux on the shutter. The attenuator was then opened to the first test point, usually the lowest setting of interest, the shutter lowered, and the solar flux entered the receiver. While the receiver reached a new equilibrium point, input conditions (temperature and flow rate) were maintained constant. During the test, solar input was monitored by recording both the output of a total reading pyranometer and a manually-positioned pyrheliometer, the latter was used to obtain the direct flux vector required to estimate the input energy. Periodic readings of the diffuse solar component and sun elevation angle were also manually recorded.

A period of approximately 20 to 30 minutes was required to reach the sun-on equilibrium point, during which time the thermocouple temperatures, airflow parameters, solar inputs and heater performance were periodically recorded. After equilibrium was reached and the final data set recorded, the attenuator was opened further, increasing the solar energy into the receiver, and the process then repeated.

3.5 RESULTS

3.5.1 Method of Data Reduction

The basic performance features of interest are: the obtained temperature increase (ΔT), the heat exchanger efficiency (η), and the pressure drop across the honeycomb (ΔP_2).

The temperature increase (ΔT) of the air due to the input solar radiation was obtained by the relationship:

$$\Delta T = T_{out} - T_{in} + \Delta T_L$$

where

T_{out} = Outlet air temperature, obtained either by the average of the seven rake temperatures, or from the exit centerline thermocouple #4

t_{in} = Inlet air temperature, obtained by averaging the upper and lower supply pipe inlet temperatures: T.C. #2 and T.C. #3

ΔT_L = Wall heat loss correction factor, illustrated in Figure 3-7

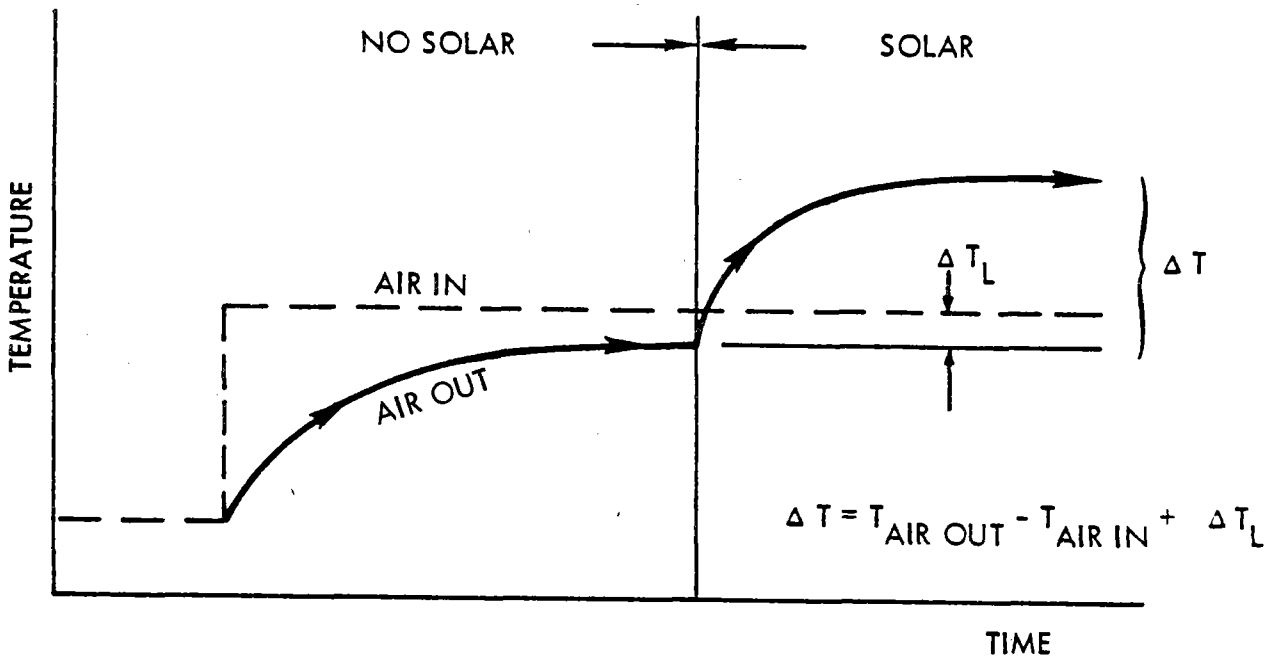

Figure 3-7. System Thermal Transient Response

The receiver efficiency (η) is defined on an incremental basis as:

$$\eta = \frac{\text{energy added to airstream}}{\text{solar power input}}$$

$$\eta = \frac{\dot{m}\ C_p\ \Delta_T}{\dot{Q}_{in}}$$

where $\dot{m}$ = mass flow rate (lb/hr), and $\dot{Q}_{in}$ = solar power incident on the matrix surface. (Approximately 90% of the energy incident on the window impinges on the matrix.) $\dot{Q}_{in}$ is obtained as determined by calibration from Figure 3-6, or from the formulas below:

$$\dot{Q}_{in} = \dot{Q}_o \frac{I\ T}{I_o T_o}$$

$$= 21.69\ IT \text{ (for runs in the forward position) (Btu/sec)}$$

$$= 16.29\ IT \text{ (for runs in the aft position) (Btu/sec)}$$

where the subscript o refers to calibration conditions, I to direct solar flux, and T to attenuator transmission.

3.5.1.1 Position FWD versus AFT

This variable refers to the position of the receiver with respect to the focal plane of the solar furnace. The designation FORWARD (FWD) denotes the placement of the receiver so that the window (or aperture) is at the focal plane, while the designation AFT places the window 11.4 cm (4.5 in) behind the focal plane. This position variable was unanticipated; the initial test plan considered only one position, FORWARD. However, tests at the AFT location were added when the results of the flux calibration test disclosed larger than expected variations in flux intensity over the matrix surface in the forward position.

Figure 3-8 illustrates the effect of air inlet temperature on efficiency. The efficiency (η) is defined as heat gained by the air-stream divided by input solar energy. As expected, efficiencies decrease with increasing inlet temperatures.

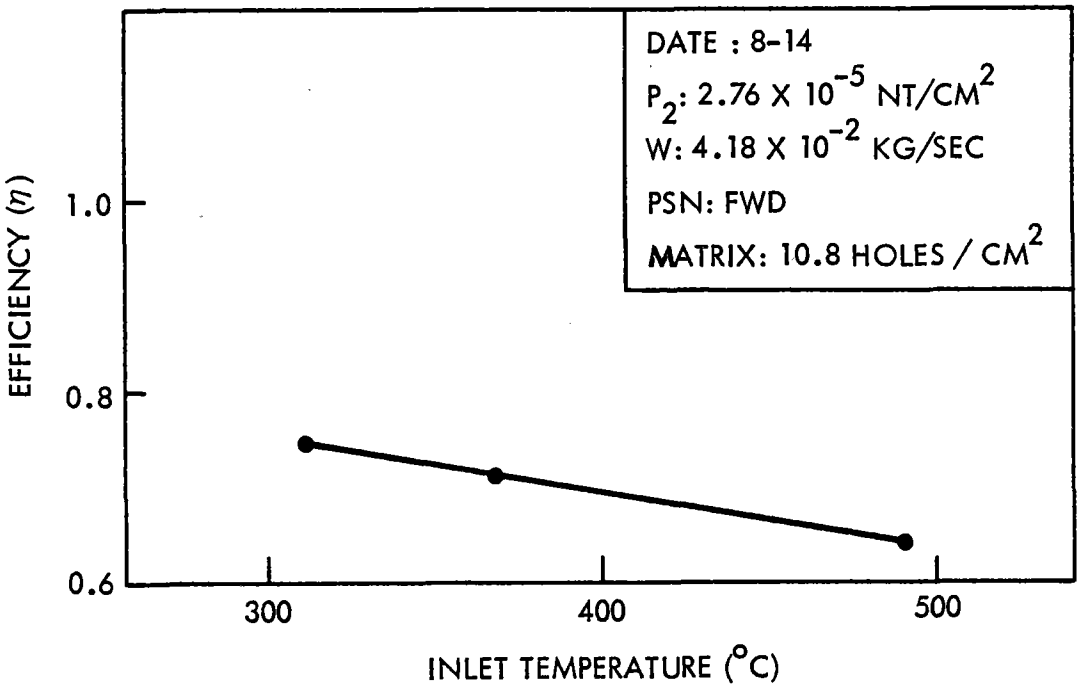

Figure 3-8. Efficiency versus Inlet Temperature

The efficiency increase obtained in the AFT location is attributed to the more uniform flux distribution at that location. (Figure 3-5 shows a 3.5:1 variation over the matrix in the AFT position, while a 10:1 variation exists over the surface in the forward location, as shown in Figure 3-4.)

3.5.1.2 Pressurized versus Unpressurized

Comparisons between pressurized and unpressurized runs with similar conditions show no notable difference. There is a tendency toward higher efficiencies in some of the pressurized data; but the increase does not exceed 5% and could be related to inhomogeneous flux effects being moderated by pressure, as much as to any direct contributions to efficiency.

3.5.2 Correlation with Computer Model

A simplified, single node heat balance was performed for use as a semi-empirical curve fit for the data, especially for outlet air temperature rise and efficiency comparisons. For many data points, the fit has been good even when nominal solar flux values were used, with no special accounting in the model for the flux inhomogenities in the real situation.

One use of this model in fitting the data is to show isolated points that are out of line with the main body of data in a particular run, providing a counterpart of the averaging of single run data. Comparison with these semi-empirical curve fits can help identify "possibly erroneous points". Figures 3-9 and 3-10 show some comparisons of data from various experimental runs with the model.

3.5.3 Infrared Scanner Results

In order to obtain temperature information on the SiC matrix, an infrared scanner was used to monitor the matrix temperature

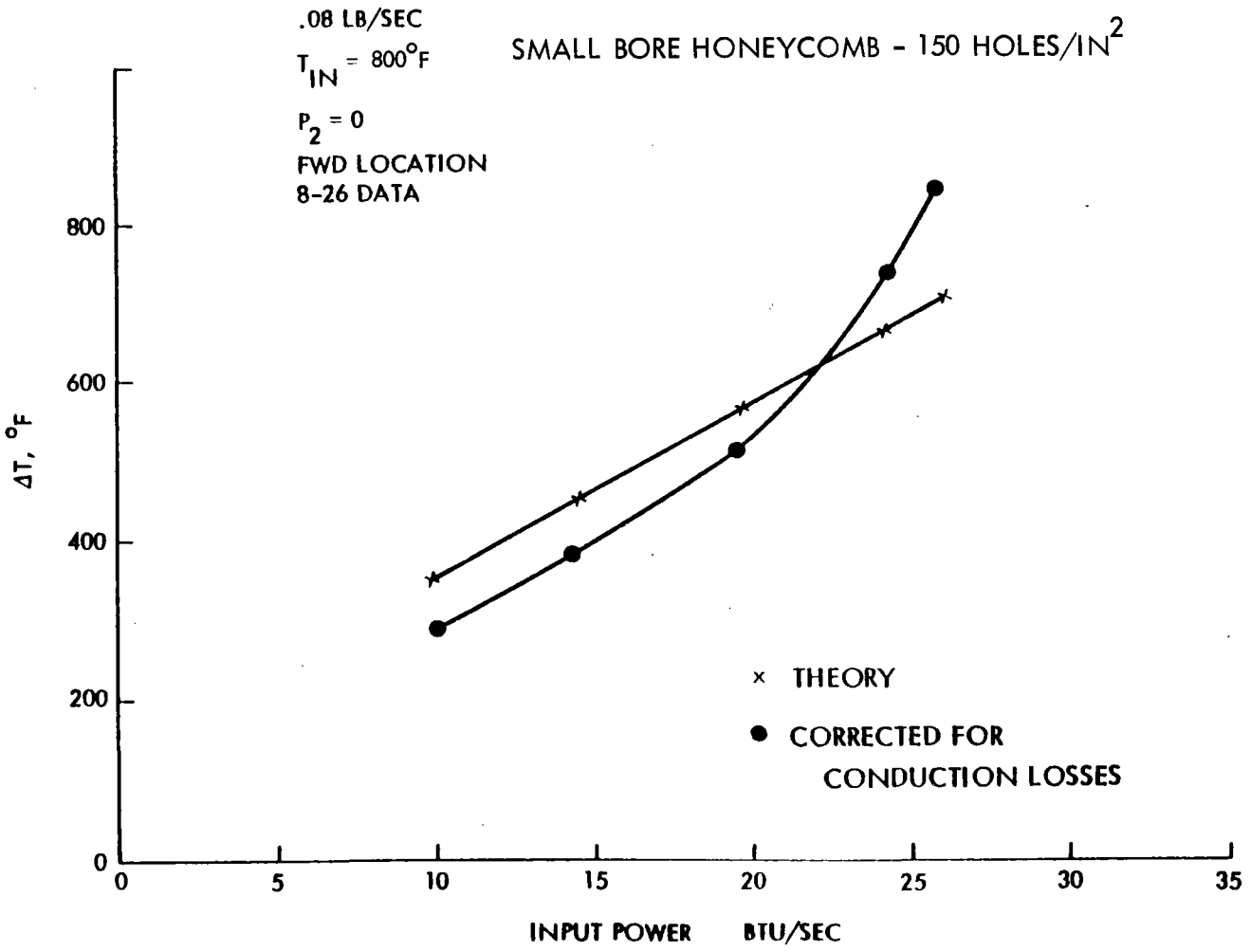

Figure 3-9. Temperature Increase versus Input Power

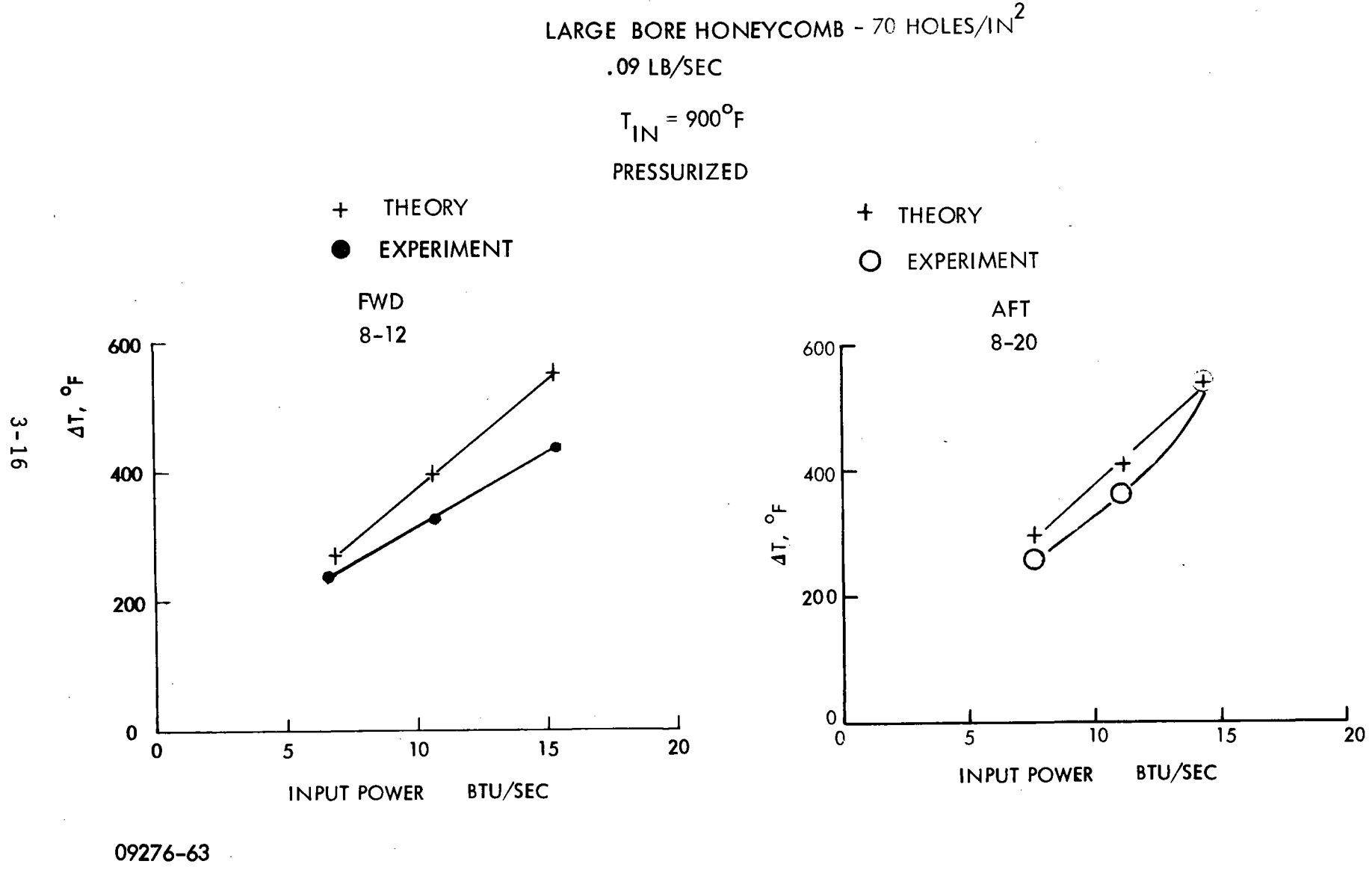

Figure 3-10. Temperature Increase versus Input Power

distribution during operation. The experimental setup is shown in Figure 3-11. The infrared scanner was placed directly in front of the receiver and aligned to view the matrix through the quartz window. A solar-blind response filter (2.75-2.85μ) was placed in front of the scanner. The infrared scanner was operated in the 2.75-2.85μ band because: (a) the quartz has a high transmission at this wavelength allowing the scanner to view the matrix through the window, and (b) the 2.6-3.0μ atmospheric water absorption band greatly attenuates incoming solar radiation, preventing interference due to reflected solar energy during operation.

The calibration curve for the scanner measured using an NBS traceable blackbody is shown in Figure 3-12. This calibration was made with the quartz window used in the White Sands tests inserted in the optical path to account for reflection and absorption. Figure 3-13 illustrates the real-time infrared images obtained using this system. The bright outline is an electronically-controlled isotherm which can be adjusted to outline the temperature contour of interest. As used in Figure 3-13, the system allows a general view of the front surface temperature of the silicon carbide matrix. The hottest spot on the ceramic matrix is shown in Figure 3-13a. Figures 3-13b to 13f show progressively lower temperature regions.

The information can also be displayed in a single line scan mode where each raster line of the image is viewed with the amplitude representing the temperature (Figure 3-14). This is a particularly useful mode because it allows quantitative measurements of the matrix surface temperature. In Figure 3-14, the object is scanned from bottom to top; i.e., Figure 3-14a is a scan of the lowest position of the honeycomb and Figure 3-14p is the top of the honeycomb. This information can be used to determine how efficiently the material is being used in a specific cavity design.

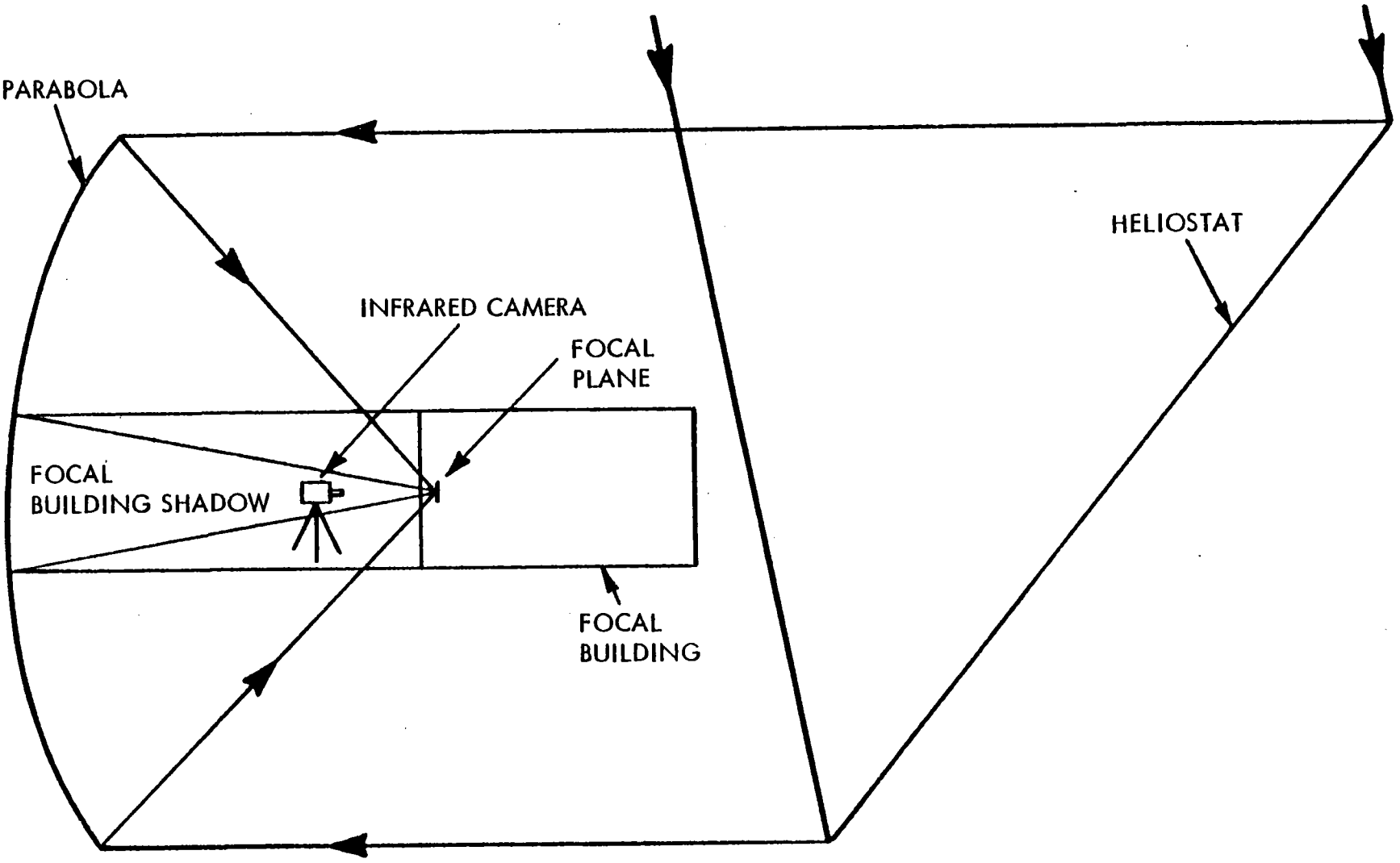

Figure 3-11. Infrared Imaging Camera Experimental Arrangement

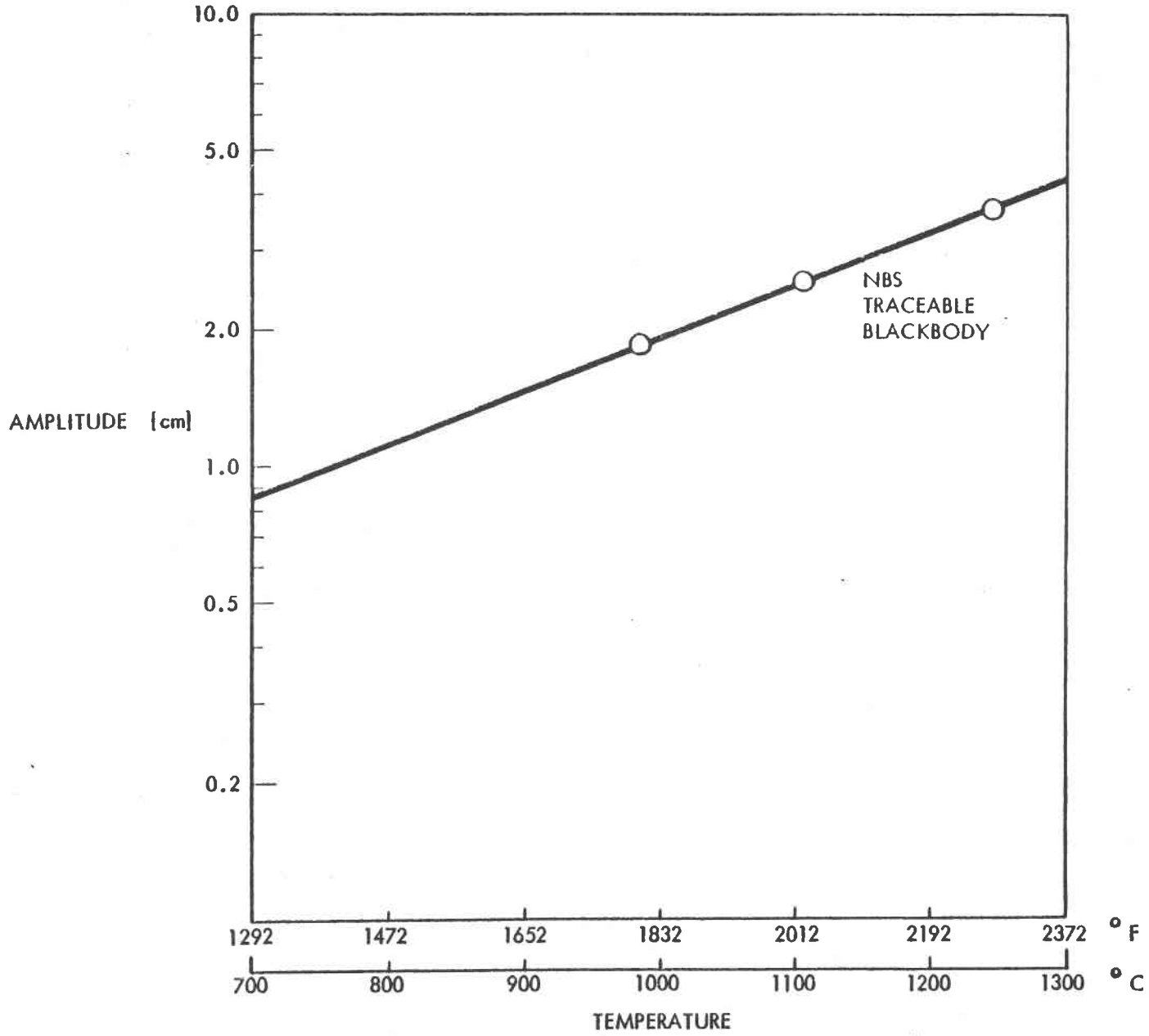

Figure 3-12. Scanner Calibration at 2.8μ

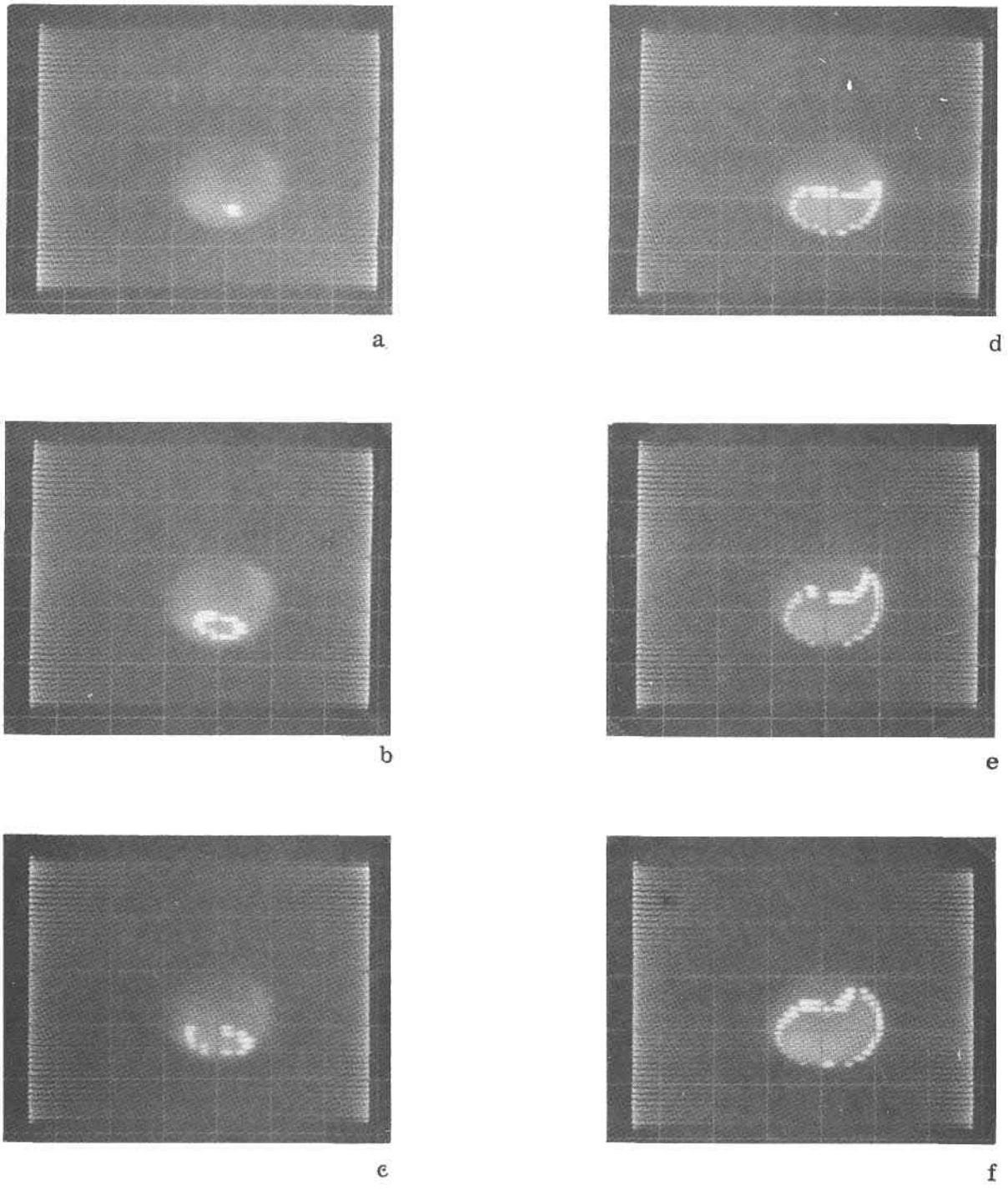

Figure 3-13. Isotherms on the Silicon Carbide - view through receiver window (only the central 5" diameter section is scanned).

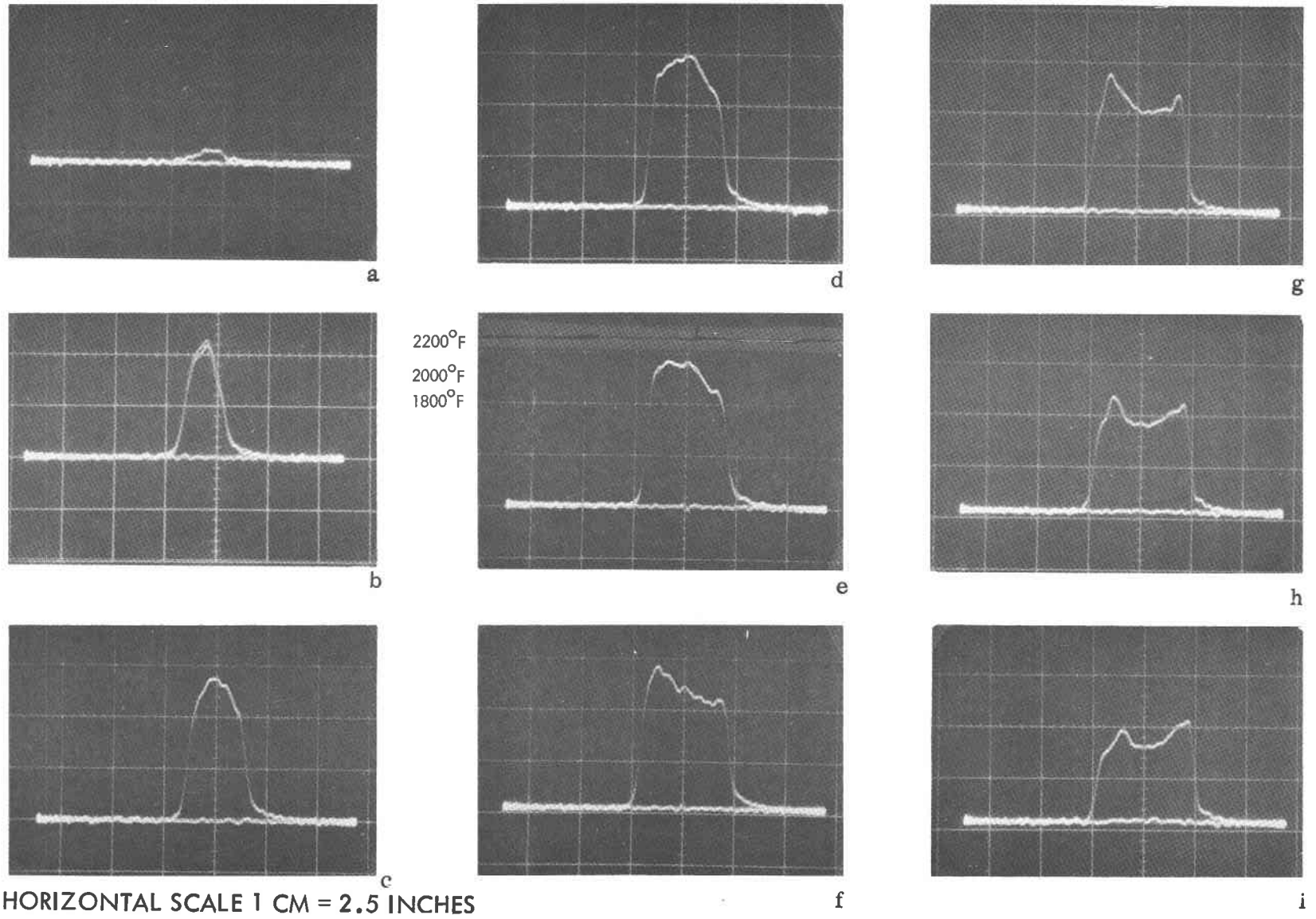

Figure 3-14. Thermal Scans of the Solar Energy Receiver - view of the silicon carbide taken through the window (only the central 5" diameter section is scanned)(sheet 1 of 2)

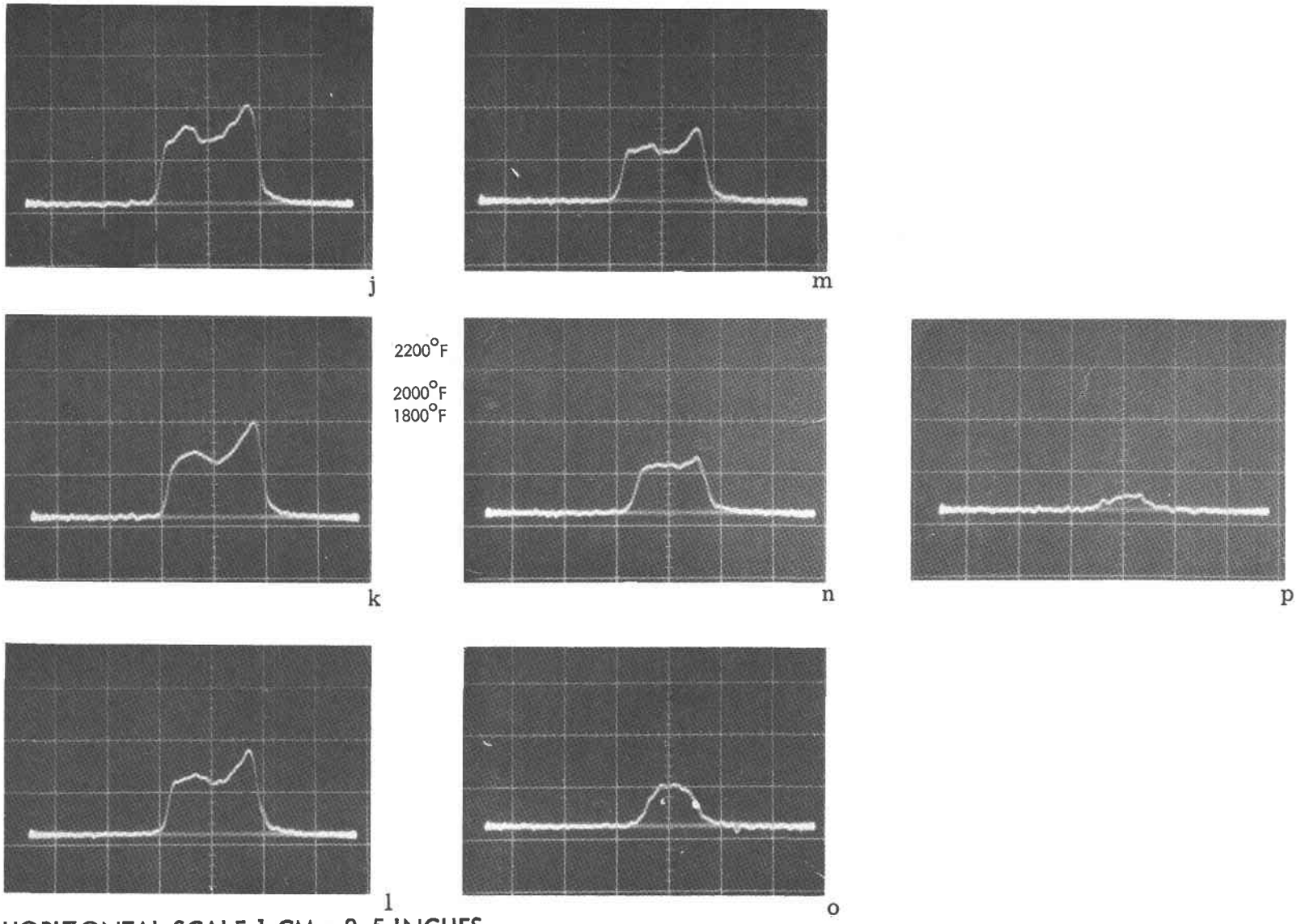

Figure 3-14. Thermal Scans of the Solar Energy Receiver - view of the silicon carbide taken through the window (only the central 5" diameter section is scanned)(sheet 2 of 2)

3.6 EXPERIMENTAL ERRORS IN WHITE SANDS TEST

3.6.1 General

The prime quantity to be measured was conversion efficiency (η). Generally, the efficiency (η) can be described by:

$$\eta = \frac{\dot{m}\, C_p\, \Delta T}{\dot{Q}_{RAD}}$$

where

$\dot{Q}_{rad}$ = integrated radiation flux
$\dot{m}$ = mass flow rate of fluid
C_p = specific heat of fluid
ΔT = temperature change

The precision of the efficiency measurements depends on the precision of the three variable quantities; i.e., $\dot{Q}_{RAD}$, $\dot{m}$, and T, in the range that occurs in the experiment.

Radiation flux ($\dot{Q}_{RAD}$) can be measured either by a carefully calibrated photoelectric device or, much better, by a radiation-absorbing calorimeter. The calorimeter is preferred in that it is less subject to systematic errors if the incident spectrum differs from calibration conditions. However, the instrument must be carefully designed and calibrated to assure that all incident radiation is absorbed or accounted for.

An important factor in overall experimental precision is the relationship of the radiation measurements to actual test conditions. In the White Sands experiments, the calorimeter was scanned over the

actual honeycomb area with the front baffles from the equipment in their operating location. All such scans were made with a single setting of the facility attenuator (at #4); all radiation input values at all attenuator settings are dependent on the consistency and repeatability of this attenuator/shutter system. It is believed that $\pm$5% accuracy in insolation values is appropriate for isolated points, while half this variation is reasonable for ratios of measurements taken in a single run on a single day. This considers both the calibration procedures and the pyrheliometer readings taken during a run to measure the local value of direct insolation.

The mass flow rate ($\dot{m}$) is the least critical factor in determining η. Based on manufacturer's literature (Fischer and Porter ROTAMETER, catalog 10A 1022) and on tests against other instruments at Sanders' environmental laboratory facility, in comparison with other flow measuring equipment (MERIAM Model 50MC2-45, serial #d 14972-R3), a variation of $\pm$3% is judged to be a conservative upper limit, with half this figure attainable with good care.

The temperature difference between the input and output airstream was available from thermocouples (chrome-alumel in this temperature range). The principal thermocouples were radiation shielded, and sample calculations estimated radiation effects on the thermocouples to be 1^{o}F at a maximum, essentially eliminating this source of error.

Possible incomplete mixing of the airstream with associated uncertainty in the wall losses and the long thermal equilibrium time of equipment wall structures leads to a $\pm$5% uncertainty at ΔY. Improvements are not judged possible without redesign of the temperature measuring system and auxiliary experiments to test these accuracies.

3.6.2 Error Propagation Summary

The judgement of experimental errors on individual measurements (due to random uncertainties) is as follows:

$$\% \text{ error in } \eta = \sqrt{5^2 + 1.5^2 + 5^2} = \pm 7.2\%$$

These estimates are generally consistent with the distribution of the White Sands test data (see Figure 3-6 of Section 3.4.1). All the data points together (16 in the above figure) lead to a factor of $\sqrt{16} = 4$ reduction in "overall uncertainty", to the extent that these data points can be plotted on a compatible basis and taken as related to the same basic measurement. With this basis for estimate of overall undertainty, $\pm 2\%$ can be ascribed to the data represented in this figure.

Systematic errors cannot be detected through internal consistency checks within the experiment. Determination of these errors must be based on a critical review of experiment procedures, along with any assumptions involved in data interpretation. All known systematic errors have been eliminated to within the random error figures stated above.

3.7 SUGGESTIONS FOR FUTURE TEST PROGRAMS

3.7.1 Solar Radiation

The input solar radiation is critical and deserves at least two independent measurements, if possible. It is highly desirable that one of these measurements be of the differential type to allow determination of flux distributions. If at all possible, neither measurement should be subject to correction for an attenuator system. Costs might be an obstacle to achievement of this ideal, but the degree of experimental error is reduced by the extent to which these recommendations can be followed.

3.7.2 Temperature Measurement

While a practical alternative to thermocouples in the 1100°C range has yet to be offered for air temperature measurements, the following recommendations will improve experimental precision.

3.7.2.1 Redundancy

Redundancy in a number of (radiation-shielded) thermocouples would, in addition to preventing loss of data in burnout, avoid any uncertainty about complete mixing of all parts of the airstream. An average of thermocouples which independently measure the same parameter will yield data quality improvements. Moreover, observation of temperatures at multiple locations will be the basis of an auxiliary experiment to check the wall loss estimates and the equilibrium time for these losses.

3.7.2.2 Procedure

Operating a run series with constant wall temperatures can reduce the impact of wall losses on the air temperature measurements. Measuring temperatures of the receiver structure is another matter. With the thin walls between tubes, any placement of thermocouples and their leads would perturb the airflow, with substantial alteration of the temperatures to be measured. The most practical temperature measuring method available appears to be the one used in this program, based on use of an infrared scanning device with a solar-blind response filter.

3.8 SUMMARY

By incorporating these recommendations into the design of tests on a scaled-up experiment, improved accuracies can be expected at a modest cost to the test program.

SECTION 4
CONCEPTUAL DESIGN FOR 100 MWe SOLAR POWER PLANT

4.1 INTRODUCTION

4.1.1 Objectives

A part of this contract was a system study to determine the cost of a commercial size power plant using the high temperature Brayton technology. This section describes a baseline conceptual design for a 100 MWe solar power plant based on present day gas turbine technology and the results of experiments and theoretical analysis of the receiver work performed under this contract.

4.1.2 General Requirement

The cost of Sanders' conceptual design was to be compared with concepts under investigation by other DOE contractors. The baseline design was to provide three hours of storage with operation at a power level of 100 MWe. Mirror field design was not considered as a part of this study except for the extent to which tower height and cost were affected. A special requirement for the baseline design was a seismic specification on the tower which would allow it to survive an earthquake that would produce horizontal and vertical ground accelerations on the order of 0.20 to 0.25 g.

4.1.3 Concept Summary

Sanders' baseline design concept for an advanced 100 MWe solar power plant utilizes solar-heated air to drive efficient, low pressure ratio Brayton cycle turbomachinery. Salient features of the proposed system include decoupling the receiver from the turbomachinery, a sensible heat storage system, and the mounting of all power generation

and storage equipment in the tower next to the receiver. Operationally, this design concept offers the user a flexible scheduling of power output to meet varying demands without direct dependence upon real-time insolation.

Energy storage is provided by two thermal storage units, in the form of improved checker stoves, each capable of operating the Brayton machinery for 1-1/2 hours, for a total storage of three hours. The mirror field is sized to provide 10-1/2 hours of nameplate power plant operation on June 21 from 11 hours of solar energy collection. This includes three hours of full power operation directly from storage.

The design concept, as an intermediate power plant operating for 12 hours per day, will derive 57% of the yearly average power from solar energy. The offset mirror field has 9700 heliostats concentrating 2000 suns on a 15.1 meter diameter receiver cavity. The receiver is located with the checker stove storage vessels and all the power generation equipment on a 262 meter high tower. An overall efficiency of 0.30 is projected for the system based on component efficiencies of:

- 0.87 for the receiver
- 0.47 for thermal-to-electric conversion
- 0.73 for mirror field accounting for tracking, blocking cosine reflection, and spillage losses.

(The size of the mirror field is sufficient to generate 103 MWe at an insolation value of 950 W/m^2.)

For an estimated cost of $1240/KWe (1978 dollars) (which includes the cost of a fossil fuel optional burner), the concept will provide capital displacement credit as well as savings in energy costs.

The power plant cycle shown in Figure 4-1 is divided into two basic system functions:

a. An energy collection system which consists of a solar receiver, improved checker stove storage, and a variable speed fan to control the airflow through the receiver and into the top of the storage units; and

b. A power generation system where the Brayton power plant converts heat either from the charged storage unit, or from a fossil fuel burner which supplies the hot air to the Brayton power plant when a solar-charged unit is not available, into electrical power.

4.1.4 Energy Collection

The collection of solar energy is totally independent of the Brayton machinery. The mirror field focuses solar energy into the open cavity of the receiver. Inside the cavity, the solar energy is absorbed on a silicon carbide honeycomb. Air is heated as it passes through the honeycomb; the heat is then transferred to the firebrick checkers in the storage unit which is closely coupled to the receiver. The size of this storage unit relative to the generator nameplate rating determines the length of time the power plant can operate from a single charge.

The heated air, leaving the top of the receiver cavity at temperatures of 1100°C to 1200°C, passes over the top of one storage unit and is cooled as it passes down through the unit on its return to the receiver. When the air passing out the bottom of the unit approaches 1100°C, the storage is fully charged and is switched either to STANDBY or to the power operating loop. Variation of the airflow rate is used to control the receiver outlet air temperature.

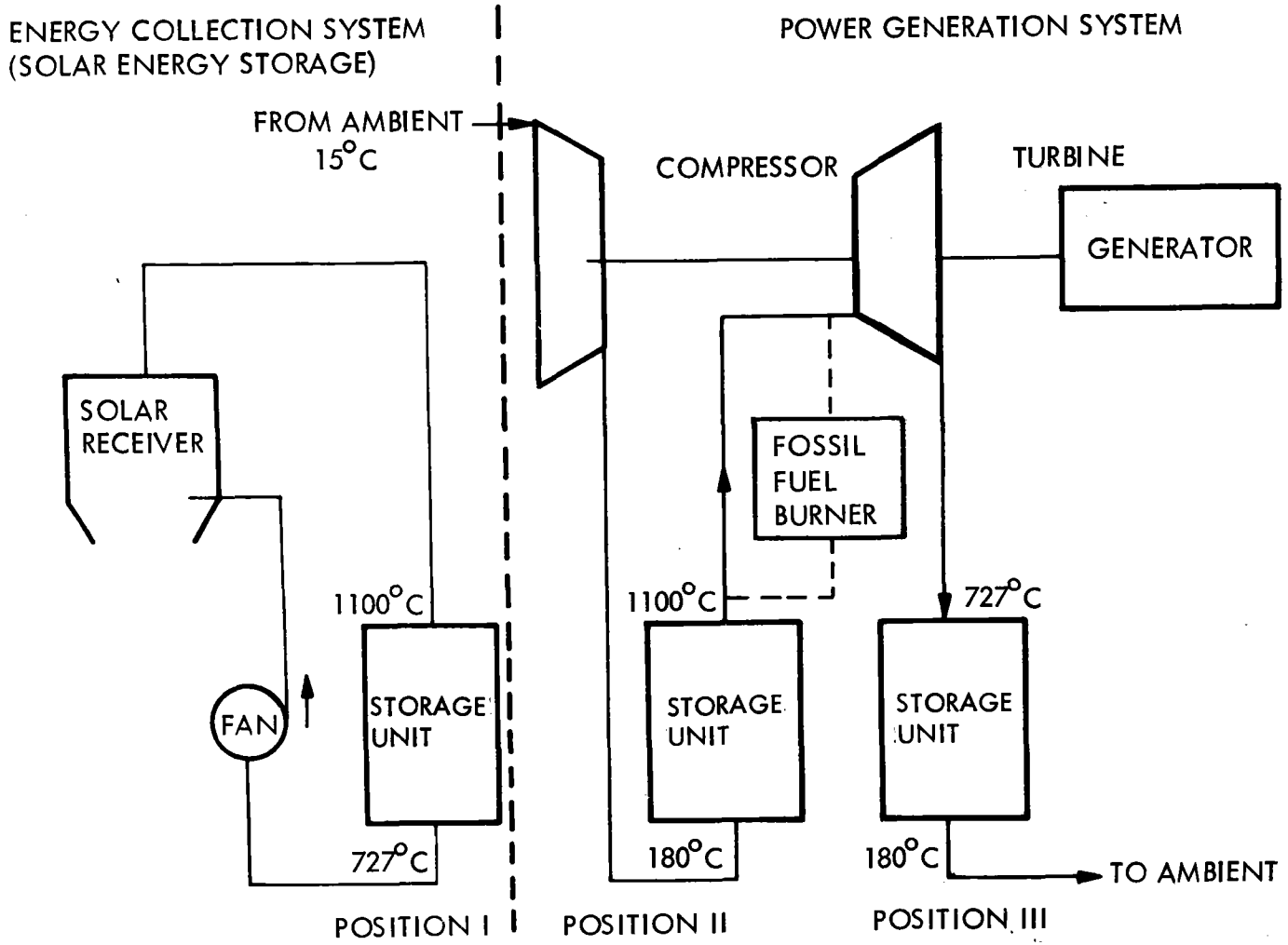

Figure 4-1. Power Plant Cycle

Two more storage units are assigned to the generation system allowing power to be generated simultaneously with the operation of the energy collection system. A fourth unit is in STANDBY, ready for recharging with solar energy should there be a mismatch between power in and power out.

4.1.5 Power Generation

The power cycle starts with ambient air entering the compressor. A 4:1 compression ratio causes the air to be heated to approximately 180°C. The air then passes into the bottom of the hot storage unit (Position II of Figure 4-1) and emerges from the top of the unit at 1100°C. It is then expanded through a two-shaft turbine, generating the power needed to drive the compressor and generator. Air leaves the turbine at approximately 725°C and slightly above ambient pressure to pass into another storage unit (Position III) which has previously been discharged in Position II. The power cycle is complete when the storage unit in Position III reaches 725°C. At this point, the storage unit can be valved into Position I and the cycle repeated.

This power generation concept has the following advantages:

- No water is used
- Brayton machinery efficiencies in excess 50% are feasible
- Low system cost
- Lightweight power generation equipment means fast startup and quick response to varying demand loads
- Safety advantage from low pressure operating system (4 atmos.)
- Adaptable to fossil fuel (oil, gas, or coal)
- Minimal environmental impact even when burning fossil fuel

4.2 CONCEPT ELEMENTS

4.2.1 Brayton Cycle

4.2.1.1 Efficiency versus Pressure Ratio

Since the 1930's, the gas turbine engine used in aircraft propulsion systems has accounted for most of the Brayton cycle engine development efforts. The aircraft application has traditionally emphasized a high thrust, lightweight design rather than high efficiency.

A low pressure ratio recuperated cycle having higher weight-to-power ratio has improved efficiency over the aircraft types and is a prime candidate for ground-based power plants. There are a few models of the recuperated cycle engines available from gas turbine manufacturers, such as the GE Series 7000-R; but there are no production models which optimize efficiency. A comparison of performance characteristics of both types of open cycle gas turbines (Figures 4-2 and 4-3) at a temperature ratio of 5 shows a recuperated cycle as having a peak efficiency of 52% at a pressure ratio of only 4; whereas the nonrecuperated cycle requires a pressure ratio of 32 to reach the same efficiency. This characteristic high efficiency at low pressure ratios of the recuperated cycle gas turbine is the prime reason for its selection in the conceptual design.

In view of the improved efficiency for low pressure ratio recuperated gas turbines, a recuperated design has been selected which operates at a pressure ratio of 4 and a turbine inlet temperature of $1100^{o}C$. A power plant designed to operate under these conditions is available either by a new design or through modification to existing equipment; i.e., reducing compressor and/or turbine stages. Table 4-1 contains desired gas turbine specifications readily obtainable with present technology.

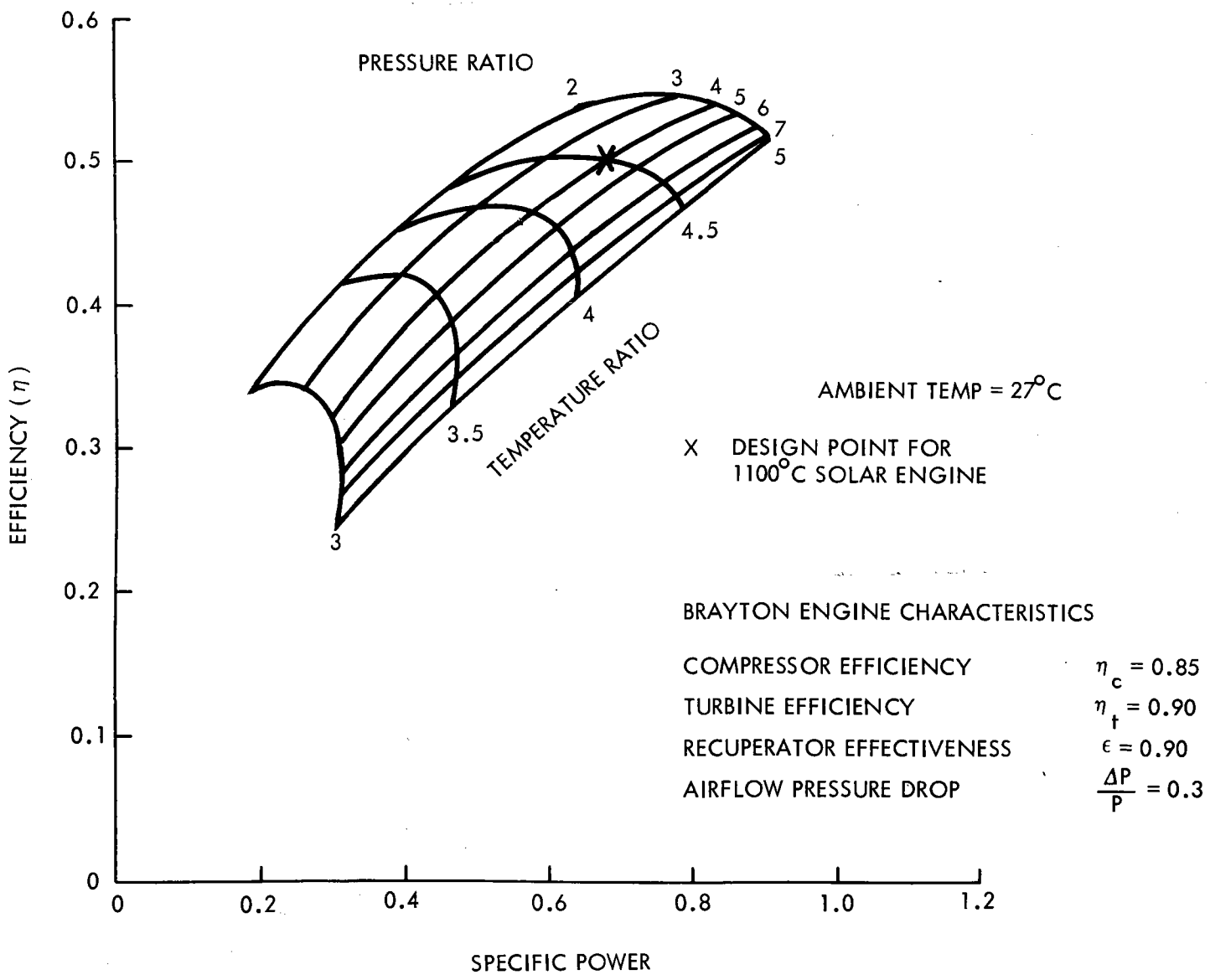

Figure 4-2. Theoretical Performance of Recuperative Gas Turbine Engine

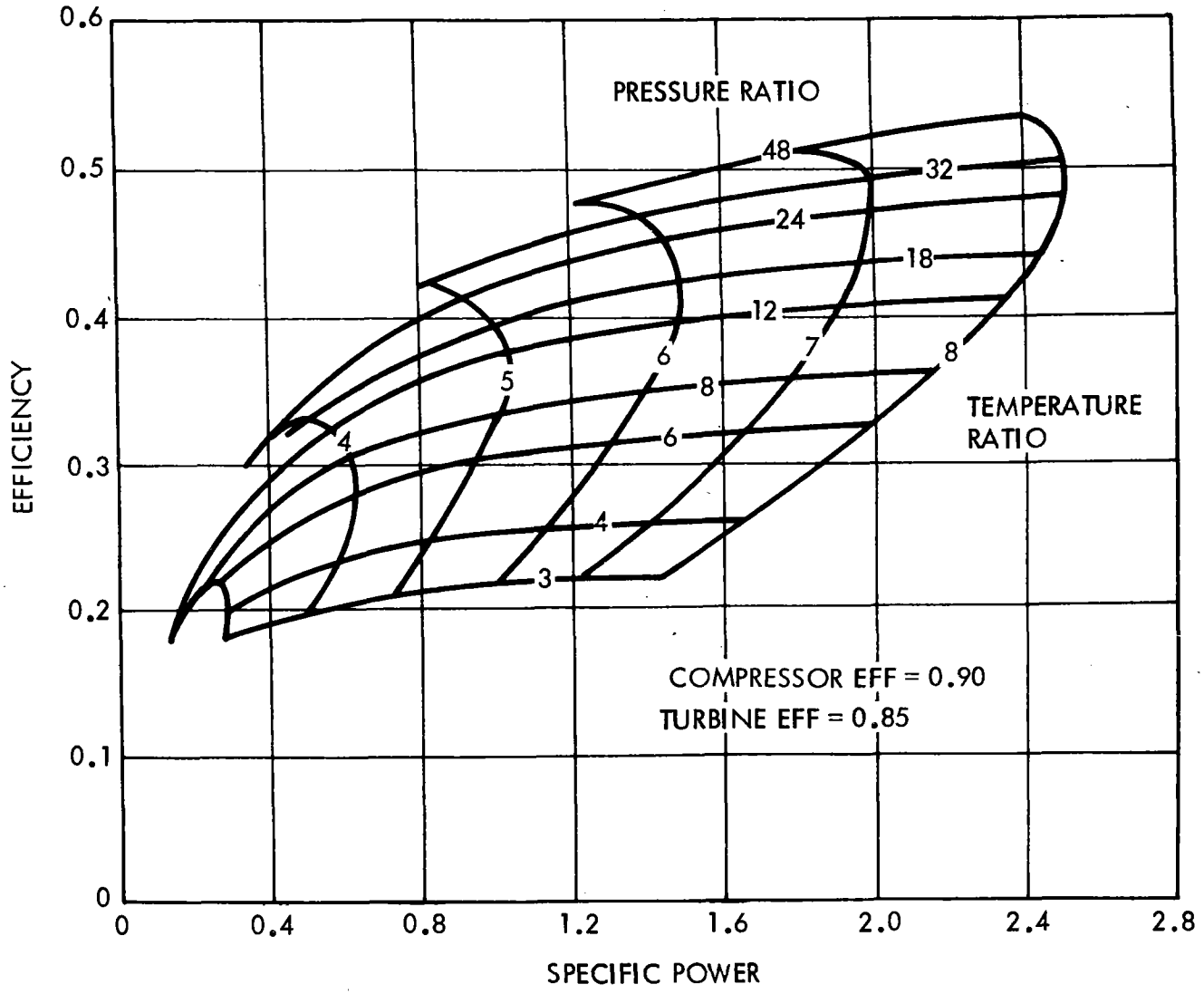

Figure 4-3. Theoretical Performance of Aircraft-Type Gas Turbine Engine

TABLE 4-1. DESIRED GAS TURBINE SPECIFICATIONS

Pressure Ratio	4:1
Temperature Ratio (27°C ambient)	4.7:1
Compressor Efficiency	0.85
Turbine Efficiency	0.90
Sum of Pressure Losses[1] ($\Delta p/p$)	0.02
Recuperator Effectiveness (two recuperators)	0.90
Cycle Efficiency (thermal-to-mechanical)	0.52
Ambient Temperature	27°C

4.2.1.2 Recuperators

Recuperator designs vary widely. Some designs are large metal fabrications which use many small, adjacent tubes to obtain efficient counterflow heat exchange between gases. Other, batch-type units operate in steps: a quantity of hot air heats the unit, is expelled and replaced with cold air which is heated by the hot unit. Rotating wheels are efficient heat exchangers; but where high mass flow is involved, they become so large that valving of fixed exchangers becomes more efficient. Sanders' design concept uses a checker stove similar to that used with a steel blast furnace for the storage of thermal energy. This unit will also serve the recuperator function in the gas turbine cycle.

4.2.1.3 Turbine Configuration

In selecting a gas turbine for use in a power plant, there is a problem in matching the rpm of the generator with that of the compressor, which operates at near-sonic tip speeds for high polytropic

[1] Does not include pressure drop for a combustor.

efficiency. Either a large gear reducer is required to connect the gas turbine to the alternator, or the gas turbine must be large enough in diameter to operate efficiently at 3600 rpm.

The selected design uses: (a) three units modified to be gas generators, and (b) an impulse turbine which drives the generator. Of the several approaches considered, this design is based upon components taken from high pressure and high temperautre ratio engines. The number of high pressure stages in the compressor have been reduced and some of the expansion stages of the turbine removed, leaving only the low pressure ratio compressor and turbine. As a result, the gas turbine performance will experience considerable derating (e.g., 50% reduction in mass flow). The modified unit, therefore, will have greatly improved reliability and will still retain its high turbine inlet temperature capability. The turbine generator is a separate unit of the partial admission impulse type which operates efficiently over a wide range of mass flows.

Westinghouse makes a 100 MWe gas turbine power plant, Model W501, which has been selected for this concept design. It operates at a turbine inlet temperature of 1100^{o}C and a pressure ratio of 12:1. By removing the first nine of the 19 compressor stages and two of the expansion stages, a compression ratio of 4:1 results with a mass flow reduction from 360 kg/sec to 170 kg/sec. Since the specific power is also reduced by 20%, there is an overall power reduction of approximately 35%. Therefore, three gas generator units are needed. A single impulse turbine then drives the Westinghouse generator from the exhaust gases of the three gas generators.

4.2.1.4 Potential Manufacturers

Pratt & Whitney and Rolls Royce each make two-spool, turbojet engines which have separate bearings for high and low pressure stages. Sufficient information has been obtained on the Rolls Royce Olympus

engine to prepare a design concept for a 100 MWe power plant. The normal mass flow is 100 kg/sec and the pressure ratio is 17. The high pressure compressor has seven stages and the high pressure turbine has two stages. The entire engine sells for $800,000, ready for installation in an aircraft.

Five stages of the high-pressure compressor provide a pressure ratio of 4. At full speed, each unit would produce the equivalent of 6.7 MWe: therefore, eight units would be ducted to one 50 MWe power turbine and generator such as a Curtiss-Wright MOD POD 50 modified to operate at a lower pressure ratio. Two such combinations would be needed to produce 100 MWe.

The price of the high-pressure spool with only combustor and associated controls is $520K, the cost of the gas generator is estimated to be $83/KWe. To this, the quoted price of a Curtiss-Wright MOD POD 50 at $85/KWe must be added for a total power plant cost of $168/KWe. The Pratt & Whitney FT9 is a two-spool engine of a similar mass flow. Its industrial version (derated aircraft) is designed for a turbine inlet temperature of 1200^{o}C. Another approach to the Brayton machinery is a modification of the General Electric 7XXXR series described in Section 4.3.5.

4.2.1.5 Operational Features

The separation of the gas generator function from the power turbine function also separates the high temperature components from the main power generation unit. In Sanders' concept where there are eight, high speed, high temperature gas generators for each power turbine, a failure of one of the high temperature blades will cause only a 12% loss in peak power rather than a total shutdown. The high reliability of the power turbine operating at lower temperatures and speeds, combined with the multiple gas generators, will result in improved plant availability.

On startup, one of the gas generators is used to pressurize the checker stove. The gas generator is started either by depressurizing a spent stove or by using a standby combustor. Once pressurized, power is available to start more gas generator units. Consequently, the start-up procedure will take only several minutes. By switching gas generators in and out, a fast response in following peak load demands is possible. Furthermore, the fossil fuel combustor is available for topping as well as for capital displacement credit.

4.2.2 Block Diagram

4.2.2.1 Receiver Decoupling and Storage

The power plant cycle for solar energy collection has a receiver which is totally independent of the Brayton machinery (Figure 4-1). Operating at ambient pressure with an open cavity, the receiver collects solar radiation on a silicon carbide (SiC) honeycomb configuration. The air is heated as it passes through the honeycomb; the heat is then transfered to the firebrick checkers in the storage unit. This transfer is similar to checker stove operation at a steel plant. The size and number of storage units determines the length of time the power plant can operate from storage.

Air leaves the top of the receiver cavity at 1100^{o}C, passes over to the top of the storage unit, and is cooled as it passes down through the storage on its return to the receiver. When the air passing out the bottom of the storage unit approaches 1100^{o}C, the storage unit is full and can be switched to either operate the Brayton machinery or be held in reserve. The airflow is controlled to regulate the receiver outlet air temperature. Four storage units are used so that the power cycle can function simultaneously with the charging cycle.

4.2.2.2 Power Generation

The power cycle starts with ambient air entering the compressor. The air leaving the compressor is at 4.1×10^5 N/cm^2 (4:1 compression ratio) and 150°C. The air is then heated as it rises through the storage unit in Position II Figure 4-1 to a temperature of 1100°C. As it passes through the turbine, pressure and temperature are reduced to 1.02×10^5 N/cm^2 and 150°C before the air is exhausted to the atmosphere. Pressure losses through the storage units are on the order of 1% because fluid velocities are low.

An alternative energy source, when solar energy is lacking, is the standard gas turbine combustor used in series with the stove in Position II, Figure 4-1. In this way, power plant operation could become totally independent of hourly, daily and seasonal variations in insolation.

4.2.3 Sizing and Costing-Tracking Efficiency

A total concept must be developed before costs can be compared with other systems. This concept includes extracting information on mirror fields from the work of others and assembling cost elements for all parts of the system concept. The mirror tracking efficiency, an important element of the mirror system design, was supplied by Sandia Laboratories on June 10, 1976. This is shown in Figure 4-4, where the tracking efficiency includes cosine, shadowing and blocking losses only. Both a north field and an offset field were considered; the offset field was selected because

of the superior tracking efficiency available during the summer months. It also allowed a lower tower and a smaller mirror field for the same mirror area. No further analysis was performed except to limit the daily solar collection to period when the tracking efficiency was greater than 0.50.

4.3 DESIGN POINT SELECTION

4.3.1 Mirror Field Selection

With the collection system decoupled from the generation system, the power generated does not depend on the insolation. A mirror field was selected which will provide at least 50% of the average yearly energy demands of an intermediate type of power plant located at Barstow, California and operating 12 hours each day. The storage volume was sufficient to collect all the mirror-reflected energy on June 21 with an insolation of 950 W/m^2. Table 4-2 describes the efficiency factors which result in an overall solar-to-electric efficiency of 0.30. It was assumed that the daily insolation averaged over one year for the Barstow, California location is 6.5 $kW\text{-}hr/m^2\text{-}day$.

$$\text{Mirror area for 100 MWe} = \frac{10^8}{950 \times 0.30} = 350{,}877 m^2$$

$$\text{Number of mirrors of } 37.2 m^2 = 9432$$

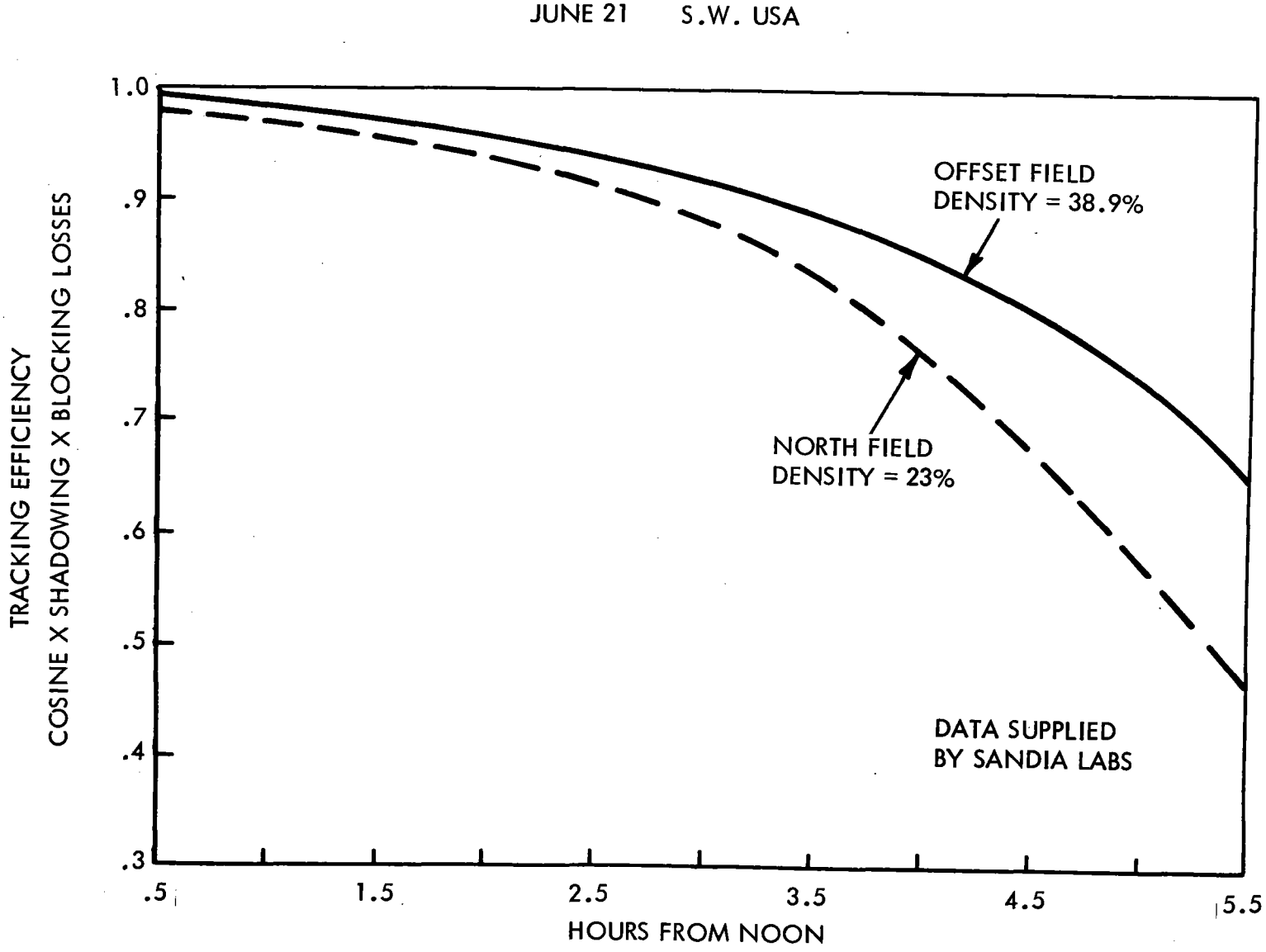

Figure 4-4. Tracking Efficiency

TABLE 4-2. TABLE OF EFFICIENCIES FOR JUNE 21, 1978

Solar Power In: 331 MWe

		η	MW	
Mirror Reflectivity	=	0.91	301	
Integrated cos, Tracking Blocking[1]	=	0.89	268	Mirror Field: η = 0.731
Power Accounting for Spillage	-	0.97	260	
Power Accounting for Reflection Losses	=	0.93	242	
Power Accounting for Radiative Losses	=	0.91	220	
Power Accounting for Convective Losses	=	0.98	216	Receiver: η = 0.874
Power Accounting for Conductive Losses	=	0.98	211	
Storage for Pumping & Thermal	=	0.98	206	
Thermal-to-Mechanical Conversion[2]	=	0.50	105	Conversion: η = 0.475
Mechanical-to-Electrical Conversion	=	0.97	100	
Daily Overall Efficiency	=	0.30	100	MWe

(1) Integrated for 11 hours of collection on June 21 in southwestern USA. Data supplied by Sandia Labs in June 1976. Offset mirror field with packing density of 38.9%.

(2) See design point on Figure 4-2.

In one year, this will generate

$$365 \times 6.5 \times 350{,}877 \times 0.3 = 249{,}737 \text{ MWe-hr}$$

Solar contribution is

$$\frac{249{,}737}{365 \times 100 \times 24 \times 0.5} = 0.57$$

For Sanders' concept, the solar multiple (SM), which is a measure of the average to the peak tracking efficiency, varies with the number of hours of operation desired per day. In the example, 10.5 hours of operation and 11 hours of solar energy collection on June 21 has an associated SM = 1.1.

4.3.2 Storage Size

The size of storage has been arbitrarily selected as that size required to hold sufficient heat to generate 150 MW-hr of electricity. With the fourth stove in STANDBY, there is the potential for 3 hours storage. As shown in Table 4-2, 100 MWe requires 211 MWt x 1.5 hours = 316.5 MWt-hr. Heat will be stored in ceramic firebricks such as Mullite, having a density of 160 lb/ft^3 and a shape factor to give 50% open area. To estimate the weights in pounds:

$$W = \frac{Q}{C_p \Delta T}$$

where

$$Q = 316.5 \times 10^3 \times 3412$$
$$= 1.079898 \times 10^9 \text{ Btu}$$

$$C_p = 0.23 \text{ Btu/lb} - {}^{o}\text{F}$$

$$\Delta T = 800^{o}\text{F} \ (2000^{o}\text{F} - 1200^{o}\text{F})$$

Assumes 100% utilization (No oversizing allowance for thermocline thickness)

$$W = 5.87 \times 10^6 \text{ lb}$$

$$\text{tank volume} = \frac{5.87 \times 10^6}{160 \times 0.5} = 73{,}363 \text{ ft}^3 \text{ (45 ft D x 45 ft H)}$$

(0.5 = ceramic fraction)

weight of tank, insulation and hot valves = 6×10^5 lb

total weight of each tank = 6.47×10^6 lb

4 tanks' weight = 25.88×10^6 lb (22×10^6 kg)

Taking a day in June as an example of the stove operation (Table 4-3) sunrise is at 4:30 AM. At 6:00 AM, the tracking efficiency has reached 0.5. After allowing 30 minutes for adjustments, collection of solar energy begins to charge the stove in Position I. When stove I is fully charged, it is switched into Position II, stove III is switched to Position I, and stove II is switched to Position III. After 8:30 AM, energy is collected at a greater rate than energy delivered; this condition will continue until 3:30 PM. During the day, whenever the stove in Position II is empty, a fully charged stove is ready waiting to be connected. Energy collection stops at 5:30 PM, but nameplate power continues from the solar energy in storage until 7:00 PM. By 7:00 PM, the fossil fuel burner will be on and ready to be switched on-line if needed. Sunset occurs at 7:30 PM. Solar energy has supplied 10-1/2 hours of the 12 hours of intermediate plant operation at this time of year.

4.3.3 Mirror Field Geometry

The mirror field geometry was calculated from an existing computer program which determined the cosine of the angle between each heliostat and the sun at noon for June 21. The inputs of this program are: (a) the azimuth and elevation angles of each mirror and (b) the latitude, longitude, and declination of the sun on June 21 for Barstow, California. The solar receiver has its central axis tilted 14 degrees towards the north and a terminal concentrator with a rim angle of 62 degrees.

TABLE 4-3. ENERGY COLLECTION SCHEDULE FOR JUNE 21

HOURS OF OPERATION	TIME	ENERGY COLLECTED (MWe-hr)	ENERGY SUPPLIED (MWe-hr)	ENERGY IN STORAGE (MWe-hr)
Sunrise	4:30 AM	-	-	-
0 (on)	6:30 AM	0	0	0
1	7:30 AM	36	0	36
2	8:30 AM	123	0	123*
3	9:30 AM	222	50	72
4	10:30 AM	327	150	177
5	11:30 AM	434	250	184
6	12:30 PM	543	350	193
7	1:30 PM	652	450	202
8	2:30 PM	759	550	209
9	3:30 PM	864	650	214
10	4:30 PM	963	750	213
11 (off)	5:30 PM	1050	850	200
	6:30 PM	-	950	100
	7:00 PM	-	1050	-
Sunset	7:30 PM	-	-	-

*Switch at 150 MWe-hr to Power Generator

The mirror field design selected, shown in Figure 4-5, is elliptical with the tower placed south of center. The outward lines, like spokes of a wheel, give the bearing or azimuth angle. The concentric circles about the tower represent the elevation angles of the heliostat to receiver line-of-sight. The 60 degree pie segment located directly behind the tower cannot be viewed by the receiver because of tower blockage, and therefore contains no mirrors. This mirror area, with a packing density of 38.9%, results in a mirror field area of $9.25 \times 10^5 m^2$ with 9700 heliostats, each having an area of $37.2 m^2$ (note that the minimum number of heliostats of 9432 was increased to 9700 to provide for outages). For the proposed design concept, the cavity is at a height of 233 meters and the maximum height of the tower is 262 meters.

4.3.4 Receiver/Tower Design

4.3.4.1 General Arrangement

The tower positions the receiver over the mirror field with a clear field-of-view except for the 60 degree pie segment to the south of the tower (Figures 4-5 and 4-6). The active system components are located in the enclosure at the top of the tower. The enclosure represents a two-story building 70 meters in the north-south direction, and 37 meters in the east-west direction. The open cavity receiver, which is 15.1 meters in diameter, is located on the north side of the enclosure, as shown in Figure 4-7. The storage stoves are located at the same level and are closely coupled to the receiver.

Receiver and cavity design is based on heat transfer analysis and experimental results obtained from a 10 kWt unit tested in the solar test facilities at White Sands Missile Range. The honeycomb solar collector, located within the cavity, is made from silicon carbide bricks

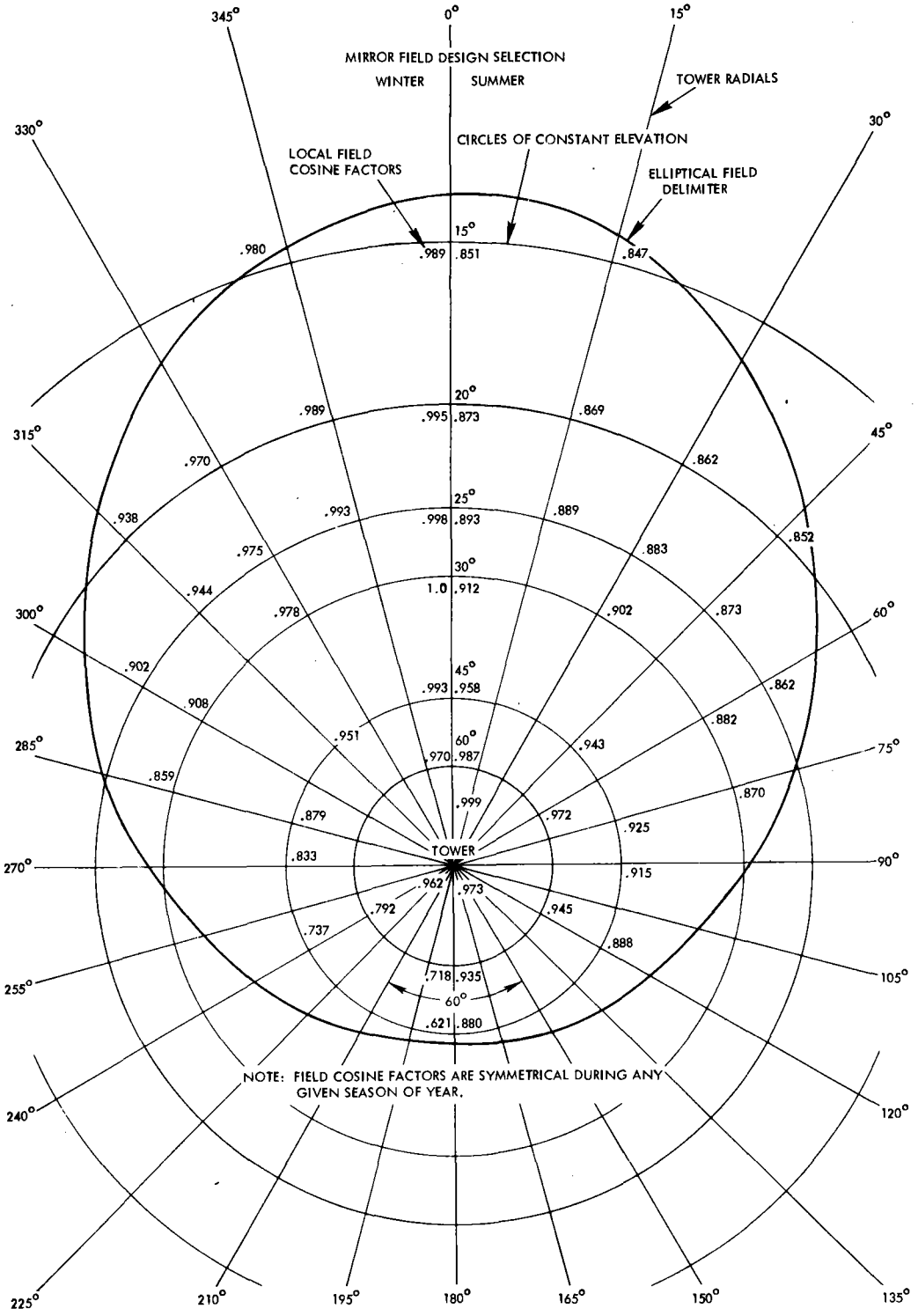

Figure 4-5. Mirror Field Design

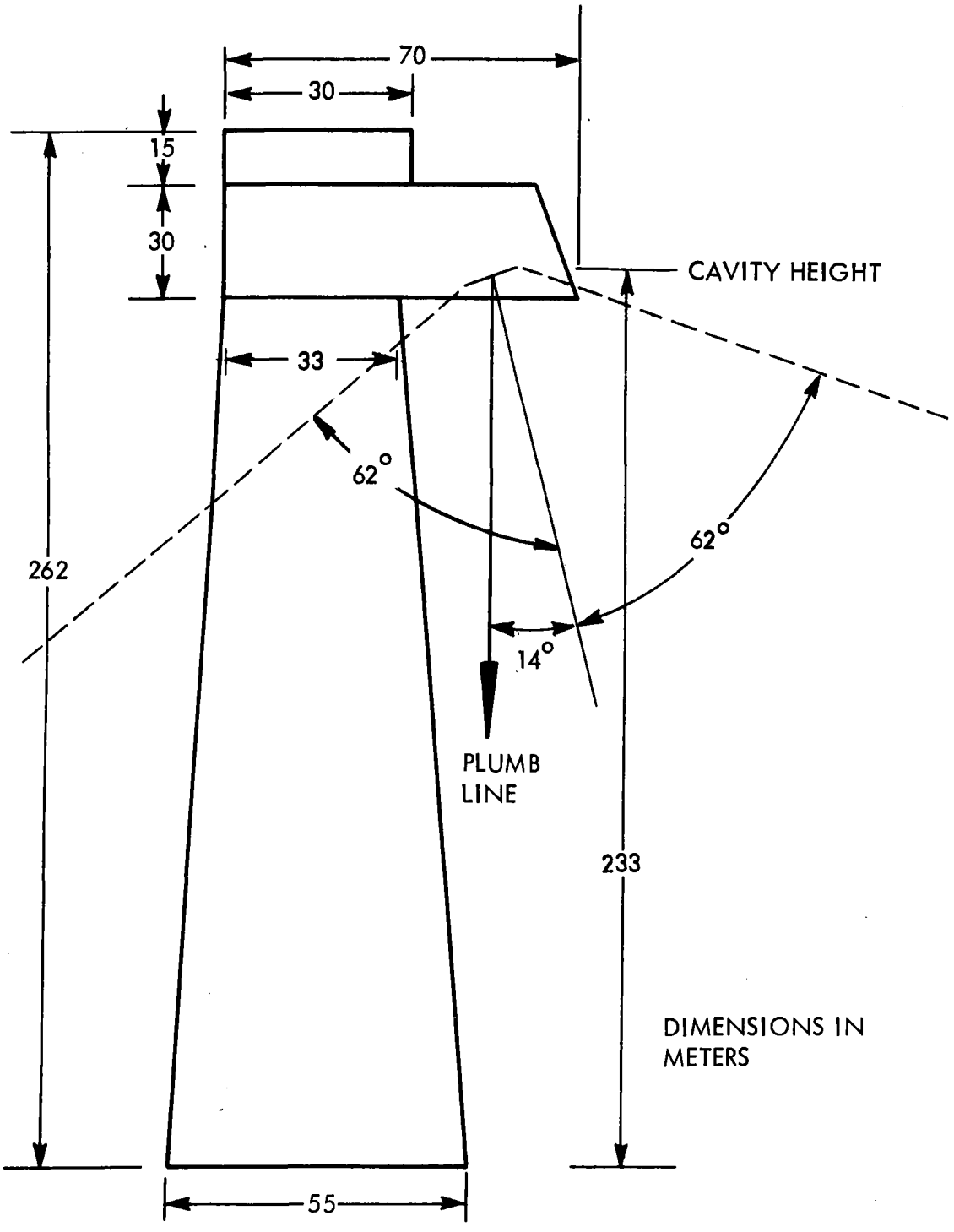

Figure 4-6. Tower Design

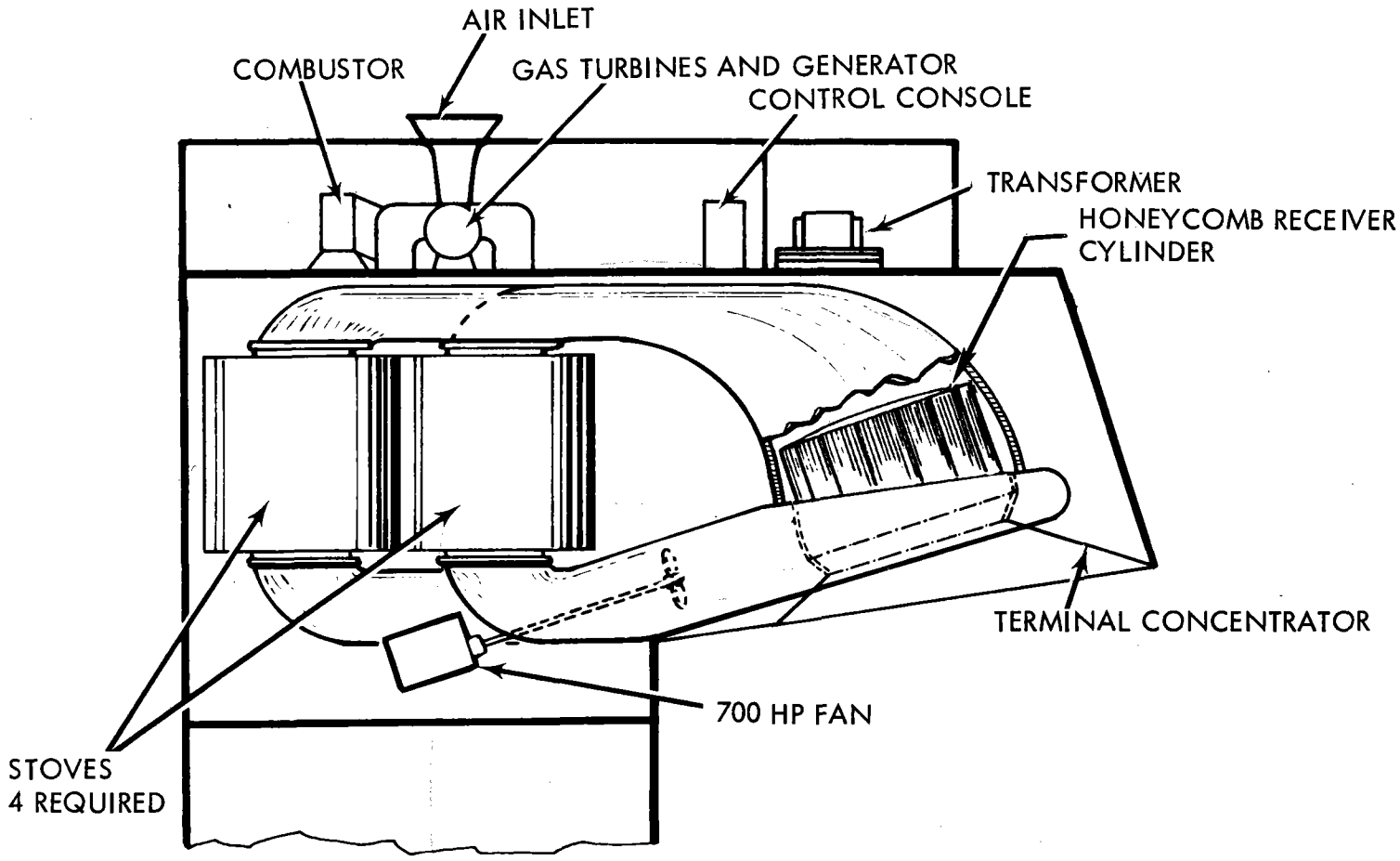

Figure 4-7. Storage - Receiver Ducting

assembled into a cylinder. The manifold surrounding the base of the receiver supplies a controlled amount of air into the cavity. As it passes through the honeycomb, the air is heated and ducted to the top of the checker stove. A variable speed fan at the bottom of the checker stove controls the airflow from 270-545 kg/sec such that the air temperature entering the top of the checker stove is maintained at $1150^{o}C \pm 55^{o}C$. A wind shield, extending beyond the cavity entrance, protects the cavity against wind convection losses, and also functions as a terminal concentrator to deflect part of the reflected beam from the farthest mirrors into the cavity, thus minimizing radiation losses.

The gas turbine burners and turbines are located on the floor above and directly over the stoves. This location has the advantage of having the lowest inlet air temperature for the most efficient gas turbine cycle, plus short connections to minimize pumping and convection losses. Also, the inlet air is free of sand and dirt which would require filtering if the inlets were located on the ground.

The two floors represent an enclosure height of 45 meters: 15 meters for the rotating machinery and 30 meters for the stoves and receiver. The heavy equipment such as stoves, electric motors and ducts are positioned directly above the cylindrical tower support. The lightweight receiver is cantilevered to the north.

Air for the Brayton machinery enters the three gas generators at ambient conditions, is compressed to 4 atmospheres, and directed down to the bottom of the fully charged stove. As the air rises through the stove, it absorbs heat from the firebrick and returns to turbine I, upstairs, which drives the compressor. The hot gases then leave turbine I, at somewhat reduced pressure and temperature, passing into the impulse turbine II which is directly coupled to the electric generator. The air leaves turbine II at near-ambient pressure and

727°C to enter the top of the third stove. The third stove has previously been cooled to 180°C in Position No. II (Figure 4-1). It now recovers waste heat from the turbine exhaust and is heated to 727°C. The exhaust of this stove is expelled to the atmosphere at 180°C. A fourth stove is in STANDBY position.

As shown in Figure 4-8, a Westinghouse 100 MW generator is coupled to a three-inlet impulse turbine. A transformer is also located on the roof outside and adjacent to the generator and is surrounded by a firewall dike for containing the transformer oil.

Sanders' conceptual design also incorporates a wind screen. The simplest wind screen design is passive and consists of appropriate flow deflectors built into the terminal concentrator, as shown in Figure 4-9. Crosswinds, which are essentially parallel to the ground, will be deflected down to pass below and not into the cavity. Small eddy currents may still remain at or near the cavity entrance; their contribution to convective loss will be minimal.

4.3.4.2 Tower Design

General

The convenience and efficiency of closely coupling the receiver to the checker stove storage and Brayton cycle machinery in the tower means the tower must support more weight than do competitive designs. To give some reference to the required size of the solar tower, it is useful to compare it to the CN Tower in Toronto, shown in Figure 4-10. This tower, which was ready for occupancy in 1976, is 549 meters tall. The lower 350 meters were constructed of slipformed concrete

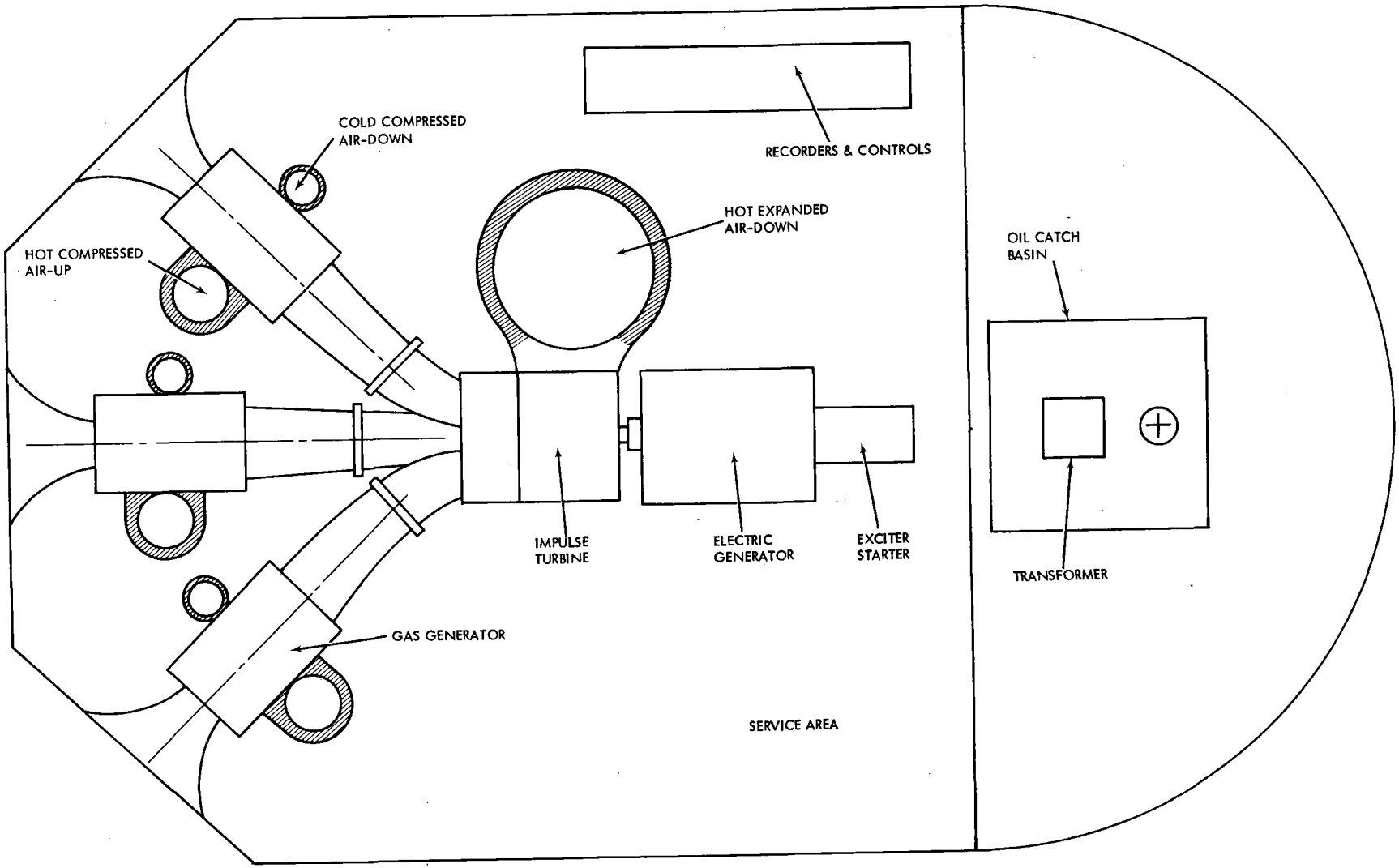

Figure 4-8. Top Floor Layout

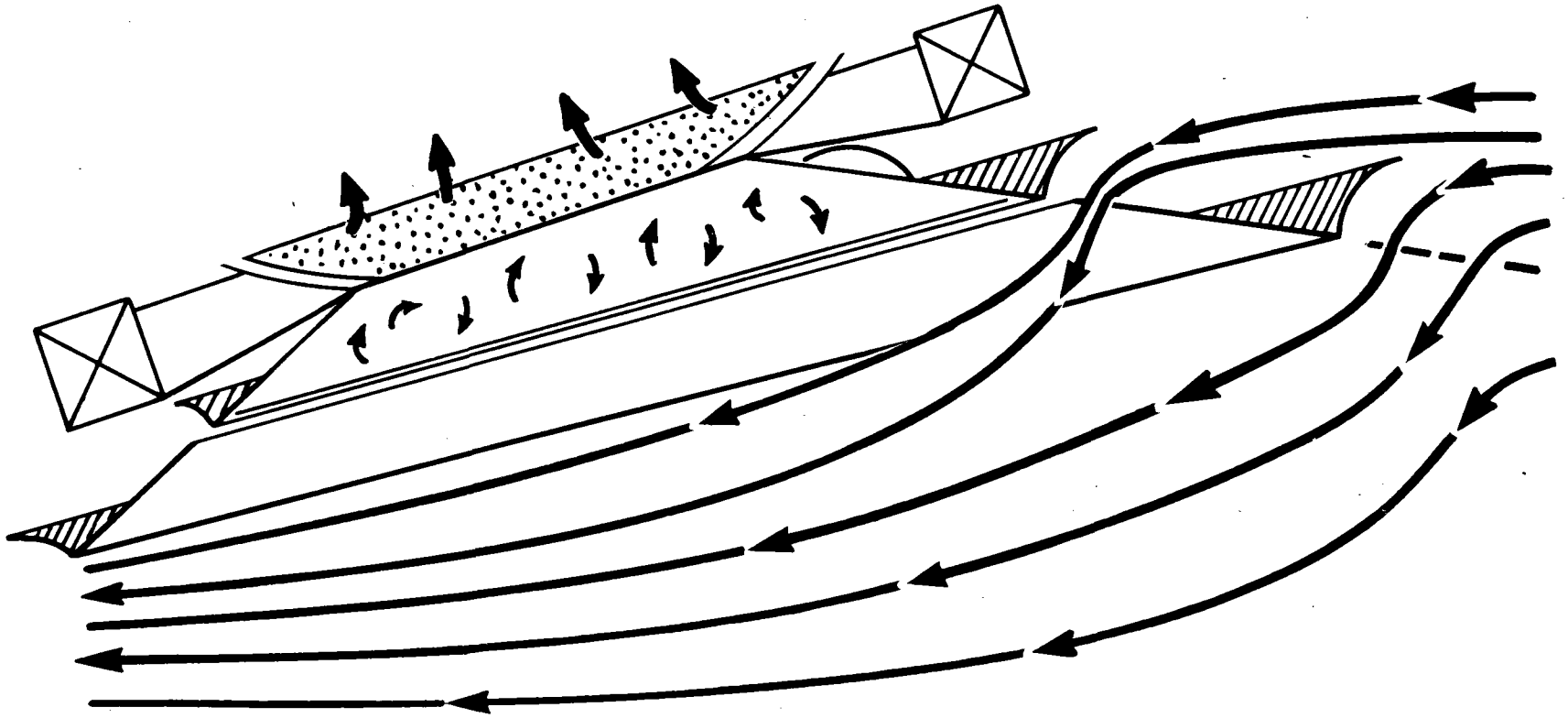

Figure 4-9. Passive Control of Open Cavity Wind Losses

CN TOWER TORONTO

- CONSTRUCTION: STEEL REINFORCED SLIP FORMED CONCRETE
- TOTAL TOWER WEIGHT = 2.6×10^8 LBS
- DESIGN CRITERIA: MAXIMUM WIND GUSTS

100 MW SOLAR POWER TOWER

- CONSTRUCTION: STEEL REINFORCED SLIP FORMED CONCRETE
- TOTAL TOWER WEIGHT = 140×10^6 LBS
- DESIGN CRITERIA: SURVIVAL OF ZONE 3 EARTHQUAKE EXCITATION ($\simeq$.25 g's RESPONSE IN HORIZONTAL)

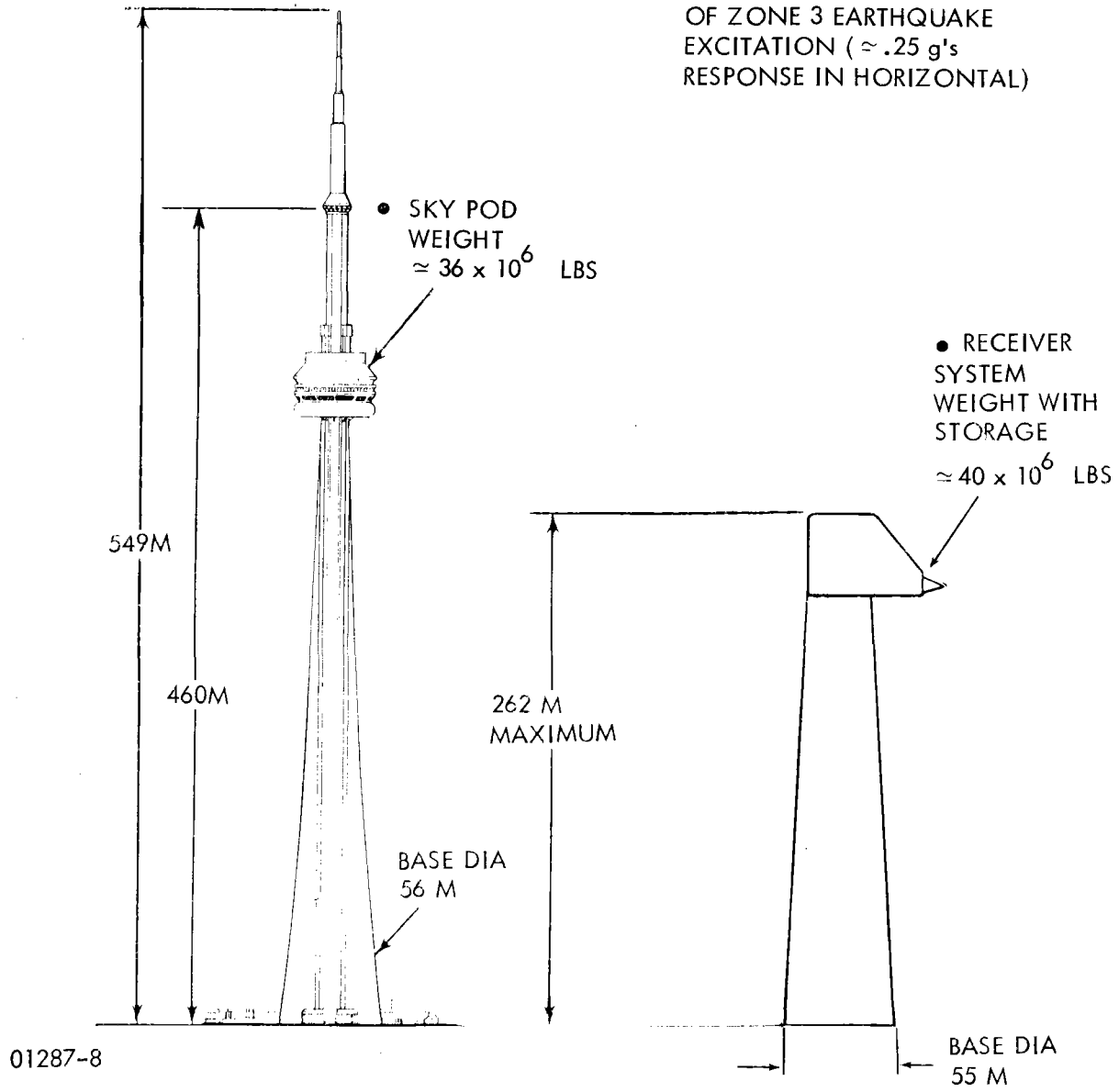

Figure 4-10. Tower Concept

weighing 118 x 10^6 kg, which includes 16 x 10^6 kg for the sky pod. The sky pod weight exceeds the total weight of four storage stoves, the rotating machinery, the receiver and the enclosure. However, in the proposed design concept, the slip-formed structure will be 214 meters high which is considerably shorter than the CN Tower with the same base diameter. The total weight is approximately 64 x 10^6 kg, with the powerhouse and its contents accounting for 18 x 10^6 kg. Of the 18 x 10^6 kg, 12 x 10^6 kg is assigned to the storage stoves; 3.5 x 10^6 kg to the receiver, turbines, generator and valving, etc.; and 2.5 x 10^6 kg to the enclosure.

Seismic Considerations

Since one of the candidate locations for a solar tower is in California near the location of major geological faults, the basic structural integrity of the tower and its equipment must not be destroyed by a Zone 3 earthquake, and the equipment should be operable after realignment. A preliminary analysis of the effects of Zone 3 earthquake excitation on a typical solar tower structure was performed with the principal objectives of: (a) assessing the resulting dynamic loads imposed upon the system components located on top of the tower; and (b) determining structural requirements for a 335-meter high, slip-formed concrete tower of the type conceived in the NSF Report.(ref 4)

The acceleration response spectrum for the NSF tower was based on the average ground excitation of the four largest California earthquakes for which recorded ground motion exists. These response spectra are the results of comprehensive analog computer calculations of structural response to known earthquake ground excitations (which exhibit the characteristics of random fluctuations) for a range of structural parameters. The results are conveniently depicted in reference 5 as structure response acceleration for a single degree-of-freedom system as a function of the structure's undamped natural period and the fraction of critical damping inherent in the design. The assumption

is made that the structure's foundation moves with essentially the same motion as that of the ground; in other words, there is negligible interplay between the ground and the building. Data taken during both major and minor earthquakes has shown this to be true for buildings on solid ground. The assumption is made that only the horizontal component of the ground motion during an earthquake is of concern. The literature states that the magnitude of the vertical components is generally much less than the horizontal component.

The resonant frequency of an NSF-type, 335 meter high, conical concrete tower with a 40 to 90 meter diameter base and 1.5 meter thick linearly tapered walls will be in the 0.6 to 1.0 Hz range. The average response acceleration levels to equipment mounted in the top of the tower resulting from the ground motion of the strongest recorded California earthquake, centered at a moderate distance from the tower (70 km), would be in the range of 0.25 to 0.32 g's. Based on these response accelerations, an equipment specification for the tower-mounted components of 0.35 g's in the 0 to 2 Hz range and 0.15 g's from 2 to 5 Hz should be sufficient. Magnification from ground to tower is not expected to be significant in a building with such a low natural frequency.

This response level is based on a damping coefficient equal to only 5% of the critical damping which is a fairly conservative value. For example, concrete structures typically have damping equal to 8% of critical and normal buildings as high as 15%. (The addition of small amounts of damping significantly reduces the maximum response.) The tower resonant frequency will be independent of wall thickness and will vary linearly with base diameter. The acceleration response of 0.25 and 0.32 g's corresponds to the 40 to 60 meter base diameters. Since the range of resonant frequencies is smaller than the recorded excitation frequencies of major earthquakes, a tower design with an undamped natural resonance lower than the 0.6 to 1.0 Hz range would result in a lower response acceleration to the tower-mounted equipment.

It should be pointed out that the above-described NSF conical concrete tower is a fairly stiff structure, considering it is 335 meters in height. For comparison, the measured resonant frequency of an 87 meter high, 23 meter x 23 meter building was only 0.5 Hz. It is anticipated that a 335 meter high, structural steel frame-type tower with a suitable load-carrying capability could be designed with a lower undamped natural resonance; and in turn, could lower the acceleration response levels to the equipment. An alternate design concept, if such response levels become a practical necessity, might be to suspend the powerhouse from the tower with a damped hanger system.

Structures which are designed to sustain a major earthquake without exceeding yield strength (like the NSF tower) are not common. In other words, the lateral forces to which buildings are subjected during a major earthquake are much larger than the design forces specified by the building codes in seismic regions. For example, the building code for the City of Los Angeles specifies that the NSF 335 meter tower does not exceed yield stresses when subjected to lateral forces equivalent to a 0.04g input excitation. This results in buildings which are overstressed and sustain considerable damage (e.g., cracked interior partitions or permanent deformation of structural members) during major earthquakes. These buildings have considerable capacity for energy dissipation and do not undergo serious failure; i.e., collapse. The capacity for energy absorption via various forms of plastic deformation characteristically provides an adequate margin of safety against collapse. It is fairly obvious that the NSF-type conical concrete tower does not have a great amount of plastic deformation energy absorption capability due to its rather simple design. With the exception of the strain energy dissipated via plastic elongation of the reinforcing rods, the yield is indicative of collapse of the structure. In other words, this relatively stiff tower represents somewhat of a brute force design approach to seismic survivability.

The maximum outer fiber tensile stresses resulting from the inertial response to a major earthquake excitation of a 40 meter base x 335 meter high conical tower with 1.5 meter thick tapered walls, assuming the inertial load is equivalent to a static load acting through the tower cg, would be about 7.6×10^6 pascals (1100 psi). Since the tensile yield of unreinforced concrete is only 1.4×10^6 to 2.1×10^6 pascals (200 to 300 psi) and the compressive stress due to gravity is only on the order of 1.7×10^6 pascals (250 psi), a substantial amount of continuous steel reinforcing rods will be required near the outer diameter. It is design practice with concrete structures to neglect the tensile strength of the concrete completely and assume the reinforcing steel takes up the entire tensile load. A preliminary calculation indicates that 2.5 cm diameter reinforcement on 10 cm centers (or the equivalent) will be required.

In summary, the proposed tower is not as tall as the NSF tower; and because of its stiffness and low natural frequency, it should sustain a severe Zone 3 earthquake without damage to the structure. However, realignment may be required. Any serious structural disruption would obviously require more than simple realignment.

4.3.4.3 Receiver

The solar receiver is made from silicon carbide fabricated into a special honeycomb configuration which optimizes the heat transfer to air. During August 1976, Sanders conducted tests of this honeycomb in a 10 KWt solar receiver simulator (Figure 4-11) at the White Sands solar test facility. These tests demonstrated the suitability of the honeycomb material as a solar receiver for air temperatures exceeding $980^{o}C$, and also that computer simulations could accurately predict the radiant, conductive and convective heat transfer between the solar input and the outlet air.

Further computer simulations have been performed using a two tube, multi-node analysis to evaluate: (a) effects of inhomogeneity

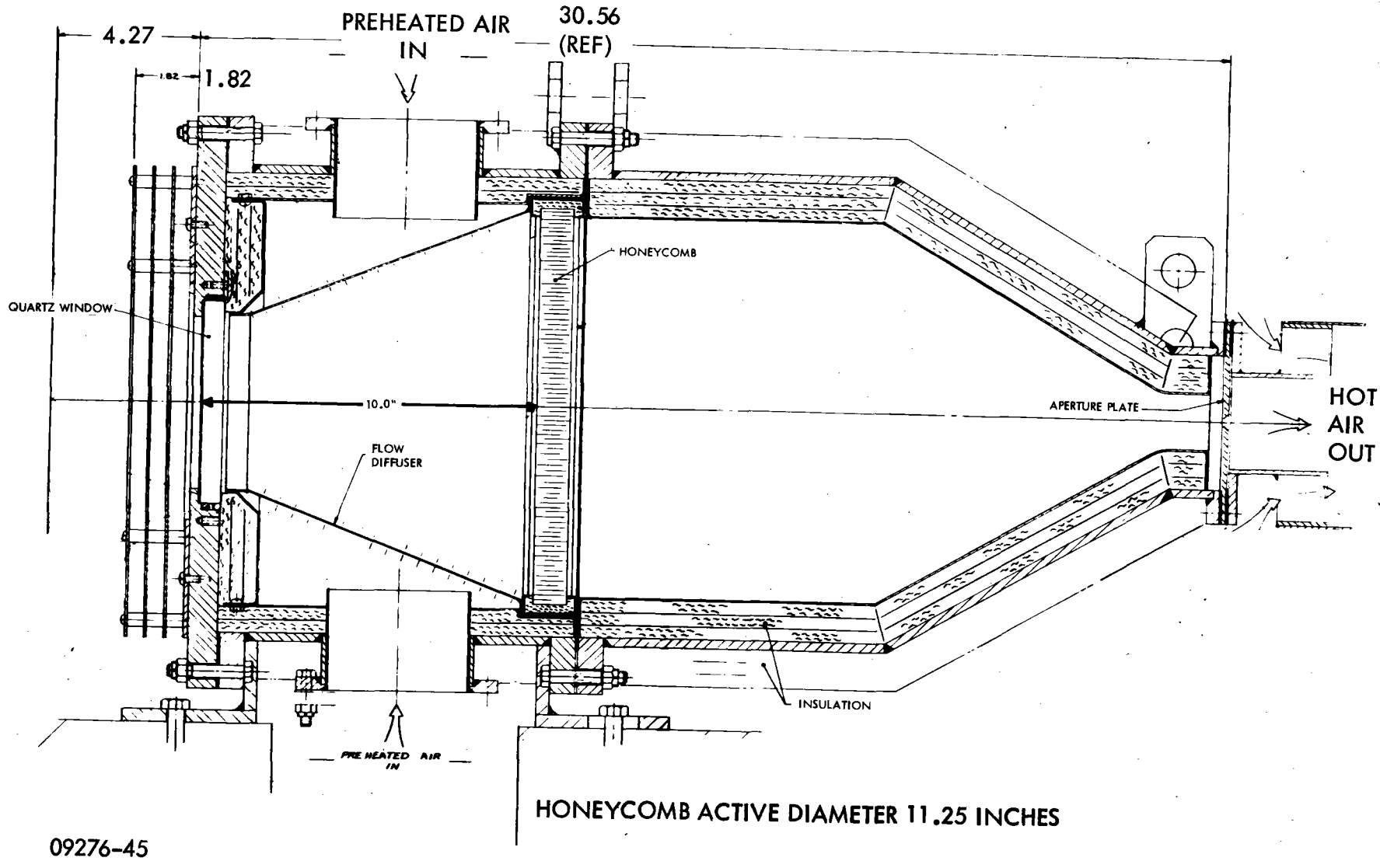

Figure 4-11. 10 KW Solar Receiver

in solar flux; and (b) design parameter such as cavity ratio, concentration ratio and inlet temperatures on the honeycomb temperature and cavity radiation efficiency. It was found that a 7:1 change in solar flux between adjacent tubes caused no reduction in radiation efficiency and only a 1% reduction in honeycomb temperatures.

Results of the parametric study shown in Figure 4-12 depict the honeycomb temperatures as a function of concentration ratio. These simulations were made with the mass flow per unit area and honeycomb surface area determined by the power, and with the maximum air temperature fixed at 1100^{o}C.

Three different air inlet temperatures were selected for each computation. The results of this study were:

- Radiative efficiency improves with increased concentration ratio.
- Inlet temperatures between 425^{o}C and 650^{o}C have negligible effect on efficiency.
- Honeycomb temperature is strongly influenced by the cavity ratio.

As a result, the design parameters selected from the analysis were:

Cavity ratio = 7:1
Concentration ratio = 2000:1
Radiative efficiency = 0.91

4.3.5 Storage

4.3.5.1 Checker Stove Operation

The checker stove is a heat exchange device used since the early 1800's in the glass and steel industries. As shown in Figure 4-13,

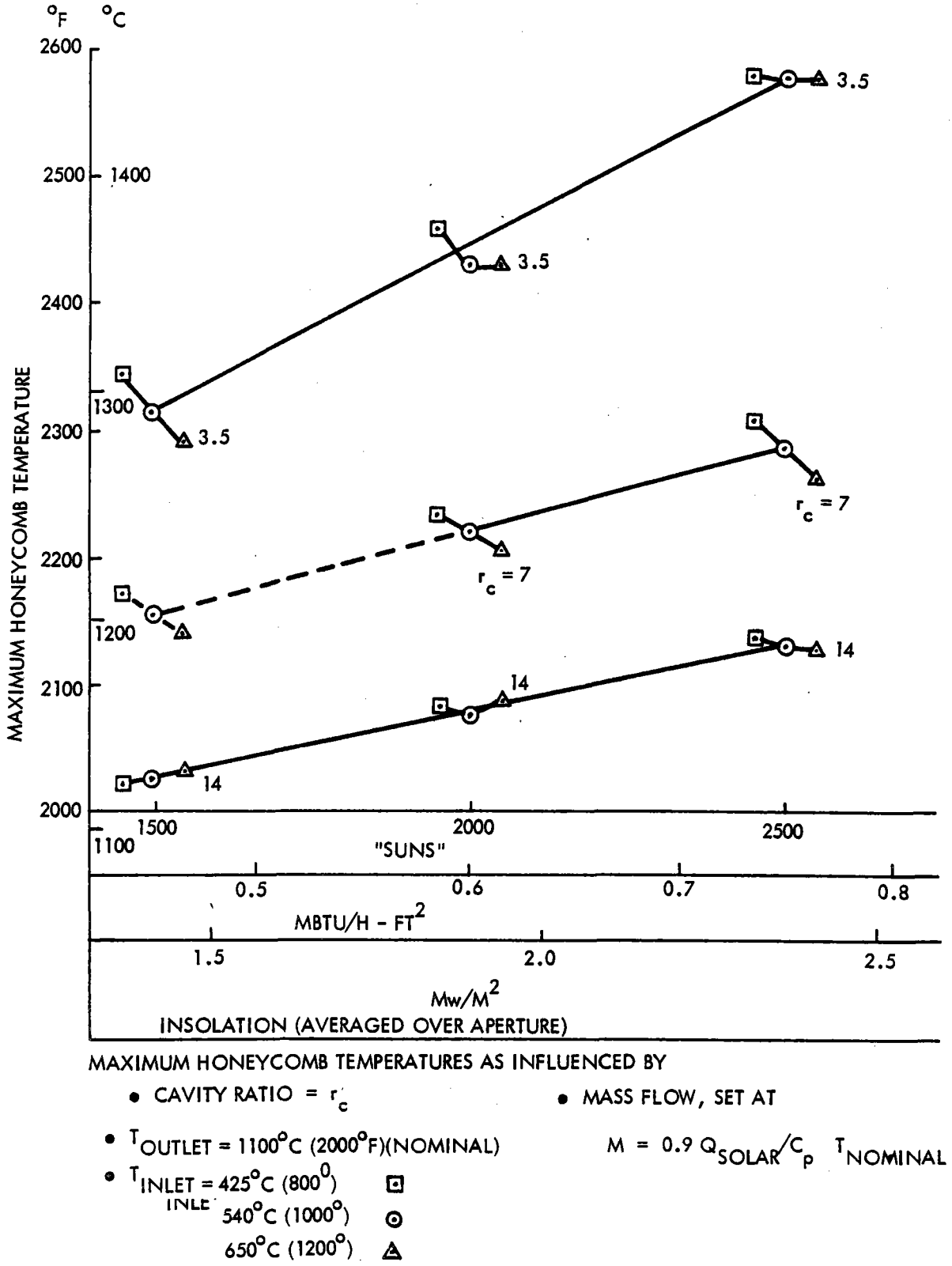

Figure 4-12. Results of Parametric Study - Honeycomb

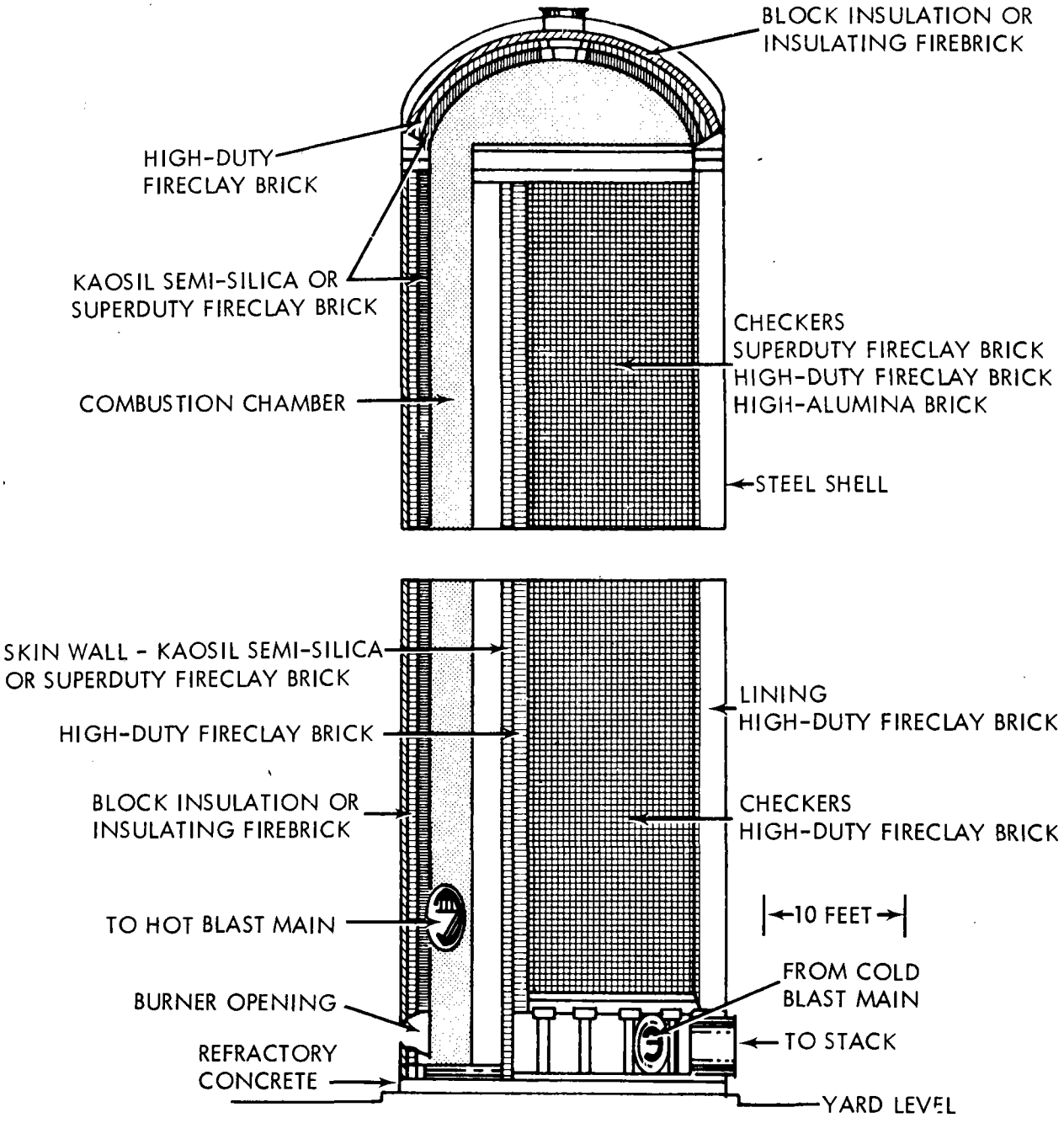

Figure 4-13. Typical Blast-Furnace Stove

it consists of an insulated pressure shell approximately 11 meters in diameter and 40 meters high, containing internal air ducts and a large array of refractory bricks called checkers. The checkers are arranged in stacks, often 30 meters high, forming a large number of individual air passages called flues, through which air can flow. Heat is alternately stored in the checkers, or removed from them during opposing portions of the process cycle. In the steel industry these stoves are used to supply vast quantities of very hot air into the blast furnace charged with iron ore, coke, and limestone. Heat and carbon monoxide released from the coke reduce the iron ore, while the limestone absorbs various impurities. The hot flux of the furnace is piped into a cold stove where heat is extracted for use during the next blast period. In a typical installation, a furnace will have three or four stoves manifolded together with automatic valves, with one or two stoves "on blast" while the others are "on gas" or "on charge". Through an arrangement called staggered parallel operation, the stoves are valved from one position to another to maintain constant output temperatures during the continuous operation of the furnace.

In order to maximize manufacturing efficiency by reducing the amount of coke required, there has been a progressive increase in the blast temperature. Current practice is for an output temperature of at least 1200°C, which is also ideal for efficient gas turbine operation. Furthermore, typical stoves deliver this air at 3 to 4 atmospheres, the pressure required by the furnace combustor. This pressure is close to that required if the stove were to exhaust into a turbine designed for recuperated operation. Operating a gas turbine from a pressurized checker stove was first reported in England[6], and has the unique capability of handling large flow rates with low internal pressure losses, a factor which minimizes pumping losses and maintains high Brayton cycle efficiency.

Not cited in Refs.

In applying checker stoves to Brayton cycle generating plants, the following characteristics are important:

- Ability to store and release huge quantities of heat at high, constant temperatures and at high rates
- Ability to deliver large airflows at low pressure drop
- Ability to operate at desired pressure levels
- Existence of automatic valving techniques to rapidly connect and reconnect stoves

The checker stove performance, shown in Figure 4-14, indicates that the outlet temperature decreases 200°C to 260°C during the discharge cycle, which is an undesireable condition for operating Brayton machinery because it means that either a loss in power and efficiency will occur or makeup heat must be provided.

4.3.5.2 Porous Media Theory

The velocity of the thermocline in a typical blast furnace is estimated as follows:

Air

pressure	=	3 atmospheres
temperature	=	1180°C
flow	=	19.3 m^3/min (880 SCFM)
density	=	0.72 kg/m^3
velocity	=	2.65 m/sec

Porous Media

Firebrick -

ρ	=	1380 kg/m^3
C_p	=	1050 f/cg - °C
$\bar{V}$	=	0.128 cm/sec

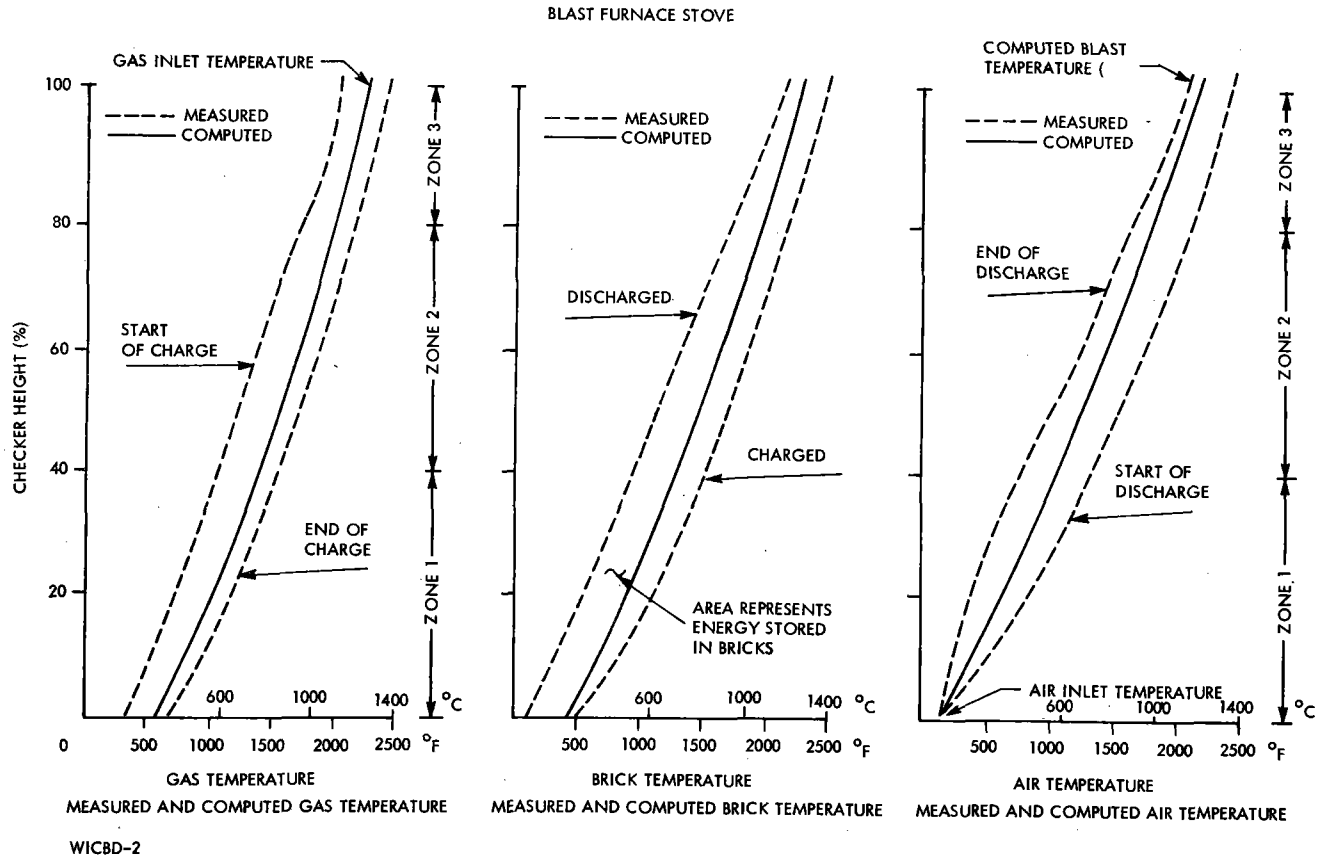

Figure 4-14. Blast Furnace Stove Performance

Again referring to the stove performance curves of Figure 4-14, the lack of a clearly defined thermocline is explained by the fact that in the one hour charging cycle, the thermocline has moved only 1/8 to 1/10 the height of the stove. Upon repeated cycling, the thermocline dissipates and plays no part in the operation of a blast furnace.

Using the differential equations derived for pebble bed heat storage, [4] and the assumption that the heat storage cycle begins at a uniform temperature of 590°C, temperature profiles were computed as a function of time as shown in Figure 4-15. These profiles clearly show the development of a thermocline. Notice that the output temperature is constant for five hours; and even at six hours, only 10% of the step is observed. This 10% represents a loss in power due to the fact that the stove cannot be completely emptied in the allotted time.

4.3.5.3 Efficiency

The primary losses in efficiency are: (a) the thermal losses through the piping and container walls, and (b) the pumping losses incurred in charging and discharging the stoves. Pumping losses are difficult to estimate at low fluid velocity, but a conservative assumption was made that losses equal to two times the velocity head were possible; the maximum velocity is that passing through the hot valves. Considering only those losses associated with charging a stove, the pumping losses total nearly 1%. Using two feet of Babcock and Wilcox insulating firebrick (K-23), for a 1-1/2 hour storage time, thermal loss is estimated at less than 1%. We use 2% for pumping and thermal loss in charging the stove in Position I.

The effectiveness (ε) of the stove as a recuperator in the gas turbine cycle is defined as:

$$\varepsilon = \frac{t_{c\ out} - t_{c\ in}}{t_{h\ in} - t_{c\ in}}$$

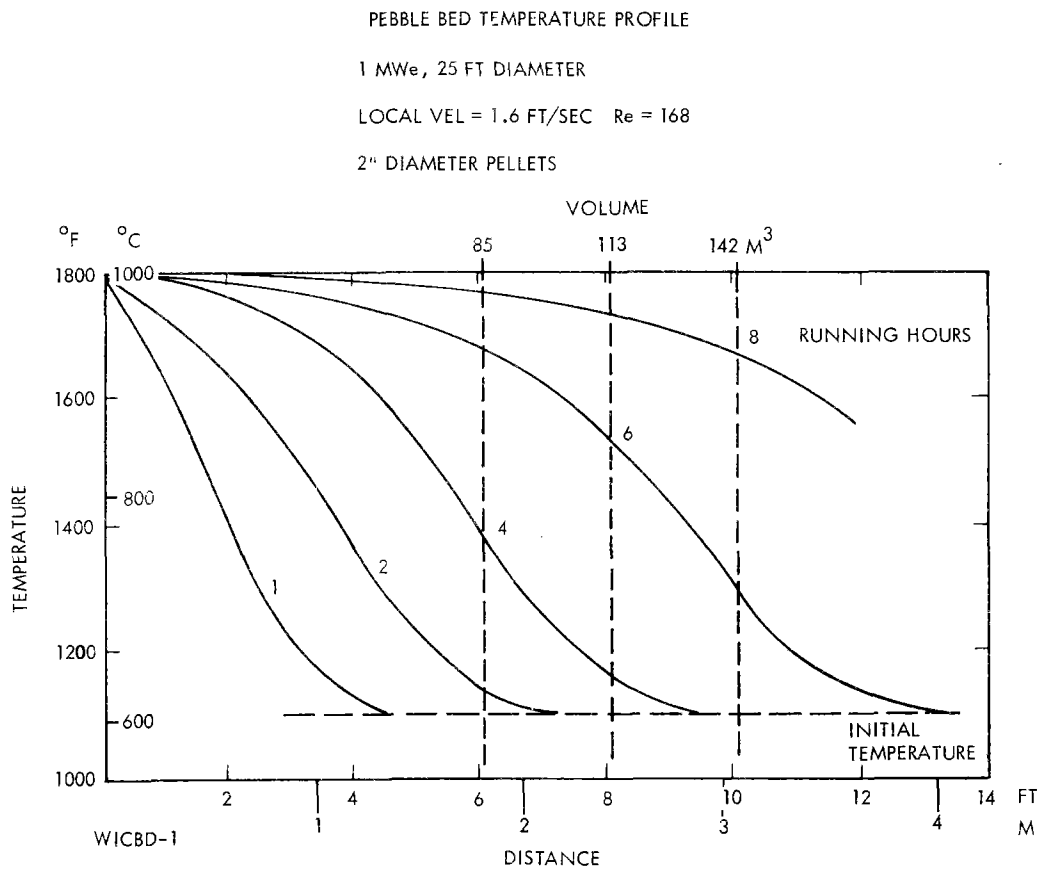

Figure 4-15. Pebble Bed Temperature Profile

where $t_{c\ out} - t_{c\ in}$ is the average temperature rise of the air during discharge cycle, and $t_{h\ in} - t_{c\ in}$ is the temperature rise of the air during the charging cycle. From calculations of thermocline performance, the effectiveness of the sensible heat storage stove as a recuperator is approximately 0.95 for Position II and 0.95 when used in the recovery of turbine heat in Position III.

There are losses associated with the transient produced in switching the stoves. The stove in Position II, which is pressurized, must be depressurized in order to function in Position III. If half of the pressure is expended in pressurizing the next stove to be switched to Position II and the remainder dumped, the loss represents 80 kW-hr per cycle, or 0.05% of the cycle output.

4.4 COST ELEMENTS

4.4.1 Receiver

Receiver cost estimates were made by estimating component costs for the silicon carbide honeycomb, insulation, flow controls, instrumentation, fan, shipping, and installation. G&A and profit were added and then the total cost reduced to 1973 dollars by assuming a 6% per year inflation rate. The cost estimate included 25% for labor and 10% for A&E. The receiver was sized for the mirror field described in Section 4.3. The estimated receiver cost was $81.20/KWe.

4.4.2 Tower

The tower height is an integral part of the mirror field geometry. From studies at Sanders, the cost of towers was found to be a power function of the height. Two examples of towers built to carry large loads are shown in Figure 4-16, the CN tower in Toronto, which is higher than the solar tower and the Tower of America in San Antonio,

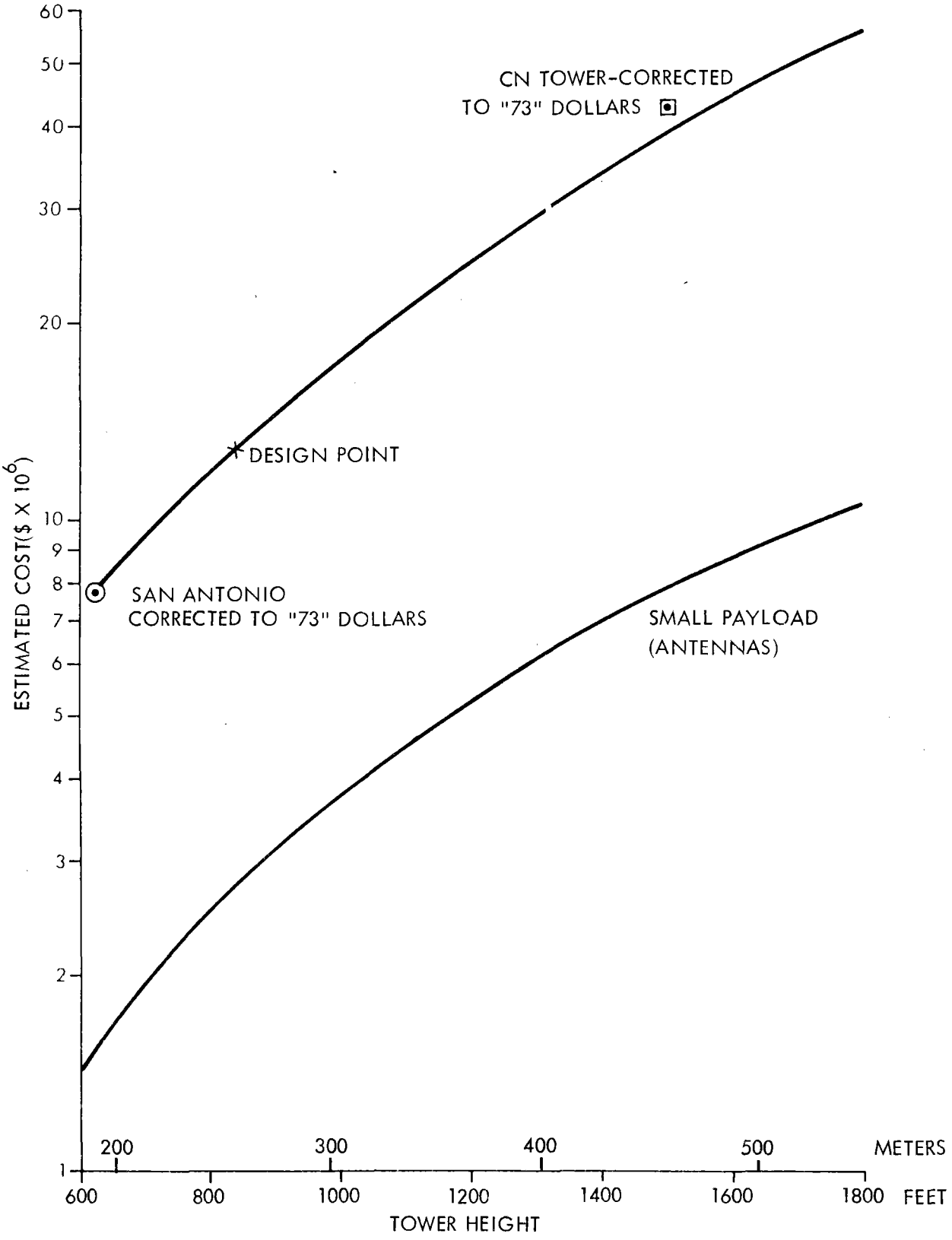

Figure 4-16. Tower Cost versus Tower Height

which is shorter. Costs for both towers were corrected to 1973 collars and plotted on a semi-log scale, as shown in Figure 4-16. Since the slope of this curve fits into the general formula for tower cost as derived at Sanders, the curve was used to relate tower cost and height. The tower data included:

	Tower of America	CN Tower
Date completed	1967	1976
Overall height (m)	230	550
Height to top of house (m)	190	350
Weight of house (kg)	4.9×10^5	1.5×10^6
Cost	$5,500,000	$50,000,000
Corrected to 1973	$7,800,000	$42,000,000

The procedure for obtaining tower cost estimates is to determine the mirror field geometry and the appropriate tower height. In this conceptual design, the tower must position the receiver cavity 233 meters above the ground. Such a tower will be 262 meters high and will cost approximately $120/KWe.

4.4.3 Mirror Field

Sanders did not examine heliostat design or make cost estimates. An estimated cost of $\$60/m^2$ in 1973 dollars was used in the power plant calculations.

4.4.4 Storage

Checker stoves manufactured by Harbison-Walker were the basis for costing the storage vessels. These stoves have high density, commercial firebricks assembled in steel pressure vessels used with insulating firebrick. Sanders' cost estimate of $21.44/kWe-hr included all cost (vessel, insulation, settling chamber at top and bottom and all firebrick).

4.4.5 Electric Generation Cost

Each of the gas turbine power plant manufacturers solicited delivers complete power plants including generator, transformer, starter, exciter and controls. Prices quoted by General Electric in December 1976 for a complete power plant including combustor and controls (a combustor is not needed in Sanders design) are:

7000 series (50 MW class)	=	$110/kW
7000R series (including recuperator)	=	$150/kW
Balance of plant, transformer etc.	=	$15/kW
Installation	=	$15/kW

Using these costs as a reference, the proposed design power plant costs are estimated as follows:

1976 dollar basic plant	=	$110 KWe
balance of plant		15
installation		15
		$135 KWe
reduced to 1973 dollars		113
modification to improve efficiency		56
		$168 KWe

The estimate of an additional 50% to modify the basic power plant is considered more than adequate to obtain the design goals particularly where new development is not required.

4.5 DESIGN POINT COST SUMMARY

The size and cost of the storage stoves depends upon the daily dispatch strategy. Should the dispatch strategy be one of supplying

energy essentially as it is collected only the minimum storage is needed. (The minimum has yet to be defined but it depends upon the operational problems which develop with frequent switching of stoves.) When the dispatch strategy of Section 4 is assumed, the plant component cost are:

Storage	= 300 MWe-hr		
Stove cost	= 4 x 150 x 21.44 x 10^3	=	$12,864,000
Mirror field	= 9700 x 37.2 x 60	=	$21,650,000
Tower	= 262m high, figure 4-23	=	$12,000,000
Receiver	= 100 x 81.20 x 10^3	=	$ 8,120,000
Gas Turbine	= GE 7XXXR modified	=	$16,800,000

4.5.1 Comparative Cost

Table 4-4 summarizes the cost for the Sanders open cycle Brayton power plant. Cost estimates for the various elements are also compared to the EPRI Strawman steam systems. As can be seen, the gas turbine power plant cost and the sum of the tower, receiver and heat exchanger costs are higher with the Sanders concept. However, because of the improved efficiency, reduced mirror field, and the reduced need for cooling, the total cost of the Sanders concept is 77% of the EPRI steam Strawman. A cost of $926.44/KWe based upon the 1973 dollar, is projected for installation of a Sanders open cycle power plant.

4.5.2 Performance Summary

The design concept described has been constructed from the best information available during the period of investigation. Specifications as summarized in Tables 4-5 to 4-8, form a baseline concept which must be further definitized with design data and engineering trade-off studies. Component efficiencies are described and an efficiency ladder shown in Figure 4-17 shows the elements which lead to an overall efficiency of 0.30 for the Sanders open cycle gas turbine power plant.

at the design point (June 21)

TABLE 4-4. COMPARATIVE PLANT COST $/KWe
(1973 dollars)

	EPRI Strawman (Steam)	Sanders (Open Cycle Air)
Turbine/Elec	$ 101.00	$168.00
Struct/Fac	44.00	44.00
Land	2.00	2.00
Heliostats	600.00(1)	216.00(1)
Heat Exchanger	95.00	
Tower	-	120.00
Receiver	-	81.20
Subtotal	$ 95.00	$631.20
Cooling	20.00	-
Thermal Storage	180.00(2)	128.00(3)
Hot Pumps/Piping	-	42.40
Misc. Plant	4.00	4.00
Subtotal	$1,046.00	$805.60
Contingency (5%)	52.00	40.28
Spares	-	-
Indirect (10%)	105.00	80.56
Subtotal	$ 157.00	$120.84
Total	$1,203.00	$926.44
(1978 dollars	$1,610.00	$1240.00)

(1) Collector Cost $60/M^2

(2) Thermal Storage $30/KWHe

(3) Thermal Storage $21.44/KWHe

TABLE 4-5. SYSTEM SPECIFICATION

Nameplate capacity:		100 MWe	
Storage (2 stoves)		3 Hours	
Mirror field:		Offset north	
Mirror field area:		0.93 km^2	
Number of heliostats:		9700	
Heliostat area:		37.2m	
Tower maximum height:		262m	
Weight of tower payload:			
4 Storage Stoves		12.0×10^6 kg	
Receiver and fan		3.0×10^6 kg	
Gas turbine-generator		0.5×10^6 kg	
Tower enclosure		2.5×10^6 kg	
Base		46.0×10^6 kg	
	Total	64.0×10^6 kg	
Cooling:		AIR	
Structural design specification:		Seismic zone 3	
Mirror reflectivity	Heliostat	0.91	0.731
Tracking efficiency	Heliostat	0.89	0.731
Spillage	Heliostat	0.03	0.731
Internal reflectivity loss		0.07	
Overall efficiency		0.30	

TABLE 4-6. RECEIVER SPECIFICATIONS

Cavity height:	233m
Concentration ratio:	2000
Rim Angle:	62^{o}
Cavity ratio:	10
Cavity diameter:	15.1m diameter
Wind screen and concentrator:	38.1m diameter
Offset angle from vertical:	14^{o}
Conducting medium:	Air (ambient pressure)
Airflow	270-540 kg/sec
Maximum temperature:	$1200^{o}C$
Radiative efficiency:	0.91
Total receiver efficiency:	0.874

TABLE 4-7. STORAGE SPECIFICATIONS

Number of stoves:	4
Volume per stove:	1873 m^3
Stove dimensions:	13.4m dia. X 13.4m high
Maximum pressure:	4 atmospheres
Maximum storage temperature:	1200°C
Sensible storage material:	10.6 X 10^6 kg of mullite (50% open area)
Weight of ceramic in 1 stove:	2.64 X 10^6 kg
Weight of tank, insulation & valves:	2.7 X 10^5
Charge cycle (ambient pressure)	
- Airflow:	250 to 550 kg/sec
- Pumping power:	1.7 MW
- Max velocity at min section (valve)	30 m/sec
- Max velocity at top of bed:	4.6 m/sec
Overall effectiveness:	0.98

TABLE 4-8. POWER PLANT SPECIFICATIONS

Gas turbine:	Westinghouse WD501 modified
Electrical generator:	Westinghouse 100 MWe generator
Compression ratio:	4:1
Turbine inlet temperature:	1100^{o}C
Mass flow (total)	525 kg/sec
Thermal-to-electric efficiency	0.490

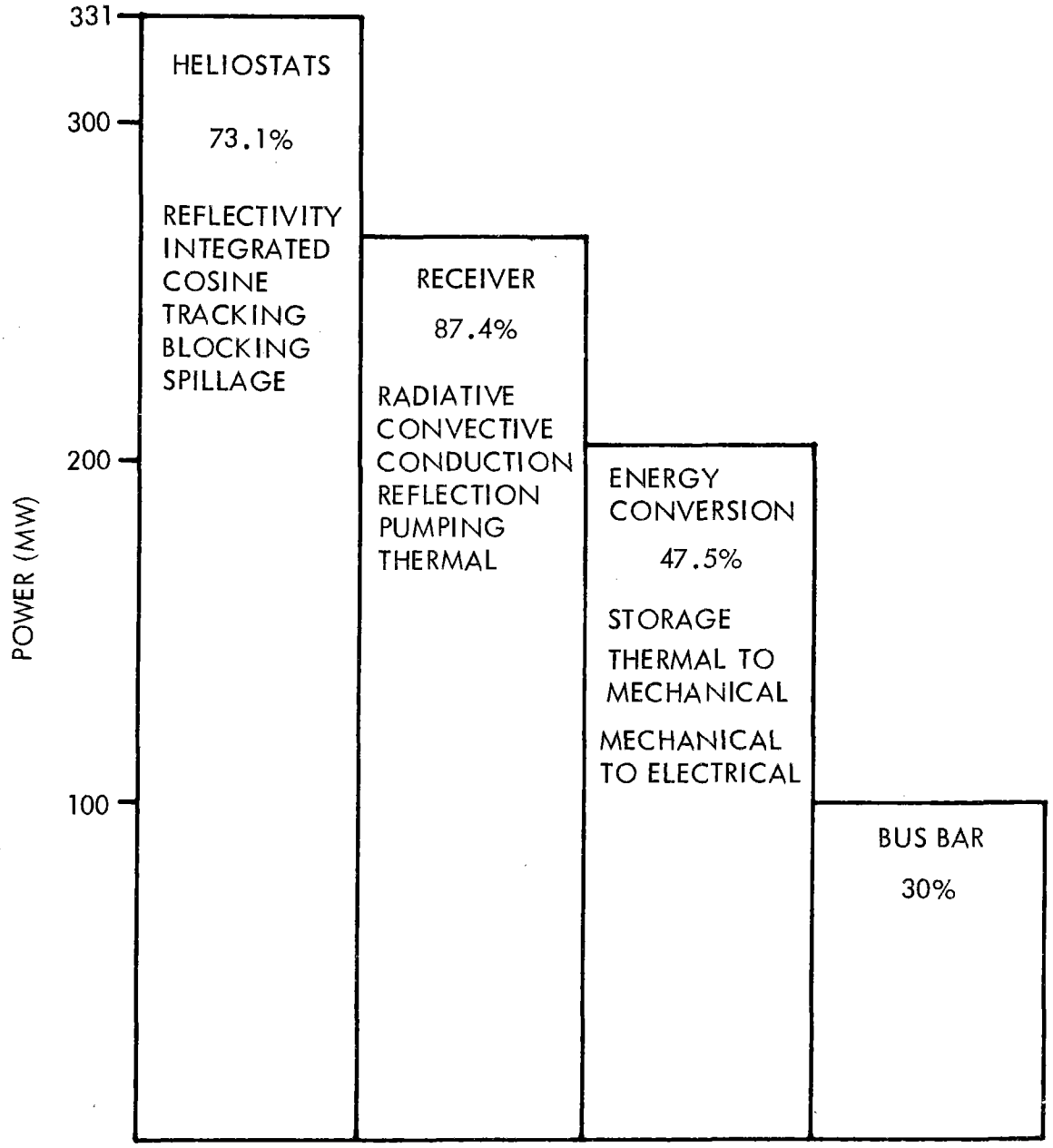

Figure 4-17. Efficiency Ladder - Solar Input

REFERENCES

(1) Solar Thermal Power Systems Based on Optical Transmission, National Science Foundation Report, NSF/RANN/SE/GI-39456/FR-753.

(2) Harris, Cyril and Crede, E. Charles, Shock and Vibration, Vol. III, McGraw-Hill (1961).

(3) Gas Turbine Principles and Practice, Sir Harold Roxbie Co., Newness, London, England (1955).

(4) Löf, G.O.G. and Hawley, R.W., Unsteady State Heat Transfer between Air and 100 se Solids, Industrial & Engineering Chem. 40, No. 6, pp. 1061-1070, H10498.

(5) EPRI Strawman, 1973.

SECTION 5
CONCLUSIONS

The objective of this program was to develop, build and test a solar energy receiver using air as the working fluid. The unit was to be designed to provide air at 925^{o}C with an efficiency of at least 0.70.

The initial test goals have been exceeded, reinforcing the underlying premise that the use of large scale receivers with high outlet airstream temperatures (1100^{o}C) to provide the thermal input to a Brayton cycle turbine will yield efficiencies which are competitive with steam (Rankine) cycles for commercial electric power generation. Air, when used as a working fluid in an open cycle, avoids many of the practical problems plaguing systems using other working fluids, while retaining high overall energy efficiencies and economic performance. The present test program and the associated design studies have confirmed the initial expectations and have increased confidence in the design methods and the overall feasibility of energy conversion systems based on the open cycle air receiver technology.

During this program, it was found that solar receivers with energy capture efficiencies (solar radiation on a honeycomb to heat in an airstream) exceeding 0.85 could be designed, using available honeycombs and other components. A specific version was selected, built, tested and evaluated at the White Sands solar test facility in New Mexico. These tests met expectations on energy capture efficiency. Other test parameters, such as temperatures, were shown to agree with the basic theoretical model. With the planned incorporation of solar flux and mass flow inhomogeneity effects, among refinements, the theoretical model will be useful in the design of larger scale solar receivers.

Efficiencies as high as 0.85 were realized for the receiver. These results are notable considering the range of experimental parameters, including solar flux input, air inlet temperatures, and airflow rates. Of most interest is the importance of inhomogeneities in solar flux and airflow, which account for the very significant differences between data taken in the FORWARD (10:1 flux variation) and AFT (3.5:1 flux variation) locations of the receiver. The former position locates the receiver aperture in the plane of best focus of the solar facility; the latter is 11 cm aft.

A 100 MWe receiver conceptual design has been developed using a novel storage/recuperation concept. This concept can provide significant economic and performance advantages for solar plants since it permits operation from storage at the nameplate rating. In addition, waste heat can be rejected directly to the ambient atmosphere as exhaust air. This eliminates the need for either cooling water or expensive dry cooling towers. The concept advocated by Sanders is also economically attractive and provides a system with a relatively low initial capital investment compared to alternative solar thermal power conversion concepts.

To summarize the highlights of the program:

- Efficient solar receivers can be designed using air as a working fluid.
- Good agreement between model and experiment has been obtained in the test program.
- Reliability of projections of the design model to larger scale receivers has been increased.
- The predicted low pressure drops for airflow through the honeycomb structures were confirmed at less than one inch of water.

- The value of solar-blind infrared scanning in providing receiver temperature measurements was demonstrated against a background of highly concentrated solar flux (see Section 3.5.4).

- The result of the conceptual design indicates that Sanders' Split Cycle Solar Brayton System offers significant cost advantages over alternate central receiver solar systems.

APPENDIX A
EMISSIVITY MEASUREMENTS
ON
SILICON CARBIDE

APPENDIX A
EMISSIVITY MEASUREMENTS ON SILICON CARBIDE

The emissivity (ε) of the receiver material is one of the major parameters affecting solar radiation capture efficiency. Therefore, measurements were made on samples of the type of material to be used in the solar receiver test program in the spectral region of interest for solar absorption. In addition to measurement of the emissivity at representative temperatures, efforts were directed at measurement of polar scattering patterns, primarily to examine the possible influence of surface texture.

In the optical and near infrared regions of the spectrum, values for ε of 0.90 or greater were measured at temperatures of 1200^{o}C or higher. The scattering pattern was found to be basically Lambertian; enough so to serve as the basis for computer simulation of any incident rays that were not absorbed on a receiver surface at first incidence.

Experimental measurements were made of the emissivity of silicon carbide. The measurements were made at three wavelengths (.753μ, .896μ and 1.06μ) and at various angles relative to a line normal to the face of the silicon carbide.

The silicon carbide was electrically heated to an average temperature of 1120^{o}C. The temperature of the silicon carbide was measured with an optical pyrometer. The equipment used to perform the measurements was reference-calibrated to a blackbody type source whose temperature was measured with a thermocouple (see Figure A-1).

The emissivity of the silicon carbide was determined from the following relationship:

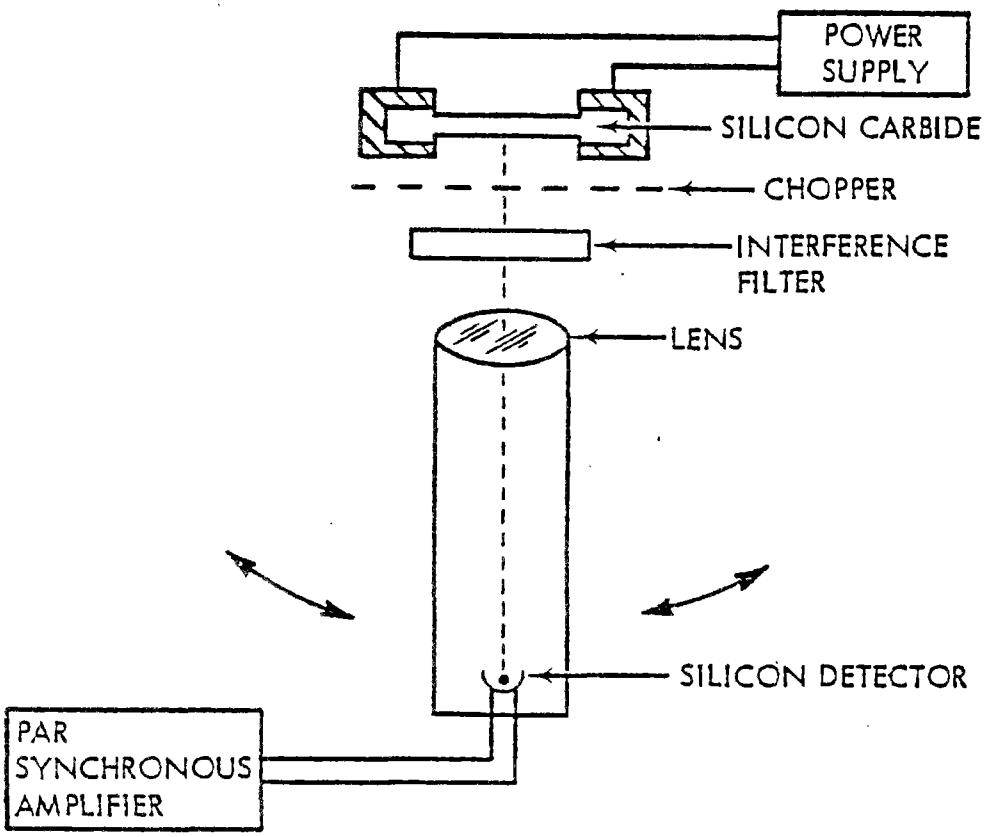

Figure A-1. Silicon Carbide Emissivity Measurement

$$\frac{V_{sc}}{\varepsilon_{sc} N_{sc}} = \frac{V_{bb}}{\varepsilon_{bb} N_{bb}} \quad \text{or} \quad \varepsilon_{sc} = \frac{\varepsilon_{bb} N_{bb} V_{sc}}{N_{sc} V_{bb}}$$

where

V_{sc} = detector signal at each wavelength for silicon carbide

N_{sc} = radiance of blackbody type source at measurement temperature

ε_{sc} = emissivity of silicon carbide

V_{bb} = detector signal at each wavelength for blackbody

N_{bb} = radiance of blackbody type source at measurement temperature

ε_{bb} = emissivity of blackbody type source = 0.99 $\pm$ 0.01

The results of the measurements are given in Table A-1

TABLE A-1. SILICON CARBIDE EMISSIVITY

Angle from Normal (degrees)	0.753μ	0.896μ	1.06μ	Temperature (°C)
0	0.98 ± 0.07	0.94 ± 0.07	0.97 ± 0.07	1134
15	0.95 ± 0.07	0.96 ± 0.07	1.0 ± 0.07	1127
30	0.96 ± 0.07	0.96 ± 0.07	1.0 ± 0.07	1120
40	0.92 ± 0.07	0.90 ± 0.07	0.93 ± 0.07	1145
50	0.98 ± 0.07	0.92 ± 0.07	1.0 ± 0.07	1087
60	0.82 ± 0.06	0.79 ± 0.06	0.85 ± 0.06	1087

The largest uncertainty in the measurement is attributed to the temperature measurements made with the optical pyrometer which (because it is a visual instrument) is only accurate to about $\pm 5^{o}C$. This amounts to an uncertainty of $\pm 5\%$ in radiance at the temperatures and wavelengths for which the measurements were done. Signal variations in the blackbody filter measurement were about $\pm 2\%$. The large decrease in emissivity at 60 degrees probably resulted from the projected increase in source size at this viewing angle which then included the cooler ends of the silicon carbide.

A first order correction to the color temperature of the silicon carbide as measured with the single color optical pyrometer is shown in Table A-1. The corrected results are shown in Table A-2.

The reflectance of a piece of silicon carbide was measured at 0.6328μ using an HeNe laser (see Figure A-2). The silicon carbide was electrically heated to a temperature of $1130^{o}C$. The reflectance was measured at various viewing angles and for different angles of incidence of the laser beam.

The equipment was reference-calibrated using a magnesium oxide block as a diffuse white reflectance standard. This reference calibration was done for a 0 degree incident laser beam (relative to the surface normal) and for a viewing angle of 15 degrees.

The results of the measurements are listed in Table A-3. The silicon carbide reflectance measurements were done at such a low signal level that even with the time response of the PAR at 10 seconds, the signal variations were about $\pm 6\%$.

TABLE A-2. SILICON CARBIDE SPECTRAL EMISSIVITY

ANGLE FROM NORMAL (DEGREES)	0.753μ	0.896μ	1.06μ	TEMPERATURE (^{o}C)
0	0.90 ± 0.07	0.88 ± 0.07	0.92 ± 0.07	1143
0	0.92 ± 0.07	0.96 ± 0.07	0.94 ± 0.07	1142
15	0.88 ± 0.07	0.90 ± 0.07	0.95 ± 0.07	1136
30	0.89 ± 0.07	0.90 ± 0.07	0.95 ± 0.07	1129
40	0.86 ± 0.07	0.85 ± 0.07	0.89 ± 0.07	1154
50	0.90 ± 0.07	0.86 ± 0.07	0.94 ± 0.07	1096

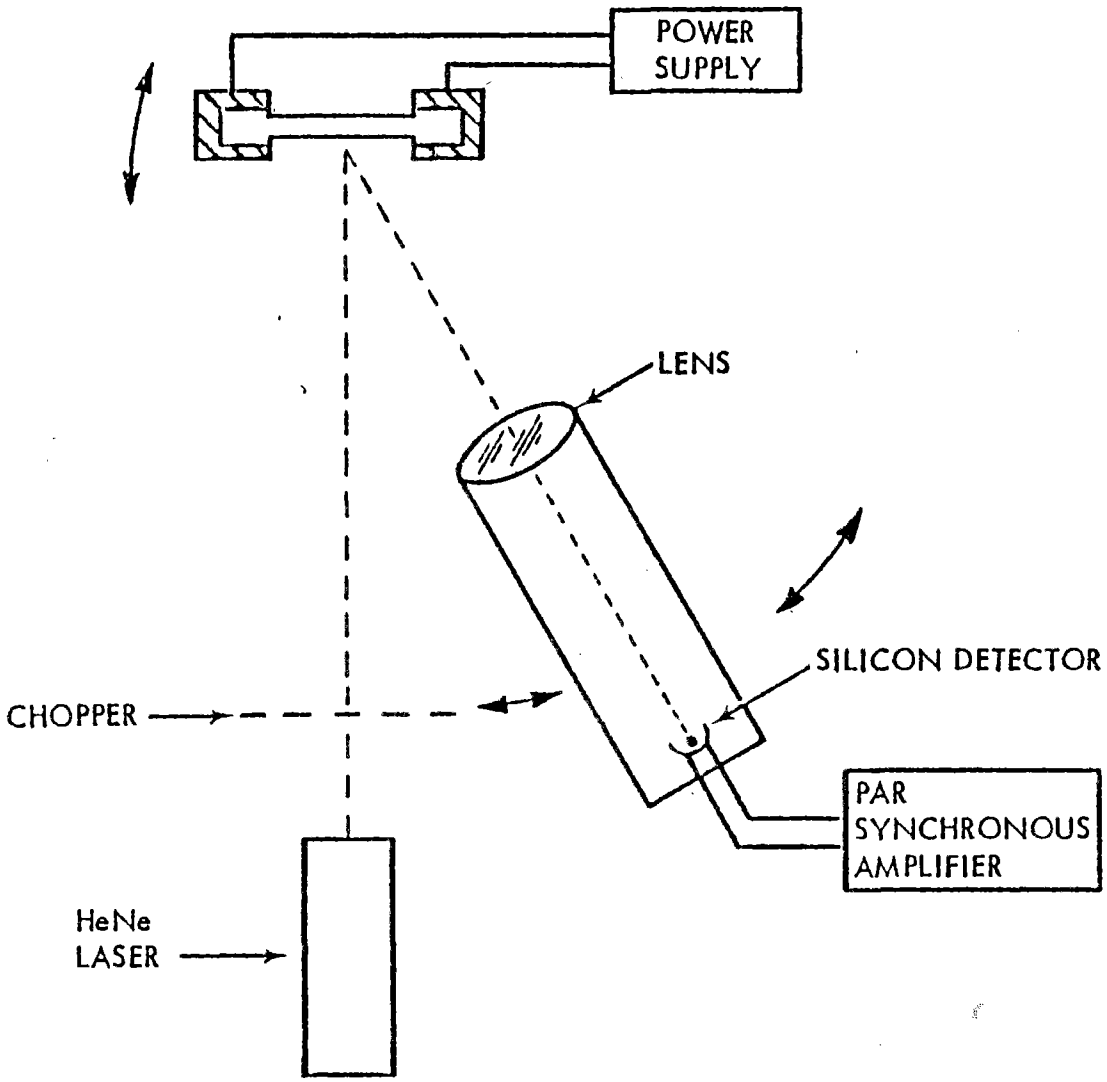

Figure A-2. Silicon Carbide Reflectance Measurement

TABLE A-3. SILICON CARBIDE REFLECTANCE

ANGLE OF INCIDENCE					
0^{o}		10^{o}		25^{o}	
REFLECTANCE ANGLE	REFLECTANCE	REFLECTANCE ANGLE	REFLECTANCE	REFLECTANCE ANGLE	REFLECTANCE
15	.101	-5	.103	5	.0810
30	.102	10	.116	20	.0930
40	.0984	20	.127	25	.0992
50	.0974	25	.106	30	.0975
60	.102	35	.108	35	.0942
-15	.0848	45	.112	45	.113
-30	.0904	55	.111	55	.119
-40	.0841	-35	.0942	65	.159
-50	.0946	-45	.102	-10	.0861
-60	.0946	-55	.095	-35	.101
		-65	.108	-45	.0911
				-55	.0857

42.5^{o}		55^{o}	
REFLECTANCE ANGLE	REFLECTANCE	REFLECTANCE ANGLE	REFLECTANCE
2.5	.0984	0	.0983
17.5	.102	15	.101
32.5	.116	30	.116
37.5	.151	35	.144
42.5	.185	40	.155
47.5	.180	45	.165
52.5	.181	50	.178
62.5	.213	55	.235
-12.5	.0958	-15	.0923
-27.5	.102	-30	.103
-57.5	.122	-40	.105

Table A-3 and Figures A-3 through A-7 represent the results of the silicon carbide reflectance measurements. The reflectance of an electrically heated (1130^{o}C) silicon carbide rod was measured using an HeNe laser as a source of 0.6328μ radiation. The laser beam was incident on the rod at various angles from 0 degrees to 55 degrees relative to the rod surface normal. Reflectance was measured at several angles and plotted as a fraction of maximum reflected energy for each incident angle. The laser position and the normal to the SiC rod surface are both indicated on each graph.

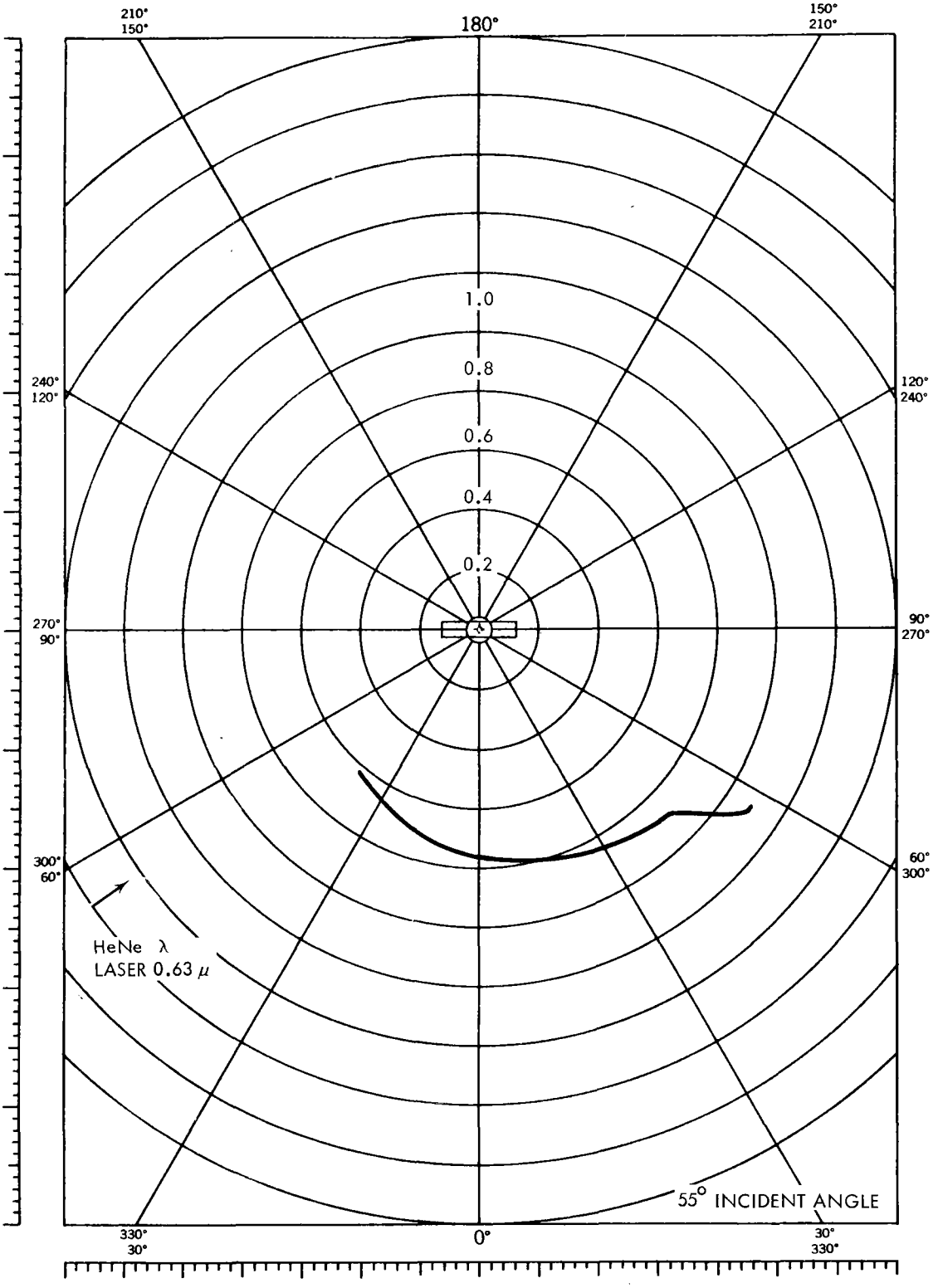

Figure A-3. Silicon Carbide 55 Degrees Incident Angle

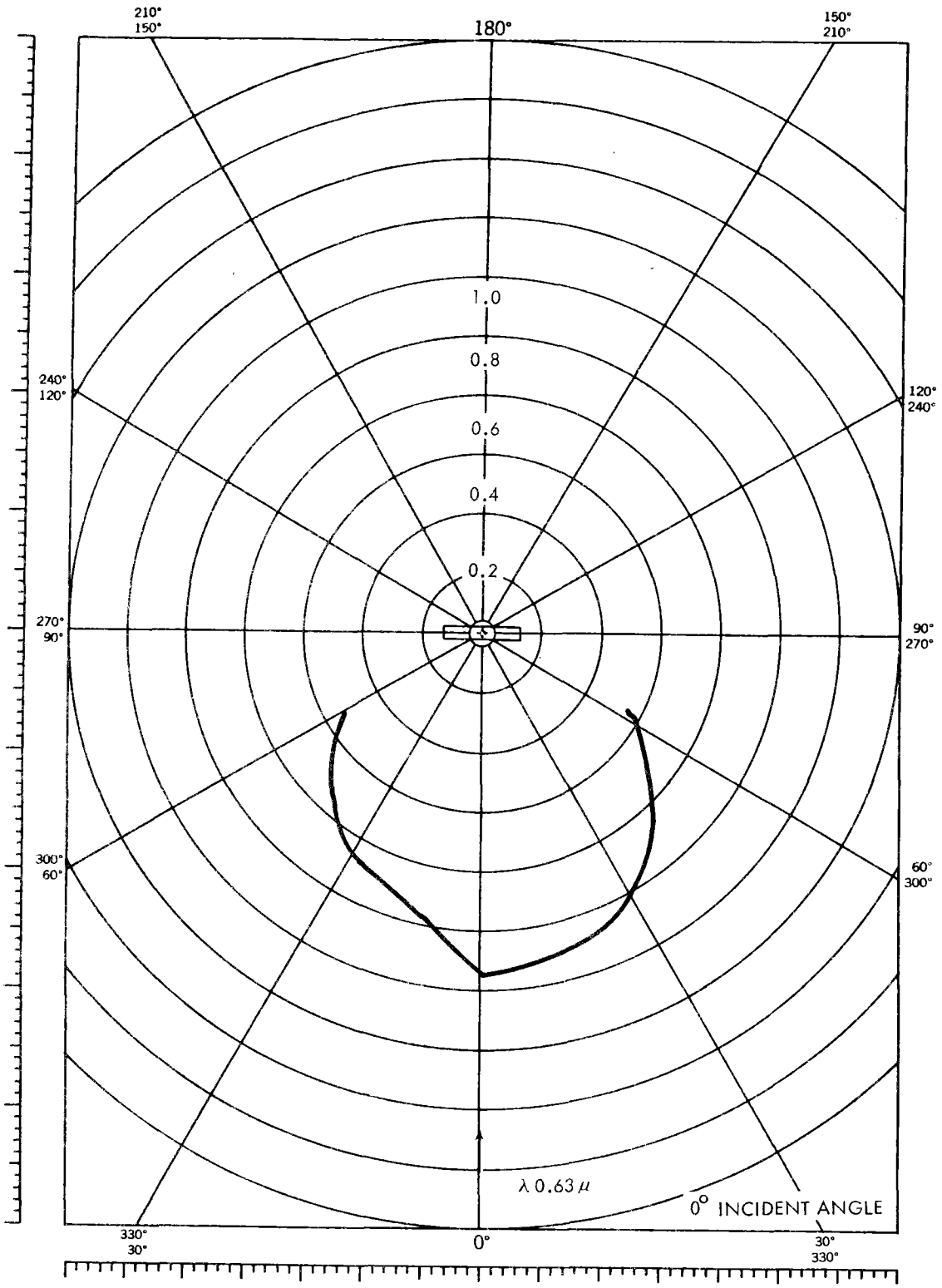

Figure A-4. Silicon Carbide 0 Degree Incident Angle

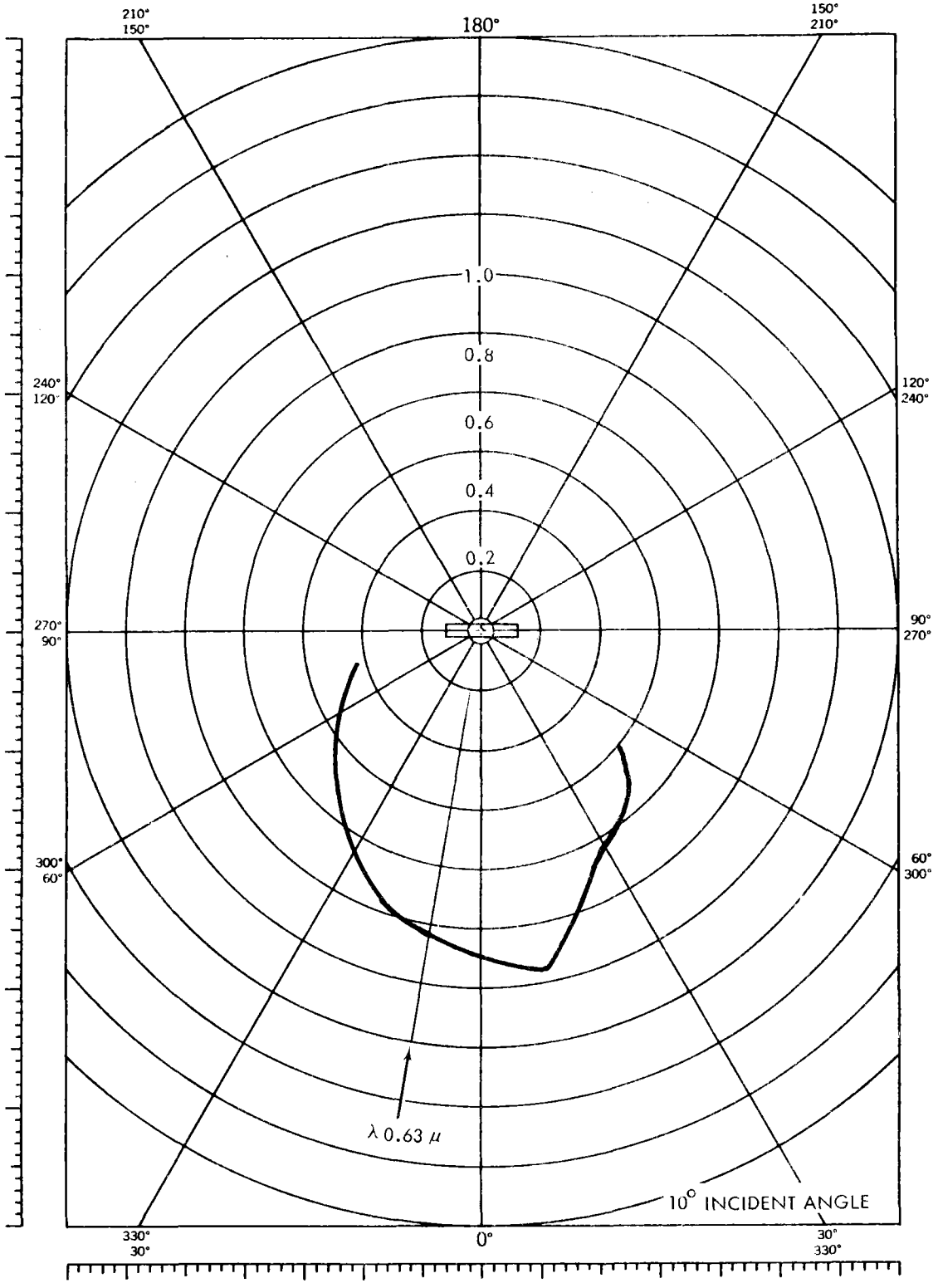

Figure A-5. Silicon Carbide 10 Degrees Incident Angle

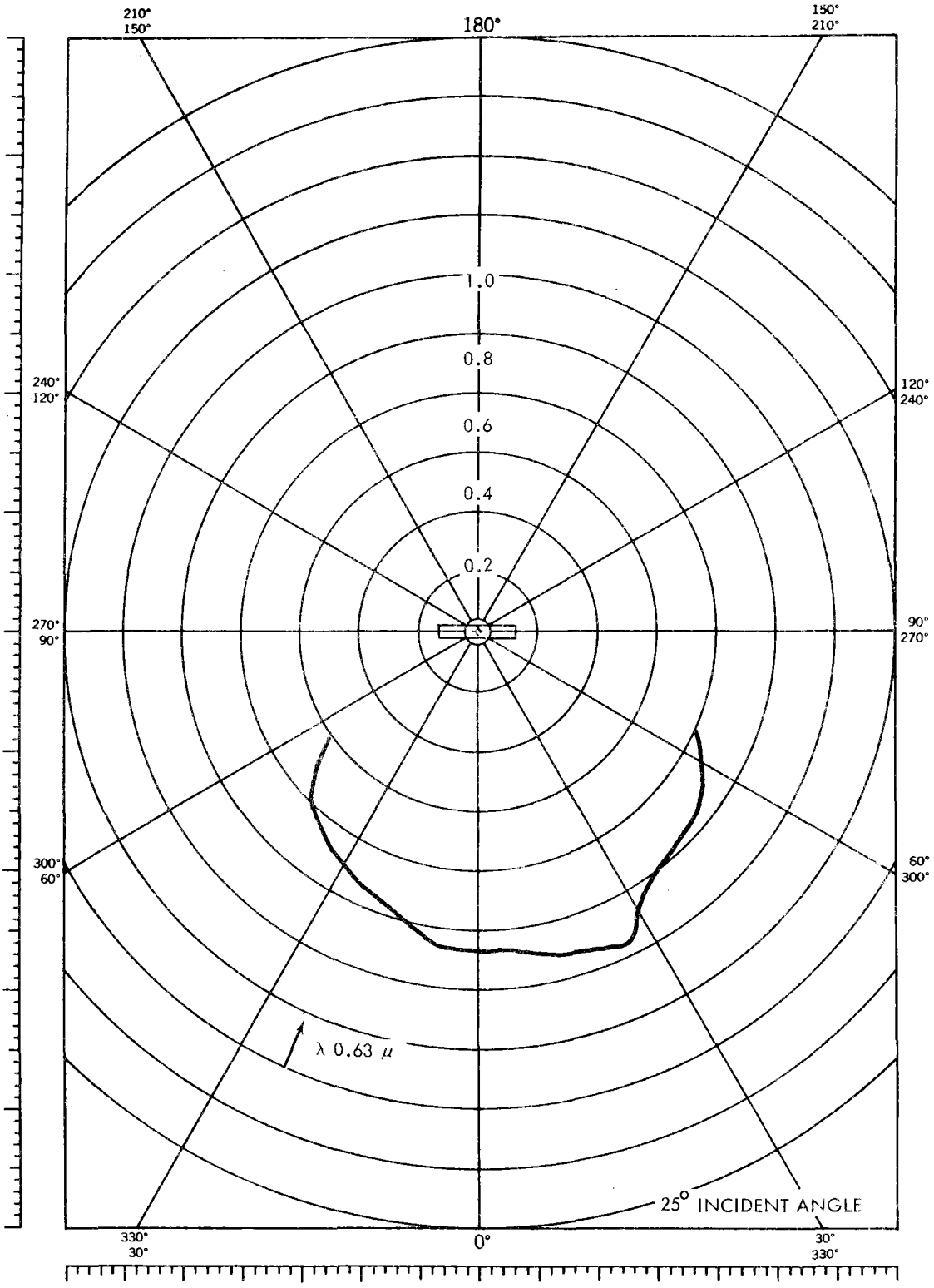

Figure A-6. Silicon Carbide 25 Degrees Incident Angle

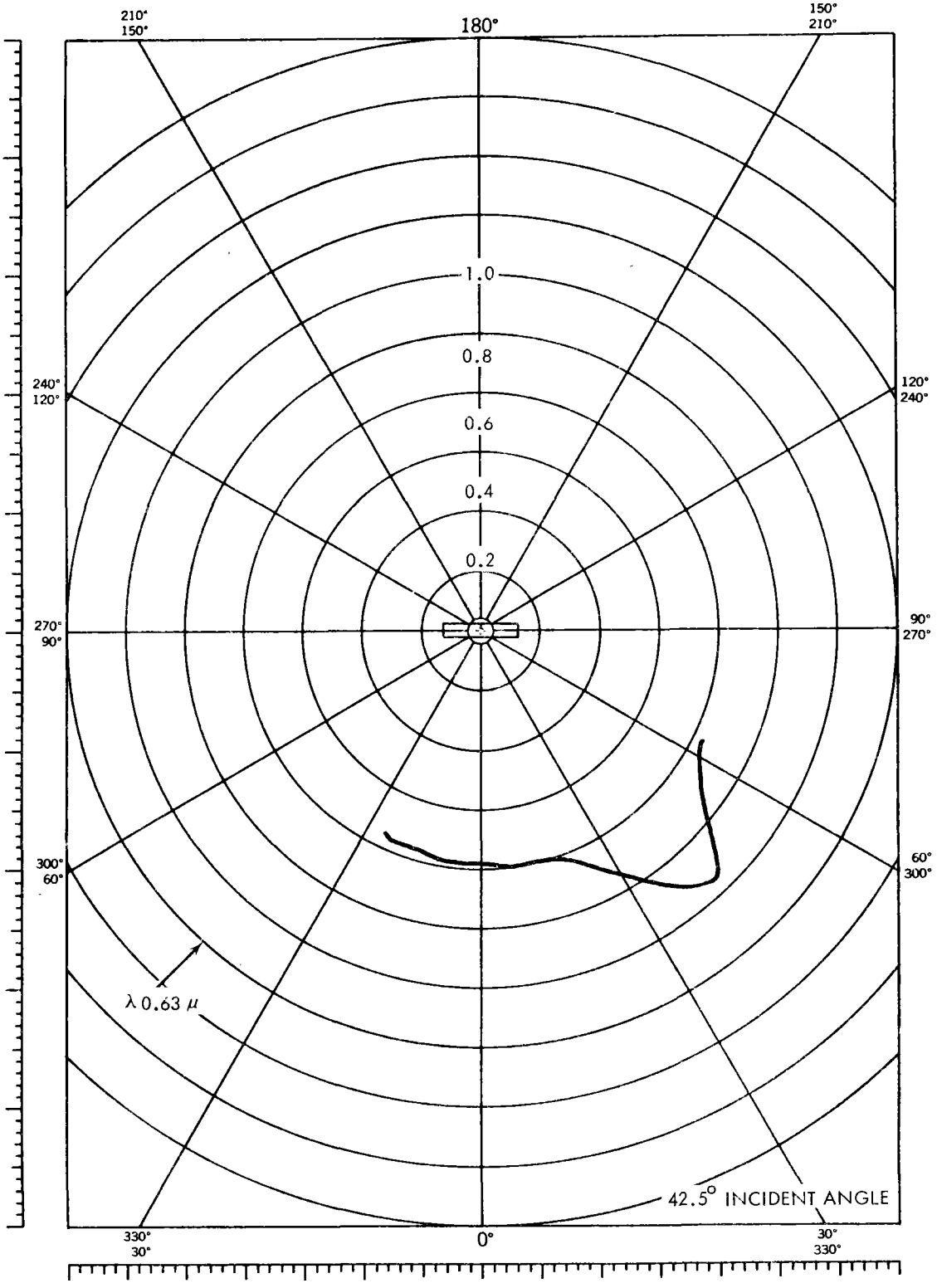

Figure A-7. Silicon Carbide 42.5 Degrees

Review of Sanders Associates Draft Final Report COO-2823-2, dtd. Dec. 77

The following comments and observations were noted during review:

p. 1-5, Fig. 1-2: The three checker-stove configuration shown does not jibe with the two-stove system with separate regenerator discussed in Section 4. The currently-preferred configuration should be indicated.

p. 2-1, 2nd line from bottom: "...surface, and θ and ϕ, specifying..."

p. 2-4: Define the symbol ξ, where it first appears.

p. 2-6: The ξ and η axes are inconsistently defined in the figure.

p. 2-7: Numerous examples of poor mathematical proofreading:

Use of ϵ for ξ, and n for η, in the upper equation and definitions;

Need to define N_F, and to add = sign in text equation for $p(\theta)$.

p. 2-11: Geometrical discussion in last paragraph of Section 2.1.2 unclear.

p. 2-13; 3rd line of text: Replace δ' by σ'.

p. 2-17; last line: Relocate comma: "...outputs, but not..."

p. 2-24: parameter list for curves (9): "h = 10".

p. 2-26, first line of lower subparagraph (3): close quotes after "..number,"

p. 2-27, second line of 2.3: "...area, and A_{sfce} as the..."

p. 2-29, second line of upper eqn.: close firs parens.; replace u by μ.

Define symbol ζ on first appearance, in paragraph C.

p. 2-28, bottom line of caption: word missing after "higher..."

p. 3-9: In fifth line from top, either "4.4°C" or "(40°F)" must be wrong.

p. 3-19, fourth text line: the reference to "scatter" in Figure 3-6 is unclear; no points are shown in the Figure of this number on p. 3-8. This figure is referenced in , paragraph 3.4, not 3.1. Is some other figure meant?

p. 3-20; para. 3.7.2.2: The solar-blind infrared scanner is not discussed (although some discussion was provided in the test report, COO-2823-1); Either the reference in the last sentence should be omitted, or a brief discussion should be provided.

2: The efficiencies given at the top of the page combine to an overall efficiency of 29.9%, not 27.3%.

Same page, para. 4.2.1.1, 4th line: delete "...over efficiency..."; last line of same para.: "...built..."

p. 4-3, Figure 4-1: Units along y-axis garbled.

p. 4-4, first line of table at bottom: "Pressure ratio$"

p. 4-7, 10th line, next-to-last word: "...displacement..."

p. 4-11, Figure 4-4: although cited in the text, the reference day, June 21, should be also indicated in the figure.

p. 4-14; last line of second para, section 4.2.3.4.1: "...$25.8M..."

p. 4-17: The "...three large steel struts..." are not shown at all in Figure 4-9 (although they are hinted at in Figure 4-10).

p. 4-20, first line: "...machinery operates from the other."

" " , 20th line: "... from 0.28 to 0.32."

p. 4-25, first line "...response to known earthquake..."

p. 4-33: the reference after the symbol "+" should be to Figure 16.

p. 4-34; fifth line of para. 4.3.3.3: "...and radiative efficiency reached..."

" " , first "bullet": the maximum efficiency increase is 3.5 - 4%, not 5%.

" " , last line of second "bullet": "...with T_{out}= 1100°C."

p. 4-35, Figure 4-17: add note on offset of T_{in} points, as in Figure 4-18.

p. 4-39, Sect. 4.3.4.2, last para.: "...400 - 500 degrees F during discharge, an undesireable condition..."

p. 4-41, first paragraph: Put definition of h, d, K in parens.

p. 4-42, line 3: "...at a temperature..."; clarify.

" " , line 8: "...exists..."

" " , line 5 from bottom: Clarify reference to dockets 3461, etc.

p. 4-50, Table 4-5, lines 6 - 8: "...Mod$-Pod 50's..." (?); "...Thermal to..."

p. 4-52, Table 4-6: EPRI Strawman upper subtotal is $842, not $95; bottom subtotals and totals in this column and middle column are garbled.

p. 4-53, Sect. 4.5.1, line 3: "...the ground to a ground-based..."

p. 4-55, line 3: "...the GE unit thermal efficiency..."

p. 4-56, Section 4.5.4: After mentioning the effect of winds on convection losses, a brief discussion of the convection loss tests would be in order; at the least, a reference to the present contract and its

final report should be made.

p. 4-57, bibliography entry 3): "Harris, Cyril...Vol. III..."

" " " " 4): "Löf, G.O.G....": clarify "...100 se solids.."

" " " " 5): "Close, D.J...."

" " " " 6): "Schumann, T.E.W..."; delete close-quotation mark after word Transfer

p. 5-3, first bullet: The solar-blind infrared scanning measurements are not discussed in this report (unless the reference is to the optical pyrometer measurements described in Appendix A; if this is the case, a reference to this Appendix should be made, and the instrumental description beefed up).

p. A-2, 3rd para., 3rd line: "...relative to a line..."

" " 4th para., 4th line: "...was referenced calibrated..."

pp. A-11 to A-15: These charts are most informative; however, some explanatory introductory text, particularly with respect to the geometry of the measurements and cross-referenced to the table on p. A-10, would make the material more accessible to the reader.